— 3 —

Solar Parameters for Modeling the Interplanetary Background

Maciej Bzowski* and Justyna M. Sokół
Space Research Center,
Polish Academy of Sciences, Warsaw, Poland

Munetoshi Tokumaru and Kenichi Fujiki
Solar-Terrestrial Environment Laboratory,
Nagoya University, Nagoya, Japan

Eric Quémerais and Rosine Lallement
LATMOS-IPSL,
Université Versailles-Saint Quentin, Guyancourt, France

Stéphane Ferron
ACRI-ST,
Guyancourt, France

Peter Bochsler
Space Science Center & Department of Physics,
University of New Hampshire, Durham, NH, USA
Physikalisches Institut, University of Bern, Bern, Switzerland

David J. McComas
Southwest Research Institute, San Antonio, TX, USA
University of Texas at San Antonio,
San Antonio, TX, USA

Abstract

The goal of the working group on cross-calibration of past and present ultraviolet (UV) datasets of the International Space Science Institute (ISSI) in Bern, Switzerland was to establish a photometric cross-calibration of various UV and

E. Quémerais et al. (eds.), *Cross-Calibration of Far UV Spectra of Solar System Objects and the Heliosphere*, ISSI Scientific Report Series 13,
DOI 10.1007/978-1-4614-6384-9_3,

extreme ultraviolet (EUV) heliospheric observations. Realization of this goal required a credible and up-to-date model of the spatial distribution of neutral interstellar hydrogen in the heliosphere, and to that end, a credible model of the radiation pressure and ionization processes was needed. This chapter describes the latter part of the project: the solar factors responsible for shaping the distribution of neutral interstellar H in the heliosphere. In this paper we present the solar Lyman-α flux and the topics of solar Lyman-α resonant radiation pressure force acting on neutral H atoms in the heliosphere. We will also discuss solar EUV radiation and resulting photoionization of heliospheric hydrogen along with their evolution in time and the still hypothetical variation with heliolatitude. Furthermore, solar wind and its evolution with solar activity is presented, mostly in the context of charge exchange ionization of heliospheric neutral hydrogen, and dynamic pressure variations. Also electron-impact ionization of neutral heliospheric hydrogen and its variation with time, heliolatitude, and solar distance is discussed. After a review of the state of the art in all of those topics, we proceed to present an interim model of the solar wind and the other solar factors based on up-to-date in situ and remote sensing observations. This model was used by Izmodenov et al. (2013, this volume) to calculate the distribution of heliospheric hydrogen, which in turn was the basis for intercalibrating the heliospheric UV and EUV measurements discussed in Quémerais et al. (2013, this volume). Results of this joint effort will also be used to improve the model of the solar wind evolution, which will be an invaluable asset in interpretation of all heliospheric measurements, including, among others, the observations of Energetic Neutral Atoms by the Interstellar Boundary Explorer (IBEX).

Brief Description of the Physics of the Neutral Interstellar Gas in the Inner Heliosphere

The distribution of neutral interstellar hydrogen and the ultraviolet radiation in the inner heliosphere are closely interrelated. Absolute calibration of observations of the heliospheric backscattered Lyman-α glow requires knowledge of the well-calibrated solar EUV output and of other solar forcing factors, mainly the solar wind. The role of those factors and their variabilities in shaping the distribution of neutral interstellar hydrogen can be derived from modeling papers cited in the remaining portion of this section.

Assuming inflow of a fully neutral gas with a finite velocity, $\boldsymbol{v}_\infty$, and temperature, T_∞, far away from the Sun, as well as a spherically symmetric and time-independent ionization rate, $\beta(\boldsymbol{r})$, plus an effective force, $\boldsymbol{F}(\boldsymbol{r})$, acting on the atoms. The distribution function of the gas at a distance r from the Sun will be axially symmetric around the inflow direction and can be given by the equation:

$$\boldsymbol{v} \cdot \nabla_{\boldsymbol{r}} f(\boldsymbol{v}, \boldsymbol{r}) + \frac{\boldsymbol{F}(\boldsymbol{r})}{m_H} \cdot \nabla_{\boldsymbol{v}} f(\boldsymbol{v}, \boldsymbol{r}) = -\beta f(\boldsymbol{v}, \boldsymbol{r}), \tag{3.1}$$

where ∇_x is the gradient operation in the x-direction, $\boldsymbol{r}$ and $\boldsymbol{v}$ are position and velocity vectors of the gas cell element, and m_H is the hydrogen atom mass.

Together with the assumption that the gas "at infinity" (in practice: a few hundreds of AU from the Sun or at solar distances relevant for heliospheric models) is homogeneous, collisionless, and Maxwellian (Izmodenov et al. 2000), this is the basis for the classical hot model of the distribution of neutral interstellar gas in the heliosphere (Thomas 1978; Fahr 1978, 1979; Wu and Judge 1979; Lallement et al. 1985b). Based on Liouville's theorem, the solution of this equation (Danby and Camm 1957) for the distribution function $f(\boldsymbol{v}, \boldsymbol{r}, t)$ for time t, location $\boldsymbol{r}$ and velocity $\boldsymbol{v}$ can be expressed as:

$$f(\boldsymbol{v}, \boldsymbol{r}, t) = f_\infty(\boldsymbol{v}_\infty(\boldsymbol{v}, r), \boldsymbol{r}_\infty(\boldsymbol{v}, \boldsymbol{r}))\, W(\boldsymbol{v}, \boldsymbol{r}, t), \tag{3.2}$$

where $W(\boldsymbol{v}, \boldsymbol{r}, t)$ is the survival probability of an atom that arrives at the time t at location $\boldsymbol{r}$ with velocity $\boldsymbol{v}$ from a distant location $\boldsymbol{r_\infty}$ where its velocity was $\boldsymbol{v_\infty}$. For now, t is only a formal parameter here. The probability of existence of such an atom in the distant region of the heliosphere is given by the distribution function $f_\infty(\boldsymbol{v}_\infty, \boldsymbol{r}_\infty)$, and the link between the local velocity and position vectors $\boldsymbol{v}(t)$, $\boldsymbol{r}(t)$ and the corresponding vectors in the so-called source region of the atoms can be obtained from the solution of the equation of motion of hydrogen atoms in the heliosphere:

$$\boldsymbol{F}(\boldsymbol{r}, t, v_r) = -\frac{G\, m_\mathrm{H}\, M\, (1 - \mu(v_r, t))}{r^2}\, \frac{\boldsymbol{r}}{r}. \tag{3.3}$$

In this expression, $\boldsymbol{F}$ is the total force acting on the atom with mass m_H, G is the gravitational constant, M the solar mass, v_r the radial velocity of the atom at time t, and μ is the ratio of solar resonant radiation pressure force to solar gravity. Radiation pressure will be more fully discussed in the section "Radiation Pressure and Its Variations".

As can be seen from this description, the distribution of neutral interstellar hydrogen in the inner heliosphere is determined on one hand by the dynamical influence of the Sun through the counteracting gravity and radiation pressure forces, and on the other hand by the ionization losses, collectively denoted β in Eq. 3.1. Both will be extensively discussed later in this paper. Here we only note that the ionization processes include charge exchange between the incoming neutral atoms and solar wind protons, ionization by impact of solar wind electrons, and ionization by the solar EUV radiation.

There are no important sources of neutral gas in the region of velocity phase space occupied by neutral interstellar gas, hence the lack of source terms in Eq. 3.1. Recombination could potentially be considered as such a source, but is not important for two reasons: (1) its rate is small in comparison with the ionization rate (Wachowicz 2006), and (2) the recombined solar wind particles maintain their pre-reaction velocities, which are equal to solar wind velocity. They do not contribute to the population of heliospheric atoms capable of scattering the solar FUV radiation which are responsible for the helioglow. Recombination is one of the secondary sources of the so-called Neutral Solar Wind (Błeszyński et al. 1992; Gruntman 1994; Bzowski and Ruciński 1996; Ruciński et al. 1998), which is beyond the scope of this chapter.

The classical hot model is almost analytical (in fact, numerical calculations are needed only when integrating the local distribution function to yield its moments, such as density and mean velocity) and thus convenient to use, but it is far from being perfect because many of its assumptions are not valid.

First, the interstellar gas in the Local Cloud is not fully neutral. The interaction of its ionized component with the plasma of the solar wind creates a boundary region of the heliosphere: the heliospheric interface. This interface begins at the termination shock of the solar wind, where the solar wind becomes subsonic and eventually turns back at the heliopause. The heliopause can be approximated as a thin layer separating the solar wind plasma from the interstellar plasma. Beyond the heliopause there is the outer heliosheath, where the pristine neutral interstellar gas is altered due to charge exchange interactions with protons from the piled-up and heated interstellar plasma. The history of the development of modeling of this region of the heliosphere can be found in Baranov (2006b) and modern views on this topic have been recently reviewed by Fahr (2004), Baranov (2006a), Izmodenov and Baranov (2006), and by Izmodenov et al. (2013, this volume). Second, the solar factors are not stationary or spherically symmetric, as will be demonstrated in the remaining portion of this chapter.

With these two observations in perspective it can be easily understood that quantitative interpretation of measuremeints of the helioglow require improvements in the classical hot model, which were realized quite early in the history of heliospheric research.

Lallement et al. (1985b) allowed for latitudinal modulation of the charge exchange rate, approximating it with a one-parameter formula: $1 - A \sin^2 \phi$. This enabled them to vary the equator-to-pole ratio of the ionization rates, but required keeping the width and range of the equatorial region of enhanced ionization fixed. A different extension of the hot model was proposed by Ruciński and Fahr (1989, 1991) who pointed out that the rate of electron-impact ionization does not scale as r^{-2}, even though its effects on the distribution of neutral interstellar hydrogen in the heliosphere are noticeable only within a few AU from the Sun, where its density is already strongly reduced. This aspect of the heliospheric physics has been neglected until Bzowski (2008) and Bzowski et al. (2008) reintroduced it in a refined, latitude-dependent manner.

The next generation of heliospheric models abandoned the assumption of invariability of solar radiation pressure and ionization rate. The first, though very simplified, model was proposed by Kyrölä et al. (1994), followed by Ruciński and Bzowski (1995); Bzowski and Ruciński (1995a,b); Bzowski et al. (1997). They studied variations in density, bulk velocity, and temperature of neutral interstellar hydrogen near the Sun, as well as variations in the helioglow intensity. Because of the lack of sufficient observational data at that time, they adopted an analytic model of the evolution of radiation pressure and ionization rate over the solar cycle.

Another modification to models of the heliosphere was introduced by Scherer et al. (1999), who addressed the prediction by Baranov et al. (1991); Osterbart and Fahr (1992); Baranov and Malama (1993) [see also (Malama et al. 2006)] that the charge exchange processes in the boundary layer of the heliosphere create a new, so-called secondary, collisionless population of neutral H atoms. They modified

the time-dependent hot model by approximating the distribution function, f_∞ in Eq. 3.2, by a sum of two Maxwellian functions with densities, bulk velocities and anisotropic temperatures being functions of the offset angle from the upwind direction. One of the Maxwellians represented the so-called primary population of neutral interstellar gas, which enters the supersonic solar wind after a "filtration" process in the outer heliosheath. The other, the so-called secondary population of neutral gas, is created via charge exchange with interstellar plasma in the outer heliosheath.

The values of temperature, density, and bulk velocity in these Maxwellian functions are parametrized by the angular separation of the point $\boldsymbol{r}_\infty$ in Eq. 3.2 from the upwind direction. The values of parameters of the distribution function f_∞ for a given set of interstellar parameters (interstellar neutral and plasma densities, flow speed and temperature) in this model must be obtained from an external model, such as the Moscow Monte Carlo model of the heliosphere [see, e.g., Izmodenov et al. (2009)]. Such an approach was later expanded and improved by Katushkina and Izmodenov (2010).

Along with the two-population non-Gaussian model, an approximation of radiation pressure and ionization rate by a spherically symmetric series of sines and cosines was added. The coefficients of those model functions were obtained from fits to measurements of the ionization rate and radiation pressure in the ecliptic plane. These approximations were described by Scherer et al. (1999) and Bzowski (2001a,b). Further extensions of the hot model to better account for latitudinal variations of solar wind speed and density are presented in the section "Historical Perspective: Insight from Heliospheric Backscatter Glow". The most recent development in modeling was an addition by Tarnopolski (2007), Tarnopolski and Bzowski (2008a) of radiation pressure force as a function of the radial velocity of an atom relative to the Sun. This effect will be discussed later in this chapter.

The list of modifications to the classical hot model presented above is also a list of effects that need to be taken into account at the solar side to facilitate inter-calibration of measurements of the helioglow with other UV observations in space. Apart from the heliospheric side, there is also the physics of the heliospheric interface and the conditions in the Local Interstellar Cloud [see, e.g., Frisch et al. 2009, 2011 for review] that must be taken into account, which, however, are beyond the scope of this chapter. From the above description it is clear that accurate modeling of neutral interstellar hydrogen in the inner heliosphere requires accurate knowledge of the factors contributing to the ionization and radiation pressure which are the main topic of this chapter.

In the following section, we sketch a global picture of the solar factors influencing neutral interstellar gas in the heliosphere. The new contributions to the picture, accomplished as a result of the ISSI working group's activities, are presented separately in two research papers: by Sokół et al. (2012), who elucidate the solar wind evolution in time and heliolatitude, and by Bochsler et al. (2012), who develops new ionization rates of heliospheric species. This chapter is intended as a review of the topic, even though the results of the working group are discussed in greater detail than insights from other sources.

Radiation Pressure and Its Variations

Temporal Evolution of the Total Solar Lyman-α Flux in the Ecliptic

The radiation pressure force that acts on neutral interstellar H atoms in the heliosphere is proportional to the total flux in the solar Lyman-α spectral line, which is defined as the spectral flux integrated over a 1 nm interval from 120 to 121 nm and is referred to as the composite solar Lyman-α flux. It has been measured since the middle of the 1970s [for the history of measurements, see Woods et al. 2000]. Despite all efforts, while precision of the measurements has been good, the problem of absolute calibration, prone to changes with time, has affected the accuracy from the very beginning. It is a measure of progress in this field that the discrepancies have been reduced from a factor of 4 in the 1970s to $\sim$ 15 % nowadays.

The composite Lyman-α time series, available from the Laboratory for Atmospheric and Space Physics (LASP) at the University of Colorado in Boulder, CO (http://lasp.colorado.edu/lisird/lya/) is scaled to the absolute calibration of UARS/SOLSTICE (Woods et al. 1996, 2000).

The time series of Lyman-α irradiance from the Sun shown in Fig. 3.1 is dominated by an 11 year period which matches the sunspot cycle. The irradiance at this wavelength at solar maximum is nearly double the value at solar minimum. In addition to the solar cycle signal, the time series also shows a strong 27-day period due to the rotation of the Sun. Active regions are much brighter in Lyman-α than the surrounding quiet Sun, so the irradiance rises as these features rotate into view on the solar disk.

The cadence of deduced flux values is presently 1 day and the inevitable gaps are usually filled using a hierarchy of proxies, as illustrated in Fig. 3.1. The most widely used is the proxy based on the solar radio flux at the 10.7 cm wavelength, the so-called $F_{10.7}$ flux (Covington 1947; Tapping 1987). Another frequently used proxy is the Mg II core-to-wing ($\mathrm{MgII_{c/w}}$) ratio (Heath and Schlesinger 1986; Viereck and Puga 1999).

The use of proxies raises the question of credibility of the results (Floyd et al. 2002, 2005). The solar FUV radiation varies on many time scales, from hours to more than solar cycle length. Proxies generally follow the variability of the quantity being modeled, but not precisely and not on all time scales. In particular, even though the correlation coefficients, calculated from a long time series of daily values may exceed 0.9, the agreement between the corresponding elements of the two time series can sometimes be in disagreement on short time scales. One cause of this disagreement is due the differing center-to-limb behavior of the proxy. Depending on the solar latitude of the active region producing the emission, the timing of the peak emission for the FUV and for the proxy may be significant (Floyd et al. 2005).

An illustration can be found in Fig. 3.2. The upper panel presents the daily change rate of the composite flux (see figure caption for definition of this quantity) and the lower panel the change rate of the monthly-averaged composite flux. The amplitude of the change rate depends on primarily on which proxy is used rather than on the strength of the solar cycle. While the monthly rate does not seem

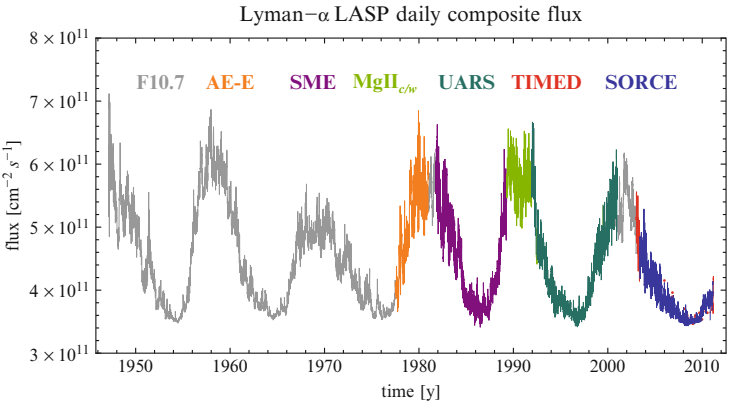

Figure 3.1: Wavelength- and disk-integrated solar Lyman-α flux from the Laboratory for Atmospheric and Space Physics (LASP), referred to as the total Lyman-α flux $I_{\rm tot}$. The daily time series is a composite of actual measurements from various experiments re-scaled to the common calibration of UARS/SOLSTICE, with the gaps filled by proxies. Color codes: *gray*: $F_{10.7}$ proxy, *orange*: AE-E, *purple*: SME, *green*: $MgII_{c/w}$ proxy, aquamarine: UARS/SOLSTICE version 18, *red*: TIMED/SEE, *blue*: SORCE/SOLSTICE (based on Woods et al. 2000)

to depend on the source proxy, the difference between the change rates derived from the $F_{10.7}$ proxy and the proxies based on FUV measurements of the Sun is especially pronounced.

As a consequence, the quality of the approximation at these short scales is reduced even though it may be quite satisfactory at longer time scales, e.g., for solar rotation period averages, as can be judged from the behavior of the monthly change rates shown in the lower panel of Fig. 3.2 and as suggested by Dudok de Wit et al. (2009). For modeling the distribution of neutral interstellar gas in the heliosphere, the Carrington period of solar rotation is the finest time scale presently in use,[1] so the short time scale proxy imperfections are not a big problem for this purpose.

Variation of the Lyman-α Flux with Heliolatitude

The disk-averaged solar Lyman-α flux is made of at least three components (Amblard et al. 2008): a quiet Sun contribution and two components that vary with solar activity, i.e., from the coolest regions of the chromosphere and from the hot lower corona. The inhomogeneous heliolatitude distribution of active regions was pointed out by Cook et al. (1980), who constructed a two-component latitude-dependent model of disk-averaged solar UV irradiance.

Cook et al. (1981) considered the solar Lyman-α emission and suggested that the ratio of the disk-integrated solar flux at the pole to the flux at the equator

[1] A H atom traveling at $30\,{\rm km\,s^{-1}}$ covers ~ 0.5 AU during one Carrington period.

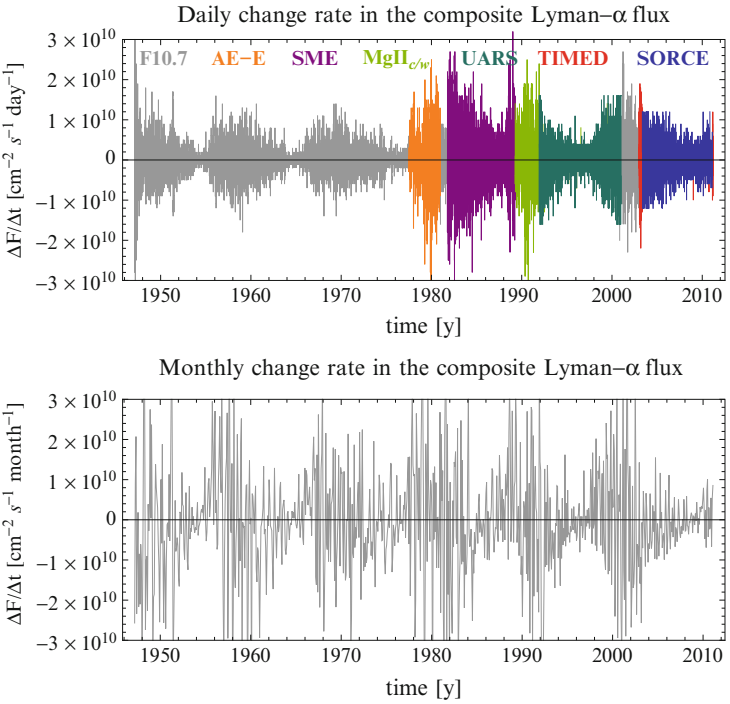

Figure 3.2: Rates of change of the total Lyman-α flux $I_{\rm tot}$. Shown are the rates of change per unit time $\frac{\Delta I_{\rm tot}}{\Delta t} = \frac{I_{\rm tot}(t_{i+1}) - I_{\rm tot}(t_i)}{t_{i+1} - t_i}$ of the daily (*upper panel*) and monthly (*lower panel*) composite Lyman-α flux presented in Fig. 3.1, with identical color coding

should be about $a_{\rm Lya} = 0.8$ during solar minimum, when the active regions are distributed in latitudinal bands. These suggestions were supported by direct solar minimum observations of the solar corona by Auchère (2005). Such a ratio was suggested to be also valid for solar maximum by Pryor et al. (1992), based on indirect evidence from observations of the Lyman-α helioglow. Thus it seems that the latitudinal anisotropy of the Lyman-α flux does not change substantially during the solar cycle, although this conclusion certainly needs further verification.

Bzowski (2008) suggested that the latitude dependence of the disk-integrated solar Lyman-α flux may be approximated by the formula:

$$I_{\rm tot}(\phi) = I_{\rm tot}(0) \sqrt{a_{\rm Lya} \sin^2(\phi) + \cos^2(\phi)}, \tag{3.4}$$

where ϕ is heliolatitude, $a_{\rm Lya}$ the "flattening" factor and $I_{\rm tot}(0)$ is the equatorial Lyman-α flux.

Heliolatitude variation of the disk-integrated Lyman-α line profile is, to our knowledge, unexplored. On one hand, some form of variation should be expected because, as shown by Tian et al. (2009a,b,c), the line profile depends on the features on the solar disk that are being observed and the latitude distribution of these

features is inhomogeneous and varies during solar cycle. On the other hand, the apparent lack of strong variability of the disk-integrated flux might suggest that the spectral variation with heliolatitude is mild. Should the disk-integrated spectral flux indeed vary with heliolatitude, this would potentially have consequences both for the photoionization rate and the radiation pressure force. However, recent investigation of the variation of the solar spectrum with heliolatitude by Kiselman et al. (2011) seems to have brought a negative result (i.e., no variation).

Mechanism of Radiation Pressure

The mechanism of resonant interaction of an H atom with solar radiation, which leads to a repelling force of resonant radiation pressure acting on neutral H atoms in the heliosphere, was extensively discussed by Brasken and Kyrölä (1998). In brief, the probability $f_{\mathrm{abs}}(\lambda)$ that a hydrogen atom in the ground state, whose base wavelength is λ_0, absorbs an incoming photon at wavelength λ is equal to:

$$f_{\mathrm{abs}}(\lambda) = \frac{\Gamma_R}{2\pi c\left(\frac{1}{\lambda} - \frac{1}{\lambda_0}\right)^2 + \frac{\Gamma_R^2}{4}}, \tag{3.5}$$

where Γ_R is the energetic width of the second orbital of the atom, corresponding to a Doppler width of about $\pm 25\,\mathrm{m\,s^{-1}}$ around the rest wavelength of the Lyman-α transition, and c is speed of light. An atom whose radial velocity relative to the Sun is $v_r = 0$ will absorb photons from the very center of the solar line at λ_0, but if its radial velocity v_r is non-zero, then due to the Doppler effect it will be tuned to a different portion of the solar line profile, namely to the wavelength $\lambda = \lambda_0(1 - v_r/c)$. Within about 10^{-7} s after it absorbs a Lyman-α photon, the atom will re-emit the photon at an angle ω relative to the impact direction with the scatter-angle probability $p(\omega)$ described by:

$$p(\omega) = \frac{\cos(\omega)}{4} + \frac{11}{12}. \tag{3.6}$$

Hence, a resonant interaction of the atom with a suitable photon results in a change of atomic momentum at the moment of absorption by $\Delta p = h\nu = c\,h/\lambda$ in the antisolar direction, followed after a time of 10^{-7} s by another momentum change in the direction described by Eq. 3.6. However, the typical frequency of interactions between solar photons and H atoms at 1 AU, which is proportional to the solar spectral flux, is on the order of 1/500 Hz (Quémerais 2006). Statistically, on time scales shorter than the time scales of a change in atomic velocity relative to the Sun, the only dynamical net effect of the interaction of the atom with solar radiation is the antisolar momentum change.[2]

Since the interplanetary medium is optically thin within a few AU from the Sun (Quémerais 2006), the solar spectral flux scales as the inverse square of solar distance. Consequently, the solar radiation pressure also scales with solar distance

[2]One can expect another statistical effect: an increase in the local velocity spread in the population of neutral H gas in the heliosphere, but, to our knowledge, this effect has not been studied in the available literature.

as $1/r^2$, thus leading to a partial compensation of solar gravity. Hence the effective solar force acting on an atom is conveniently expressed by the fraction $\mu\left(I_{\rm tot}\left(t\right), v_r\right)$ of the solar gravity force. It is proportional to the spectral flux F_λ corresponding to the Doppler-shifted wavelength $\lambda = \lambda_0\left(1 + v_r/c\right)$, which results from the instantaneous radial speed v_r of the atom relative to the Sun. Since the spectral flux varies with time, effectively the μ factor is a function of radial velocity and time, as expressed in Eq. 3.3.

Solar Lyman-α Line and Resulting Radiation Pressure

Measurements of the solar Lyman-α line profile, although scarce, date back to the 1970s (Vidal-Madjar 1975; Artzner et al. 1978; Bonnet et al. 1978; Lemaire et al. 1978; Woods et al. 1995). However, they were performed from within the Earth's exosphere and hence suffered from the absorption by geocoronal Hydrogen in the spectral region most relevant for the helioglow. Only after the launch of SOHO, which orbits at the L1 Lagrange point, was it possible to obtain an unobstructed view of the full spectral range of the disk-integrated solar line (Warren et al. 1998c; Lemaire et al. 1998, 2002, 2005).

The solar Lyman-α line features a self-reversed shape that previously was approximated by two Gaussian functions (Fahr 1979; Chabrillat and Kockarts 1997; Scherer et al. 2000). Recently, Tarnopolski (2007) and Tarnopolski and Bzowski (2008b) showed that the measurements by Lemaire et al. (2002) can all be fit by a three-Gaussian model parameterized by the disk-integrated flux:

$$\begin{aligned}&\mu\left(v_r, I_{\rm tot}\left(t\right)\right) = \\ &\quad A\left[1+BI_{\rm tot}\left(t\right)\right]\exp\left(-Cv_r^2\right)\left[1+D\exp\left(Fv_r-Gv_r^2\right)+H\exp\left(-Pv_r-Qv_r^2\right)\right]\end{aligned} \tag{3.7}$$

with the following parameters:

$$\begin{array}{lll} A = 2.4543\times10^{-9} & B = 4.5694\times10^{-4} & C = 3.8312\times10^{-5} \\ D = 0.73879 & F = 4.0396\times10^{-2} & G = 3.5135\times10^{-4} \\ H = 0.47817 & P = 4.6841\times10^{-2} & Q = 3.3373\times10^{-4} \end{array}$$

and v_r expressed in $\mathrm{km\,s^{-1}}$. The accuracy of the fit is similar to the accuracy of the measurements, estimated to be $\sim 10\,\%$.

With this formula, one can calculate the μ factor for an arbitrary radial velocity, v_r, providing that the total solar Lyman-α flux, $I_{\rm tot}$, is known. The dependence of the μ factor on radial velocity for the total flux values representative for solar minimum and maximum conditions is shown in Fig. 3.3, adapted from Tarnopolski and Bzowski (2008b).

The spectral region of the solar Lyman-α line most relevant for modeling the heliospheric Lyman-α glow is the wavelength band straddling the central wavelength by approximately $\pm 30\,\mathrm{km\,s^{-1}}$. The spectral flux at line center is closely correlated with the line-integrated flux $I_{\rm tot}$ (Vidal-Madjar and Phissamay 1980). This is beneficial to the modeling of the helioglow because it permits us to easily calculate the μ factor based on measurements of the solar line-integrated Lyman-α flux.

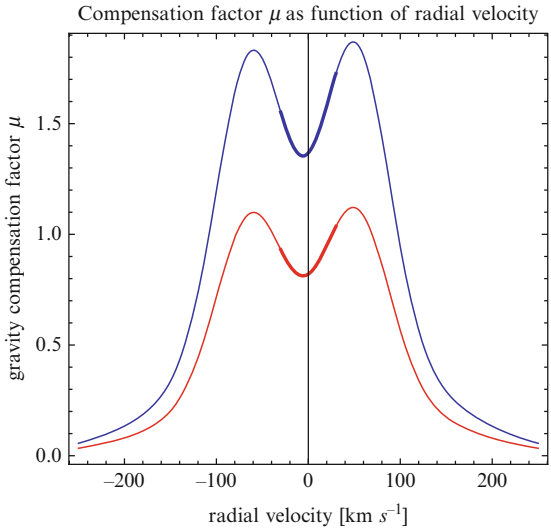

Figure 3.3: Ratio μ of solar radiation pressure force to solar gravity based on the model specified in Eq. 3.7, shown as a function of radial velocity of a H atom relative to the Sun for the total solar flux values corresponding to the minimum (*red*) and maximum (*blue*) of solar activity. *Thick lines* indicate the spectral region $\pm 30\,\mathrm{km\,s^{-1}}$ around 0 Doppler shift, relevant for the neutral interstellar hydrogen gas in the heliosphere

Approximate Values of the μ Factor

Since calculating the properties of neutral interstellar hydrogen inside the heliosphere using a model that takes the full solar line profile is computationally demanding, an approach where the μ factor does not depend on radial velocity is widely used. To obtain an appropriate μ value, a formula to translate the line-integrated flux into the μ factor is needed. In the past, this issue was addressed by taking

$$\mu\,(I_{\mathrm{tot}}) = 3.0303 \times 10^{10}\,\mathrm{cm^2\,s}\,a\,I_{\mathrm{tot}}, \tag{3.8}$$

where I_{tot} is the disk- and line-integrated solar Lyman-α flux and a is a constant usually assumed to be between 0.85 and 1. With increasing accuracy of the measurements, more sophisticated formulae have become available. Emerich et al. (2005) fit the following relation between the spectral flux at line center F_λ and the total flux:

$$\frac{F_\lambda}{10^{12}\mathrm{cm^{-2}s^{-1}nm^{-1}}} = 0.64\left(\frac{I_{\mathrm{tot}}}{10^{11}\mathrm{s^{-1}cm^{-2}}}\right)^{1.21} \pm 0.08. \tag{3.9}$$

Bzowski et al. (2008) found a linear relation between the spectral flux averaged over the range $\pm 30\,\mathrm{km\,s^{-1}}$ about the line center and the line- and disk-integrated flux:

$$\mu\,(I_{\mathrm{tot}}) = 3.473\,10^{-12}\,I_{\mathrm{tot}} - 0.287. \tag{3.10}$$

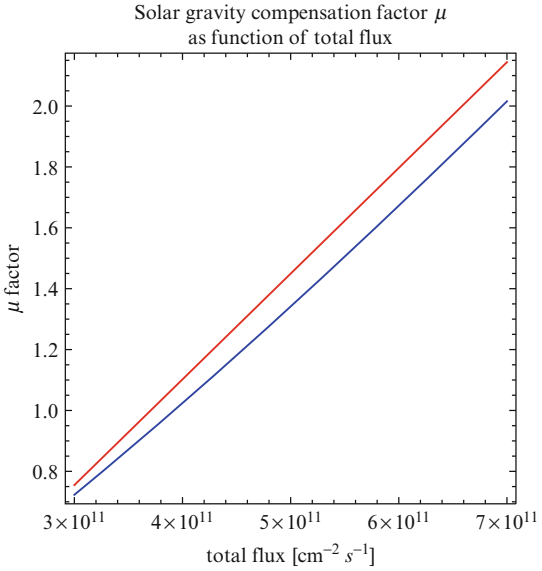

Figure 3.4: Solar radiation pressure factor μ as a function of the total flux in the Lyman-α line I_{tot}. The *blue line* represents the relation from Eq. 3.9 by Emerich et al. (2005), which connects the total flux I_{tot} with the spectral flux precisely at line center F_{λ_0}. The conversion to the μ factor is then performed using Eq. 3.8, with $a = 0.9$. The *red line* shows the relation defined in Eq. 3.10 by Bzowski et al. (2008). Here, the relation between the total solar flux and spectral flux is adopted from averaged spectral flux over $\pm 30\,\mathrm{km\,s^{-1}}$ around the line center

Figure 3.4 shows a comparison of the predicted μ values as a function of the solar total Lyman-α flux obtained from Eqs. 3.8–3.10. It suggests that if one decides not to use a model radiation pressure force which is dependent on the radial velocity of the atom, then the calculation of a good effective μ factor is not a straightforward task. In fact, it may be appropriate to use different formulae for the upwind and downwind regions in the heliosphere, as can be inferred from the asymmetry of the solar Lyman-α line profile seen in Fig. 3.3. Such an approach, to our knowledge, has never been implemented. Calculating μ as a function of v_r is required in order to model interstellar deuterium in the inner heliosphere (Tarnopolski and Bzowski 2008b).

The μ values obtained from the relations defined in Eqs. 3.9 (Emerich et al. 2005) and 3.10 (Tarnopolski and Bzowski 2008b), calculated from the monthly values[3] of the LASP composite Lyman-α flux (Fig. 3.1) are presented in Fig. 3.5. Differences between the values obtained from these equations are on the order of 10 %, i.e. on the order of the uncertainty of the total flux.

[3]Throughout the text, "monthly" is used as synonymous with "averaged over one Carrington rotation period".

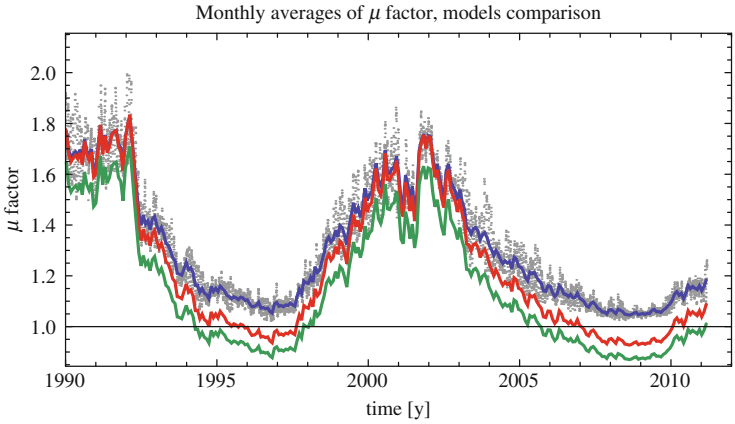

Figure 3.5: Comparison of the solar radiation pressure factors μ that approximate the compensation of solar gravity by the resonant radiation pressure force acting on neutral H atoms. The *green line* represents monthly values obtained from Eq. 3.9 (Emerich et al. 2005) and the *red line* shows the monthly values obtained from Eq. 3.10 (Bzowski et al. 2008). The *blue line* represents the μ values calculated from Eq. 3.8 with $a = 0.9$. The *gray dots* represent daily values of the μ factor, calculated from daily values of the composite Lyman-α flux using Fig. 3.8

Ionization Processes

The three main ionization processes of neutral interstellar hydrogen atoms in the heliosphere are the following:
charge exchange with solar wind charged particles (mostly protons) resulting in a pickup proton (p_{PUI}) and an energetic neutral atom (ENA):

$$H + p \rightarrow p_{PUI} + H_{ENA},$$

photoionization by photons ν of solar EUV radiation:

$$H + \nu \rightarrow p_{PUI} + e,$$

and ionization by impact of solar wind electrons:

$$H + e \rightarrow p_{PUI} + 2e.$$

As a result of the charge exchange reaction, a solar wind proton captures an electron from a neutral interstellar H atom and becomes an energetic neutral atom (ENA) However, it maintains its momentum and thus does not enter the interstellar population. In this respect, even though one neutral H atom is replaced by another, such a reaction is still a loss process for the neutral interstellar gas despite the fact that the total number of H atoms in the system does not change.

The newly-created protons are picked up by the solar wind flow (Fahr 1973; Vasyliunas and Siscoe 1976) regardless of the reaction they originate from, creating

a distinct population that can be measured (Möbius et al. 1985; Gloeckler et al. 1993) and analyzed (e.g. Gloeckler and Geiss 2001; Gloeckler et al. 2004; Bzowski et al. 2008), but this topic is outside the scope of this text.

The charge exchange reaction does not deplete solar wind protons. A proton from the core of the solar wind distribution function is replaced with a pickup proton. The concentration of protons per unit volume is not changed, although the distribution function of solar wind protons is modified.

The two remaining ionization reactions do cause genuine losses for the entire H population: a H atom enters the reaction and is not simply replaced with another one at a different velocity. Eventually, a proton–electron pair is created and the proton is picked up by solar wind.

Charge Exchange

General Formula

The process of resonant charge exchange between H atoms and protons is of crucial importance for the physics of the heliosphere. It contributes to the pressure balance between the solar wind and the interstellar gas and enables the energy and momentum transport across the heliopause. Charge exchange losses of neutral interstellar gas in the supersonic solar wind, which is discussed in this section, are only a small piece of a larger picture of the role of charge exchange in the heliosphere.

The rate of charge exchange between neutral H atoms and solar wind protons can be regarded as the probability of a charge exchange act within unit time in a given location in space. For an H atom traveling with velocity $\boldsymbol{v}_{\mathrm{H}}$ and a local proton distribution function $f_p(\boldsymbol{v}_p)$, where $\boldsymbol{v}_p$ is the velocity vector of an individual proton, the rate of charge exchange can be calculated from the formula:[4]

$$\beta_{\mathrm{CX}} = \int \sigma_{\mathrm{CX}} \left(|\boldsymbol{v}_{\mathrm{H}} - \boldsymbol{v}_p|\right) |\boldsymbol{v}_{\mathrm{H}} - \boldsymbol{v}_p| \, f_p \left(\boldsymbol{v}_p\right) \mathrm{d}\boldsymbol{v}_p, \tag{3.11}$$

where $\boldsymbol{v}_{\mathrm{H}} - \boldsymbol{v}_p \equiv \boldsymbol{v}_{\mathrm{rel}}$ is the relative velocity between the H atom and an individual proton and $\sigma_{\mathrm{CX}} \left(|\boldsymbol{v}_H - \boldsymbol{v}_p|\right)$ is the reaction cross section. The integration covers the entire proton velocity space. This formula can be put into an equivalent form:

$$\beta_{\mathrm{CX}} = \int \sigma_{\mathrm{CX}} \left(|\boldsymbol{v}_{\mathrm{rel}}|\right) |\boldsymbol{v}_{\mathrm{rel}}| \, f_p \left(\boldsymbol{v}_{\mathrm{H}} - \boldsymbol{v}_{\mathrm{rel}}\right) \mathrm{d}\boldsymbol{v}_{\mathrm{rel}}. \tag{3.12}$$

Depending on the underlying plasma regime and on the velocity of the H atom, various simplifications can be made. When the kinetic spread of the plasma $u_{\mathrm{T},p}$ is small compared with the plasma flow velocity $\boldsymbol{v}_{\mathrm{SW}}$:

$$\begin{aligned} u_{\mathrm{T},p} &\ll |\boldsymbol{v}_{\mathrm{SW}}| \\ \sqrt{2kT_p/m_p} &\ll \left| \int \boldsymbol{v}_p \, f \left(\boldsymbol{v}_p\right) \mathrm{d}\boldsymbol{v}_p / n_p \right|, \end{aligned}$$

[4]We adopt a convention where bold-italic characters mean vector quantities, while italics symbolize scalars.

we can approximate the proton distribution function by a delta-function centered at the solar wind speed. The formula for charge exchange rate then simplifies to:

$$\beta_{\mathrm{CX}} = \sigma_{\mathrm{CX}}\left(v_{\mathrm{rel}}\right) n_p v_{\mathrm{rel}}, \tag{3.13}$$

where n_p is the local proton density and v_{rel} becomes $v_{\mathrm{rel}} \equiv |\boldsymbol{v}_{\mathrm{H}} - \boldsymbol{v}_{\mathrm{SW}}|$. This is the case for ENAs that travel in the supersonic solar wind at $v_{\mathrm{H}} \sim 50\,\mathrm{km\,s^{-1}}$ or faster.

For $v_H \ll v_{SW}$, i.e., for atoms from the thermal interstellar H populations in the supersonic solar wind, $v_{\mathrm{rel}} \simeq v_p$. Then the rate of charge exchange between H atoms and solar wind protons is given by:

$$\beta_{\mathrm{CX}} = \sigma_{\mathrm{CX}}\left(v_{\mathrm{SW}}\right) n_p v_{\mathrm{SW}}. \tag{3.14}$$

This is the baseline formula for charge exchange rate between protons from the supersonic solar wind and neutral interstellar H atoms. It has been widely used in the heliospheric physics and will be used in the later part of this chapter. The accuracy of this approximation is subject of one of the following subsections.

Charge Exchange Cross Section

The collision speed range most relevant for heliospheric physics is from $\sim 1\,\mathrm{km\,s^{-1}}$ to $\sim 1,000\,\mathrm{km\,s^{-1}}$, which is equivalent to the energies of 0.005 eV and 5.2 keV, respectively. Relative velocities between interstellar neutral H atoms and protons in the supersonic solar wind range from $\sim 300\,\mathrm{km\,s^{-1}}$ to $\sim 1,000\,\mathrm{km\,s^{-1}}$.

A detailed discussion of the charge exchange process and of the cross section for this reaction can be found in Fahr et al. (2007) and will not be repeated here. For the purpose of this work it is important to point out that there were four cross section formulae used in heliospheric physics in the past: from Fite et al. (1962), Maher and Tinsley (1977), Barnett et al. (1990), and Lindsay and Stebbings (2005).

Fite et al. (1962) and Maher and Tinsley (1977) both proposed to approximate the charge exchange cross section as a function of relative velocity v_{rel} between the colliding partners by the formula:

$$\sigma_{\mathrm{CX}}\left(v_{\mathrm{rel}}\right) = \left(a + b \ln v_{\mathrm{rel}}\right)^2. \tag{3.15}$$

The valid range for the Fite et al. (1962) relationship was claimed to be between 20 and 2,000 eV. The domain of the Maher and Tinsley (1977) expression was taken to be from 0.005 to 1 keV.

Barnett et al. (1990) fit a form of Chebyshev polynomials which were valid in a broad energy range. Bzowski (2001b) approximated the data used by Barnett et al. (1990) but restricted to $v_{\mathrm{rel}} < 800\,\mathrm{km\,s^{-1}}$ by the following expression:

$$\sigma_{\mathrm{CX}}\left(v_{\mathrm{rel}}\right) = a_0 + \sum_{i=1}^{3} a_i \left(\ln v_{\mathrm{rel}}\right)^i. \tag{3.16}$$

The most recent and authoritative compilation of measurements and calculations was presented by Lindsay and Stebbings (2005), who suggested the following formula

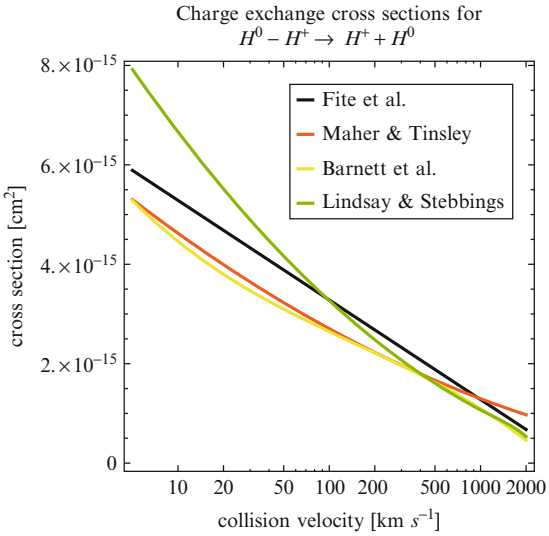

Figure 3.6: Cross sections for charge exchange reaction between protons and H atoms in the energy range most important in the heliospheric physics. The recommended relation from Lindsay and Stebbings (2005) is compared with the formulae used in the past by Fite et al. (1962), Maher and Tinsley (1977) and Barnett et al. (1990)

for the cross section expressed in cm^2, valid for collision energies E between 0.005 and 600 keV:

$$\sigma_{CX}(E) = 10^{-16}\left(1 - \exp\left[-67.3/E\right]\right)^{4.5}\left(4.15 - 0.531\ln E\right)^2 . \tag{3.17}$$

A comparison of the cross sections from the four formulae is presented in Fig. 3.6.

It is important to note that while all four formulae return similar results for the collision speeds relevant to the supersonic solar wind, the one from Lindsay and Stebbings (2005) returns a significantly larger cross section for lower energies, which are relevant for the outer heliosheath. Thus, adoption of the older formulae may result in a significant underestimation of the coupling strength between the neutral interstellar gas and the plasma in the outer heliosheath where the secondary population of interstellar H atoms is formed. This would have marked consequences for the results of heliospheric modeling, as described by Izmodenov et al. (2012, this volume).

Averaging, Approximating and Estimating Errors in the Calculation of Charge Exchange Rate

Models of neutral heliospheric gas usually need charge exchange rates averaged over specific time intervals, typically the Carrington rotation period or a year. Carrington period averages of this quantity will be extensively discussed in later sections of this paper. But what is the correct way of calculating these averages?

Since the solar wind speed and density vary with time on time scales from minutes to centuries, the instantaneous values of charge exchange rate vary on the same time scales. Theory immediately suggests that to calculate the losses of the neutral atom population due to charge exchange over a time interval ΔT, one has to integrate the instantaneous rate given by Eq. 3.14 over this interval. The mean charge exchange rate $\langle \beta \rangle_{\Delta T}$ over interval ΔT is calculated from:

$$\langle \beta \rangle_{\Delta T} = \frac{1}{\Delta T} \int_{\Delta T} \sigma_{\mathrm{CX}} \left(v_{\mathrm{SW}} \left(t \right) \right) n_p \left(t \right) v_{\mathrm{SW}} \left(t \right) \, dt. \tag{3.18}$$

In practice, however, this strict approach is usually not possible to follow because high-resolution data on solar wind density and speed throughout the heliosphere are not available. Hence, a simplified version of the Carrington averaging is adopted:

$$\langle \beta_{\mathrm{CX}} \rangle_{\mathrm{Carr}} = \langle n_p \rangle_{\mathrm{Carr}} \, \langle v_{\mathrm{SW}} \rangle_{\mathrm{Carr}} \, \sigma_{\mathrm{CX}} \left(\langle v_{\mathrm{SW}} \rangle_{\mathrm{Carr}} \right), \tag{3.19}$$

where $\langle . \rangle_{\mathrm{Carr}}$ marks averaging over the Carrington rotation period.

We have verified that calculations performed on the hourly data from the OMNI-2 web page[5] into Carrington rotation periods using Eq. 3.19 instead of Eq. 3.18 introduces a bias of $\sim 3.5\,\%$ in the computed monthly charge exchange rate. The bias fluctuates in time from $0\,\%$ to $\sim 8\,\%$. The magnitude of this bias is on the order of half the typical electron impact ionization rate, as can seen in Fig. 3.7.

One source of error in the charge exchange rate is incomplete data coverage. Inevitably, some fragments of time series measured in space happen to be unavailable. For some time intervals, one quantity (density or speed) may be present while the other one is missing. For some instruments, the data gaps are correlated with the values of solar wind speed. The gaps typically occur in series and are not randomly distributed over a Carrington rotation. This may bias the Carrington averages and induce errors in the calculated averaged charge exchange rates. To estimate the magnitude of the resulting errors, we calculated Carrington period averages of solar wind density and speed from all available OMNI-2 data and then computed the monthly charge exchange rates using Eq. 3.19. Subsequently, we changed the data selection criterion: we demanded both density and speed to be available in the qualifying hourly records and repeated the calculation of the charge exchange monthly averages. Comparison of the resulting two time series suggests that an error in the charge exchange rate due to data availability is about $2\,\%$, but no bias is introduced. The errors are likely to be largest during the Carrington rotations with lowest data coverage. A presentation of the data coverage in the OMNI-2 collection can be found in Veselovsky et al. (2010).

Another source of error is the approximation of stationary H atoms. In this approximation, used in Eqs. 3.14–3.19, it is assumed that the atoms subjected to charge exchange losses do not move relative to the Sun, i.e., that $v_{\mathrm{rel}} = v_{\mathrm{SW}}$ in Eq. 3.13. This is not the case in the heliosphere, even for the atoms of neutral interstellar gas. In the inner heliosphere, they typically travel at $\sim 30\,\mathrm{km\,s^{-1}}$

[5]The OMNI-2 dataset is described in the section "Evolution of Solar Wind in the Ecliptic Plane".

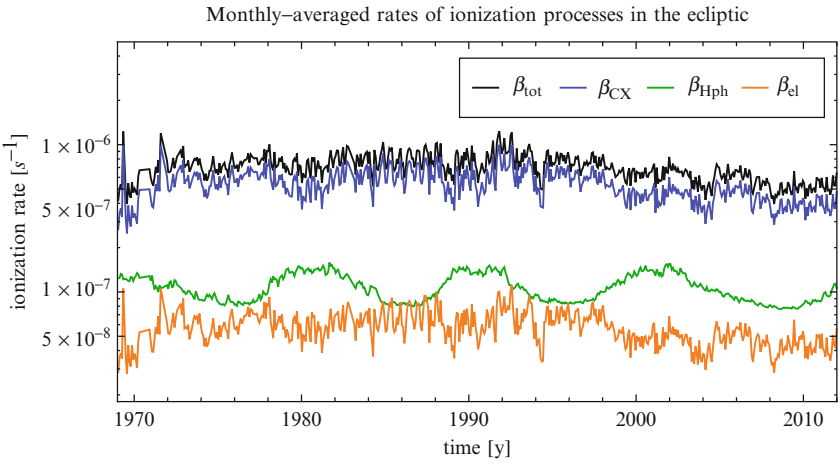

Figure 3.7: Monthly ionization rates in the ecliptic plane from all relevant processes. *Blue marks* the charge exchange rate, calculated from Eq. 3.14 using the cross section from Eq. 3.17 (Lindsay and Stebbings 2005) and monthly averages of solar wind speed and density shown in Fig. 3.8. *Green* represents the photoionization rate (Bochsler et al. 2012), and *orange* the electron-impact ionization rate (Bzowski 2008). The total ionization rate, being a sum of the three aforementioned rates, is shown in *black*. Note that the vertical axis is logarithmic. To better highlight the secular change in the charge exchange rate after the turn of the past century, an exploded view of the charge exchange rate for the time interval from 1985 through 2011 is shown in Fig. 3.15

(Bzowski et al. 1997). The modification of the charge exchange rate due to the proper motion of H atoms can be assessed as follows. The atoms approaching the Sun, i.e., mostly in the upwind hemisphere, run against solar wind and thus the relative speed is the sum of the proper velocity of the atoms and of the solar wind speed. For a typical solar wind speed in the ecliptic plane of $\sim 440\,\mathrm{km\,s^{-1}}$, the change in the charge exchange rate is by $(440 + 30)\ \sigma_{CX}\,(440 + 30)\ /\ (440\,\sigma_{CX}\,(440)) \simeq 1.035$. Similarly, for the atoms in the downwind hemisphere which recede from the Sun, the change in charge exchange rate is 0.965 (for σ_{CX} defined in Eq. 3.17). Thus, the error induced by the approximation of stationary atom is about $\pm 3.5\,\%$. It systematically varies with the offset angle from the upwind direction, transitioning from an underestimation in the upwind hemisphere to an overestimation in the downwind hemisphere.

All in all, the errors in monthly charge exchange rates due to the approximations presented are of similar magnitude. Since they are independent sources of error, they can be added in quadrature and total about $\sim 5.5\,\%$. This should be contrasted with the uncertainty of $\sim 10\,\%$ related to the uncertainty of the cross section alone.

Another approximation frequently made in the heliospheric modeling is that the charge exchange rate decreases with the square of solar distance. This assumption

originates from the inverse-quadratical reduction of solar wind density with distance, with approximately constant velocity. We will assess now how good this approximation is.

The solar wind expands almost radially (i.e., its non-radial velocity components are very small in comparison with the radial component). It expands with basically constant speed between the outer boundary of the acceleration region near the Sun (located inside a few solar radii) and approximately 10 AU, where the slowdown effects of mass loading due to the ionization of neutral interstellar gas become measurable (Fahr and Ruciński 1999, 2001, 2002; Lee et al. 2009; Richardson et al. 1995, 2008b). The overall slowdown continues up to a few AU upstream from the termination shock. At that point, the flow speed has already been reduced by about $67\,\mathrm{km\,s^{-1}}$ relative to the speed at 1 AU (Richardson et al. 2008b). It is additionally slowed down by the component of protons reflected at the termination shock (Liewer et al. 1993; Richardson et al. 2008a). The effect of pickup ions on distant solar wind varies with the angle from the inflow direction (Fahr and Ruciński 1999), but the strongest effect is expected in the upwind hemisphere, where Voyager measurements were made.

Outside the acceleration region, the solar wind flux initially falls off with solar distance as $1/r^2$. This relation, stemming directly from the continuity equation, is not significantly altered by the interaction of the solar wind plasma with neutral interstellar gas. The main reaction is charge exchange—a reaction that does not result in a change in the local proton density, only in a shift of the reaction product into the pickup ion region of the total distribution function. Only the two secondary reactions, photoionization and ionization by electron impact, actually inject new protons into the pickup ion region in phase space.

As a result, the adjusted[6] solar wind density, treated as a sum of the core solar wind protons and pickup protons, increases very slowly with solar distance. This was approximately assessed by Lee et al. (2009), who give the following formula for the absolute density at a distance r of pickup ions $n_{\mathrm{PUI,ph}}\,(r)$ created by photoionization

$$n_{\mathrm{PUI,ph}}\,(r) = \frac{r_E^2\, n_{\mathrm{H,TS}}\, \beta_{\mathrm{ph},E}}{r\, v_{\mathrm{SW},E}}, \tag{3.20}$$

where $\beta_{\mathrm{ph},E}$ is the photoionization rate at $r_E = 1$ AU, $v_{\mathrm{SW},E}$ the solar wind speed at r_E, and $n_{\mathrm{H,TS}}$ the neutral interstellar H density at the termination shock.

For the H density at the termination shock located at 90 AU equal to $0.087\,\mathrm{cm^{-3}}$ (Bzowski et al. 2008), the photoionization rate is $10^{-7}\,\mathrm{s^{-1}}$ (see below), and the typical solar wind speed is $440\,\mathrm{km\,s^{-1}}$. The density of pickup ions at 90 AU from the Sun is then equal to $3.3\,10^{-5}\,\mathrm{cm^{-3}}$, which scales to $0.27\,\mathrm{cm^{-3}}$ when quadratically adjusted to 1 AU. For a typical solar wind density at 1 AU equal to $5\,\mathrm{cm^{-3}}$, this yields a $\sim 5\,\%$ excess of the total solar wind density with respect to the pure $1/r^2$ drop.

Inserting this modified adjusted density into Eq. 3.14, along with the reduced solar wind speed of $440 - 67 = 373\,\mathrm{km\,s^{-1}}$, one obtains an adjusted charge exchange rate of $3.7\,10^{-7}\,\mathrm{s^{-1}}$, which is $\sim 3.5\,\%$ less than the rate calculated for the

[6]Throughout this chapter, we refer to various quantities as "adjusted" meaning that we take their magnitudes scaled by r^2, i.e., multiplied by the square of solar distance expressed in AU.

unenhanced and undecelerated solar wind. Hence, the modification of the charge exchange rate in the outer supersonic solar wind from the $1/r^2$ decrease is on the order of the uncertainty related to the averaging and approximating the charge exchange rate or less.

The remaining issue is whether or not using Eq. 3.14 to calculate the charge exchange rate of neutral H with pickup ions is justified. Pickup ions in the supersonic solar wind make a special case in the calculation of the charge exchange rate. Even though their bulk speed is equal to the solar wind expansion speed, the width of their distribution function is comparable to the magnitude of the expansion speed (Vasyliunas and Siscoe 1976; Möbius et al. 1988) and consequently the full version of the formula for the charge exchange rate, defined in Eq. 3.12, should in principle be used.

The simplification of using Eq. 3.14 for pickup ions seems acceptable because it is not expected to introduce major errors. Close to the Sun (within ~ 10 AU), their abundance in the solar wind is small and consequently their contribution to the total charge exchange rate is negligible. Outside of this region, their content in the solar wind increases, but the total charge exchange rate becomes small. Consequently, the contribution of charge exchange operating in this region of space to the total losses of neutral interstellar gas observed from the inner heliosphere, especially via helioglow measurements, is also small. Another issue in the calculation of charge exchange rate may be departures of the solar wind flow from purely radial expansion at larger heliocentric distances, which could result in a change of the latitudinal structure with solar distance, as suggested by Fahr and Scherer (2004). Detailed studies to support this qualitative discussion are missing in the literature, as far as we know, except for some insight provided by Bzowski and Tarnopolski (2006) on the radial profiles of survival probabilities of ENAs approaching the Sun.

In our opinion, consistently taking all these effects into account would require using a comprehensive, multi-fluid, three-dimensional and time-dependent model of solar wind. Such a model should include the core solar wind, electrons, and pickup ions as well as the solar wind magnetic field and be able to address both the large-scale behavior of the solar wind flow and small-scale disturbances such as turbulence. As boundary conditions, it should take actually and continuously measured solar wind parameters as close to the corona as practical. To our knowledge, such a model is now in development (see Usmanov et al. 2011 and references therein).

Photoionization

From Solar Spectrum to Photoionization Rate

Photoionization is a secondary ionization factor of neutral interstellar H, but its significance has recently increased because of the decrease in the average solar wind flux observed since the last solar maximum (see upper panel in Fig. 3.8). This has resulted in a decrease in the intensity of the dominant charge exchange ionization rate.

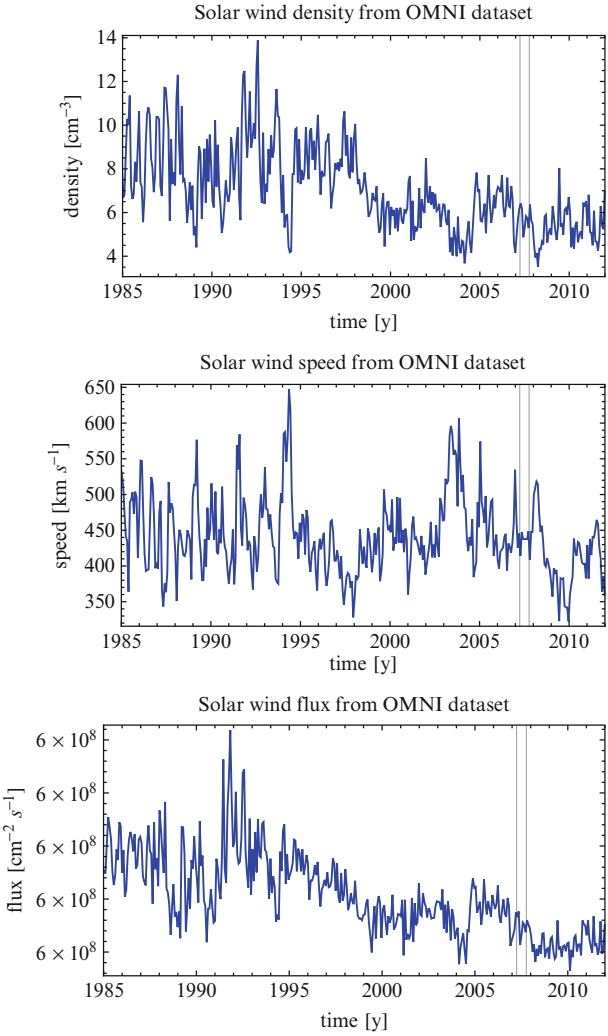

Figure 3.8: Carrington rotation averages of solar wind density adjusted to 1 AU (*upper panel*), speed (*middle panel*), and adjusted flux (*lower panel*) calculated from hourly averages from the OMNI-2 database (King and Papitashvili 2005). The *thin vertical lines* mark the time interval which is expanded to daily time cadence in Fig. 3.14

The rate of photoionization $\beta_{\mathrm{ph}}(t)$ at a time t can be calculated from the formula:

$$\beta_{\mathrm{ph}}(t) = \int_0^{\lambda_{\mathrm{ion}}} \sigma_{\mathrm{ph}}(\lambda)\, F_\lambda(\lambda, t)\, \mathrm{d}\lambda, \tag{3.21}$$

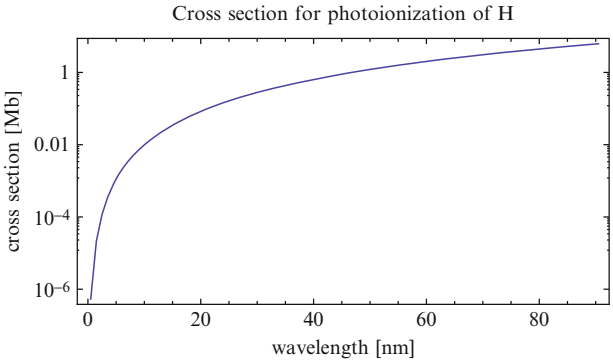

Figure 3.9: Cross section for hydrogen photoionization based on Eq. 3.22, adapted from Verner et al. (1996)

where $\sigma_{\mathrm{ph}}(\lambda)$ is the cross section for photoionization for wavelength λ and $F_\lambda(\lambda, t)$ is the solar spectral flux at the time t and wavelength λ. λ_{ion} is the wavelength for the threshold ionization energy. In the case of hydrogen, the spectral range of the radiation capable of knocking out electrons from H atoms is entirely in the EUV range. The cross section for photoionization of H can be expressed by the following formula (Verner et al. 1996):

$$\sigma_{\mathrm{Hph}}(\lambda) = 6.82297 \times 10^{-10} \left(\frac{9.36664}{\sqrt{\lambda}} + 1 \right)^{-2.963} (\lambda - 2,884.69)^2 \, \lambda^{2.0185}, \quad (3.22)$$

where the cross section is expressed in megabarns (Mb), wavelength in nm, and $\lambda \leq 91.18\,\mathrm{nm}$. The cross section is shown in Fig. 3.9, and the importance of various portions of the spectrum for the photoionization is illustrated in Fig. 3.10. It shows the integrand function from Eq. 3.21 for day of year 122 in 2001 (Bochsler et al. 2012).

It is clear from Fig. 3.10 that the most important portion of the spectrum for the photoionization of hydrogen is the one immediately above the photoionization threshold. The photoionization rate varies because the solar EUV spectral flux varies. Direct measurements of the solar EUV spectrum in the entire relevant energy range have been available on a 2-hourly basis since 2002, when the TIMED/SEE experiment (Woods et al. 2005) was launched. Before then, the spectral coverage was intermittent and one had to resort to indirect methods to estimate the solar EUV flux.

Basically, these methods can be grouped into two classes: (1) direct integration using Eq. 3.21 with the spectrum $F_\lambda(\lambda, t)$ calculated from proxies, and (2) using correlation formulae between selected proxies and photoionization rates obtained for the times when the spectrum measurements are available. Since measurements covering only a portion of the spectrum with a relatively low spectral resolution are also available (CELIAS/SEM onboard SOHO; Hovestadt et al. 1995; Judge et al. 1998), a variant of method (2) would require finding a correlation between these partial direct measurements and the photoionization rate. Neither of the methods

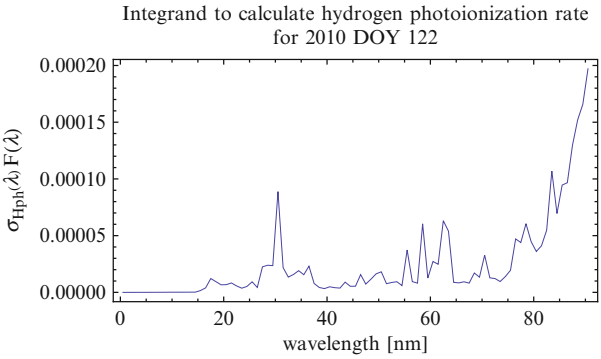

Figure 3.10: Integrand function from Eq. 3.21 for the flux obtained from TIMED/SEE for 2010 DOY 122. The photoionization cross section used is defined in Eq. 3.22 and shown in Fig. 3.9

gives perfect results. Furthermore, a reliable application of method (2) became possible only after a sufficiently rich database of precise measurements of the solar spectrum became available.

Inspection of Fig. 3.10 shows that the band from 50 to 30 nm, which is the most relevant for helium and has been observed by CELIAS/SEM, is of secondary significance for hydrogen. Since, however, variations in various portions of the solar EUV spectrum are correlated to some extent, the evolution of the EUV flux in the CELIAS/SEM bands is a reasonable indicator of the evolution of the photoionization rates of H as well (Bochsler et al. 2012).

Using method (1) requires a proxy model of the solar spectrum in the relevant photon energy range. A number of such models were developed in the past, including SERF1 (also known as HFG or EUV81; Hinteregger et al. 1981), EUVAC (Richards et al. 1994), SOLAR2000 (Tobiska et al. 2000), and NRLEUV (Warren et al. 1998a,b; Lean et al. 2003; Warren 2006). These solar proxy models are based on empirical correlations found between various portions of the solar spectrum and selected time series of available measurements, including typically the $F_{10.7}$ radio flux, the $MgII_{c/w}$ index, the solar Ca II K index, and even the sunspot time series. The methodology and problems of creation of such models have been recently reviewed by Floyd et al. (2002, 2003, 2005) and Lean et al. (2011). The question of finding suitable proxies has been discussed by Kretzschmar et al. (2006); Dudok de Wit et al. (2005, 2008, 2009). Typically, linear correlations have been sought, but they do not seem to be optimum representations of the true correlations in some cases (Bochsler et al. 2012) as is shown in the following subsection.

Temporal Variation in the Photoionization Rate of Hydrogen in the Ecliptic Plane

The process of photoionization of heliospheric hydrogen was extensively discussed by Ogawa et al. (1995) and we will not repeat such a discussion in this chapter. We briefly present current views on the rate of photoionization of

heliospheric hydrogen based on both measurements and models. Bochsler et al. (2012) developed a model of evolution of the Carrington period averages of the hydrogen photoionization rates that is based on directly measured solar spectra from TIMED/SEE and a hierarchy of proxies. From the spectra at full time resolution, available from 2002 until present, the photoionization rates were calculated using Eq. 3.21. Since the time series obtained showed clear signatures of flares and local particle-background contamination, it was filtered against the outliers beyond two sigmas that show up in the time series of change rates $(\beta(t_{i+1}) - \beta(t_i)) / (t_{i+1} - t_i)$. Monthly averages were computed from the filtered time series, which are shown in red in the lower panel of Fig. 3.11.

The TIMED/SEE coverage is limited in time, but intercalibrating or comparing various measurements in the heliosphere taken at different times requires knowledge of homogeneously-derived time series of ionization rates. Thus a hierarchy of proxies was used to extend backwards in time the directly-obtained photoionization rates. The proxy-based time series is available until the end of 1947, when the measurements of the $F_{10.7}$ flux became available.

Bochsler et al. (2012) started from directly integrated photoionization rates calculated from the filtered TIMED spectra, which cover the full interval from solar maximum to solar minimum. They calculated a time series of monthly averages and found a correlation formula between these values on one hand and Carrington rotation averaged measurements in Channel 1 SEM_{Ch1} and Channel 2 SEM_{Ch2} from CELIAS/SEM and the time series of Lyman-α flux I_{tot} from LASP on the other hand. This formula is the following:

$$\begin{aligned} \beta_{Hph} &= 5.39758 \times 10^{-20}\, I_{tot} + 2.36415 \times 10^{-16}\, SEM_{Ch1}^{0.765549} + \\ &+ 3.98461 \times 10^{-16}\, SEM_{Ch2}^{0.765549} + 2.05152 \times 10^{-8}. \end{aligned} \tag{3.23}$$

Using this formula, Bochsler et al. (2012) calculated the Carrington averages of photoionization rates for the entire interval for which the SEM data were available. For the times when SEM data was unavailable, but the $MgII_{c/w}$ index from LASP was, they used another correlation formula:

$$\beta_{Hph} = 3.56348 \times 10^{-6}\, MgII_{c/w} - 8.5947 \times 10^{-7}. \tag{3.24}$$

For epochs where the $MgII_{c/w}$ index was unavailable, Bochsler et al. (2012) used the following correlation formula with the $F_{10.7}$ flux expressed in sfu units (i.e., $10^{-22}\,W\,m^{-2}\,Hz^{-1}$):

$$\beta_{Hph} = 1.31864 \times 10^{-8}\, F_{10.7}^{0.474344} - 1.7745 \times 10^{-8}. \tag{3.25}$$

It is worth pointing out that the exponent at the $F_{10.7}$ flux is close to 1/2, not 1, as is frequently adopted. The results of the model with color coding of the sources used is shown in the lower panel of Fig. 3.11 for the time interval since 1990 until present.

The photoionization rate obtained in the way described above can be compared with the rate from the SOLAR2000 model, used extensively in previous studies (e.g. Bzowski et al. 2009). The comparison is shown in the upper panel of Fig. 3.11. The two models agree to about 10–15 %, with the direct integration model giving

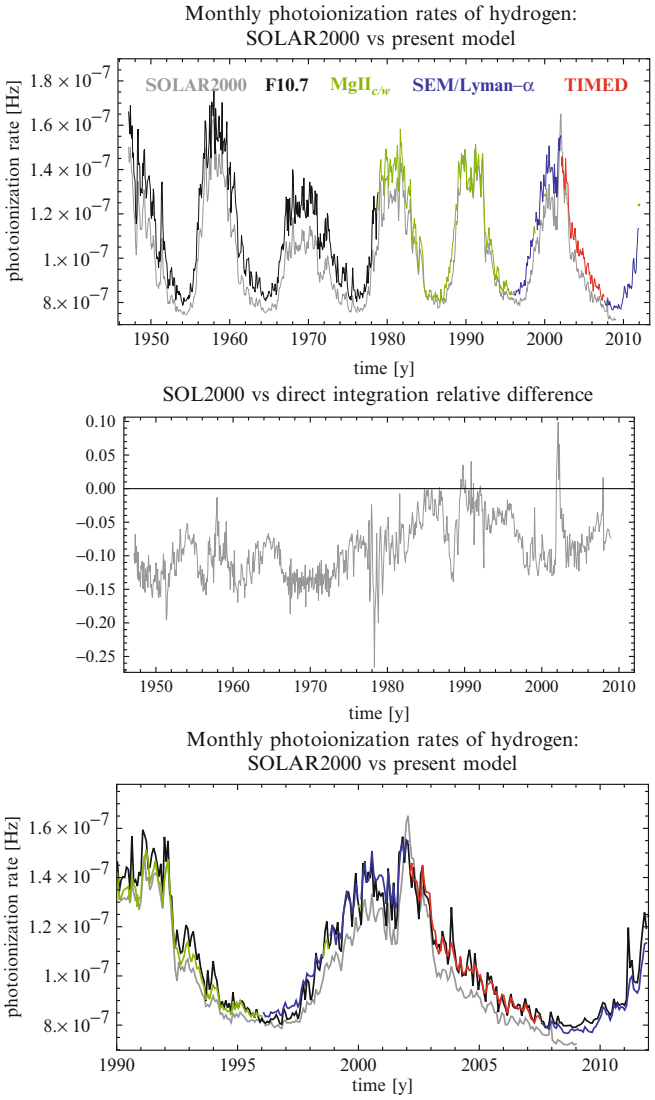

Figure 3.11: Comparison of the monthly averages of the hydrogen photoionization rate obtained from the SOLAR2000 (Tobiska et al. 2000) and direct-integration model, extended using the SEM/Lyman-α, Mg II$_{c/w}$, and $F_{10.7}$ proxies (Bochsler et al. 2012) in the *upper panel*. Relative difference between the SOLAR2000 and the Bochsler et al. models are shown in the *middle panel*. Exploded view of the photoionization rate from the Bochsler et al. (2012) multi-proxy model during the two past solar cycles is shown in the *lower panel*. In this panel one can assess the agreement of the multi-proxy model by Bochsler et al. (2012) with their model solely based on the $F_{10.7}$ proxy and with the ionization rate obtained from SOLAR2000. The color code, common for the upper and lower panels, is shown in the upper panel

almost always higher values. Such an accuracy is basically equal to the present accuracy of the EUV measurements, especially in the low-energy portion of the spectrum which contributes most to the ionization.

It seems that the cause of these small discrepancies is the difference in the way the photoionization rates are calculated by SOLAR2000 and by Bochsler et al. (2012). SOLAR2000 first calculates the solar spectrum from their sophisticated system of proxies and then integrates the spectra to yield the ionization rate. The quality of the derived spectrum seems to worsen when going backwards in time. This is understandable because it is gradually based on fewer available measurements of solar proxies. Bochsler et al. (2012) used measured solar spectra for the time intervals when they were available and the absolute calibration was most credible. For other times they used proxies and correlation formulae specially developed to connect a proxy measurement with the photoionization rate of a given species. In this sense, technically, it is not a hierarchy of proxies, where one proxy model is based on another proxy model. Rather, it is a collection of proxy models, which all are based on one reliable series of direct measurements.

The lower panel of Fig. 3.11 presents the best estimate of the hydrogen photoionization rate obtained by Bochsler et al. (2012) from their collection of proxies (the colored line) with the rate calculated solely from the $F_{10.7}$ proxy (black line) and with the rate presented by SOLAR2000 (gray line). Particularly interesting is the comparison of the model from the $F_{10.7}$ proxy with the results of direct integration of the solar spectrum (red vs black line), and with the SOLAR2000 results. While the $F_{10.7}$ proxy model exactly tracks the direct rate, showing only some departures above or below the red line, SOLAR2000 is consistently below.

Also outside the interval when the direct TIMED spectra could be used, the $F_{10.7}$ proxy model tracks quite well the best proxy model of Bochsler et al. (2012), which leads us to believe that the system developed by these authors is self-consistent and reliable, unless the relation of the $F_{10.7}$ radio flux to the solar EUV spectrum changed between 1948 and 1979, when the Mg $II_{c/w}$ proxy became available. We are not aware of any such change described in the literature.

On the other hand one has to remember that the model by Bochsler et al. (2012) is only able to calculate Carrington period averages of the ionization rate of hydrogen and a few other selected species (He, O, Ne), while SOLAR2000's ambition is to provide an estimate for an arbitrarily selected day within its validity interval. In fact, it allows one to calculate the ionization rate of any species since it produces an approximate solar spectrum at a resolution of 1 nm. Given all the challenges it has to face, it seems to be doing it remarkably well.

Latitude Variation of the Photoionization Rate

Just as for the solar Lyman-α radiation, radiation in the spectral region relevant for photoionization is also expected to vary with heliolatitude. Auchère et al. (2005b) constructed a model of equatorial and polar flux in the solar 30.4 nm line, mostly responsible for ionization of helium, and demonstrated that a ~ 0.8 pole-to-equator ratio (fluctuating) can be expected. A similar modeling for the spectral range relevant for photoionization of hydrogen is not available, but coronal observations by Auchère et al. (2005a) suggest that such an anisotropy can indeed

be expected and that some north-south asymmetry cannot be ruled out. In the absence of a complete model and sufficient data we surmise that a latitude variation of hydrogen photoionization rate approximated by a formula similar to Eq. 3.4 may be tentatively adopted. The subject certainly needs further studies.

Electron Ionization

The significance of the electron-impact ionization reaction for the distribution of neutral interstellar gas in the inner heliosphere was pointed out by Ruciński and Fahr (1989), who developed a model of the electron ionization rate based on the local electron temperature and density. Further insight into the problem of electron-impact ionization of neutral interstellar hydrogen inside the heliosphere can be found in Bzowski et al. (2008) and Bzowski (2008).

The ionization rate in the electron-impact reaction at a location described by the radius-vector $\boldsymbol{r}$ can be calculated from the following formula (Owocki et al. 1983):

$$\beta_{\mathrm{el}}(\boldsymbol{r}) = \frac{8\pi}{m_{\mathrm{e}}^2} \int\limits_{E_{\mathrm{ion}}}^{\infty} \sigma_{\mathrm{el}}(E)\, f_{\mathrm{e}}(E, \boldsymbol{r})\, E\, \mathrm{d}E, \tag{3.26}$$

where σ_{el} is the energy-dependent reaction cross section, E the collision energy and E_{ion} the ionization threshold energy. For hydrogen, E_{ion} equals $\sim 13.6\,\mathrm{eV}$. Ionization occurs for the H atom—electron collisions with energies exceeding the limiting energy E_{ion}. Practically, almost all of the energy of the electrons in the solar wind at a few AU from the Sun is in thermal motions.

The kinetic energy of an electron moving at a typical solar wind expansion speed of $440\,\mathrm{km\,s^{-1}}$ is about 0.5 eV, which is much less than the ionization threshold. Since the temperature of the electron fluid at 1 AU is on the order of $\sim 10^5$–$\sim 10^6\,\mathrm{K}$, the thermal speeds of the solar wind electrons are on the order of a few thousand of $\mathrm{km\,s^{-1}}$, which strongly exceeds the expansion speed. Thus, the expansion speed of the electron fluid can be neglected in the calculation of the electron-impact ionization rate.

The formula for the cross section for electron ionization was proposed by Lotz (1967b) and simplified for H by Lotz (1967a):

$$\sigma_{\mathrm{el}}(E) = \sum_{i=1}^{N_A} \frac{a_i q_i \ln\left(\frac{E}{P_i}\right)\left(1 - b_i \exp\left[-c_i\left(\frac{E}{P_i} - 1\right)\right]\right)}{E P_i}, \tag{3.27}$$

where N_A is the number of electrons per ion and the summation goes over the partial cross sections for knocking out all individual electrons from the ion. P_i is the ionization potential for a given charge state of the ion, E is the impacting electron energy, a_i, b_i, c_i are parameters specific to a given ion and its charge state, and q_i is the statistical weight. For hydrogen, there is only one electron to be knocked out and Eq. 3.27 takes the form:

$$\sigma_{\mathrm{el}}(E) = 4.0 \times 10^{-14}\left(1 - 0.60 \exp\left[-0.56\left(\frac{E}{13.6} - 1\right)\right]\right)\frac{\ln(E/13.6)}{13.6E}, \tag{3.28}$$

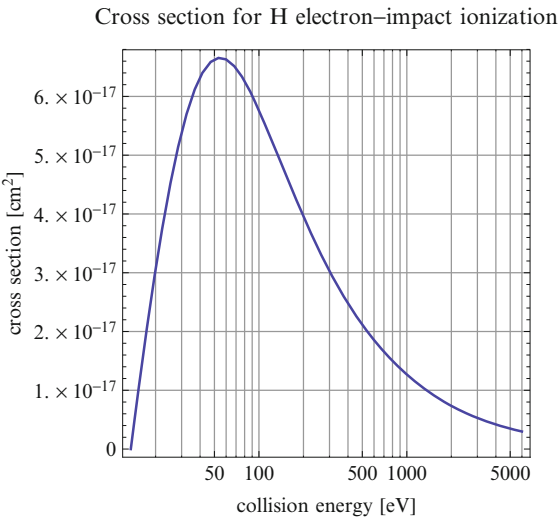

Figure 3.12: Cross section for electron-impact ionization of hydrogen, defined in Eq. 3.26 from Lotz (1967a), as a function of H atom–electron collision energy in eV

where $E \geq 13.6$ is expressed in eV. It is claimed by Lotz (1967a) to be accurate to $\sim 10\,\%$ and shown in Fig. 3.12.

The electron density can be estimated from quasi-neutrality and continuity conditions in the solar wind and calculated from the formula:

$$n_e = n_p \left(1 + 2\xi_\alpha\right), \tag{3.29}$$

where ξ_α is the local alpha-particle abundance relative to solar-wind protons. The temperature behavior is much less simple. The distribution function of electrons in the solar wind and its evolution with solar distance is fairly complex and requires further studies. Note that measurements performed on Ulysses using two different techniques—Quasi Thermal Noise (Issautier et al. 2001) and particle-measurements (Salem et al. 2001)—return somewhat discrepant results (Issautier 2009). Basically, the electron distribution function can be decomposed into three components: a warm core of $\sim 10^5$ K; a hot halo of $\sim 10^6$ K; and a fluctuating strahl, stretched along the local magnetic-field direction (Pilipp et al. 1987a,b).[7]

The core and halo can both be approximated by a Maxwellian function:

$$f_e\left(\boldsymbol{r}, T_e, E\right) = n_e \left(\frac{m_e}{2\pi\, k_B\, T_e\left(\boldsymbol{r}\right)}\right)^{3/2} \exp\left[-\frac{E}{k_B\, T_e\left(\boldsymbol{r}\right)}\right], \tag{3.30}$$

where k_B is the Boltzmann constant, m_e the electron mass, E the kinetic energy of electron, T_e the temperature of the electron fluid, and $\boldsymbol{r}$ the radius-vector of the

[7]Note that the electron distribution function can be approximated by the kappa function—originally by Maksimovic et al. (1997) and recently by Le Chat et al. (2010, 2011)—which naturally covers both the core and halo components.

location in space. The contribution of the halo population to the net rate is on the level of a few percent and is an increasing function of the heliocentric distance (Maksimovic et al. 2005; Štveràk et al. 2009). Estimates by Bzowski et al. (2008) show that at 1 AU, the ionization rate due to the core population of the solar wind electrons is equal to about $0.4 \times 10^{-7}\,\mathrm{s}^{-1}$ and to the halo population less than $0.04 \times 10^{-7}\,\mathrm{s}^{-1}$, respectively. The amplitude of fluctuations in the electron ionization rate may reach one order of magnitude, which is much more than the long-time variations related to variations in solar activity. On the other hand, the electron data from WIND (Salem et al. 2003) imply an in-ecliptic solar minimum (1995) electron ionization rate of $\sim 0.68 \times 10^{-7}\,\mathrm{s}^{-1}$ and a solar maximum (2000) rate of $\sim 0.73 \times 10^{-7}\,\mathrm{s}^{-1}$. Thus, assuming a constant electron ionization rate over the solar cycle is a reasonable approximation.

Observations done with Ulysses (Phillips et al. 1995a; Issautier et al. 1998; Le Chat et al. 2011) suggest that the electron ionization rate is a 3D, time dependent function of the solar cycle phase. Both the temperature magnitude and the cooling rate differ between the fast and slow solar wind. Bzowski (2008) adopted the following radial profiles of the core T_c and halo T_h temperatures and the halo-to-core density ratios $\xi_{hc} = n_h/n_c$ for the slow solar wind (after Scime et al. 1994):

$$\begin{aligned} T_c &= 1.3 \cdot 10^5\, r^{-0.85} \\ T_h &= 9.2 \cdot 10^5\, r^{-0.38} \\ \xi_{hc} &= 0.06\, r^{-0.25} \end{aligned} \tag{3.31}$$

and for the fast solar wind (after Issautier et al. 1998; Maksimovic et al. 2000):

$$\begin{aligned} T_c &= 7.5 \cdot 10^4\, r^{-0.64} \\ T_h/T_c &= 13.57 \\ \xi_{hc} &= 0.03. \end{aligned} \tag{3.32}$$

In both solar wind regimes, the core n_c and halo n_h densities are calculated from the equations:

$$\begin{aligned} n_c &= \frac{1 + 2\xi_\alpha}{1 + \xi_{hc}}\, n_p \\ n_h &= \xi_{hc}\, n_c, \end{aligned} \tag{3.33}$$

with the solar wind alpha abundance $\xi_\alpha = 0.04$, adopted to be identical in both fast and slow wind regimes. n_p in this expression is the proton density. We adopt it as velocity-independent because it introduces a relatively small modification to the electron density, even though Kasper et al. (2012) show variations of this quantity with solar activity as a function of solar wind speed.

Ruciński and Fahr (1989) inserted the formulae from Eqs. 3.27, 3.29, and 3.30 to the integrand function in Eq. 3.26 and obtained a formula for each of the terms i contributing to the total electron-impact cross section, which we present here in a slightly modified form:

$$\beta_{\mathrm{el},i}\,(T_e) = n_e\, \frac{a_i\, q_i}{m_e\, P_i} \sqrt{\frac{8\, m_e}{\pi\, k_B T_e}} \left(\Gamma\left(0, \frac{P_i}{k_B T_e}\right) - \frac{\Gamma\left(0, c_i + \frac{P_i}{k_B T_e}\right) \exp\left[c_i\right]\, b_i P_i}{P_i + c_i\, k_B T_e} \right), \tag{3.34}$$

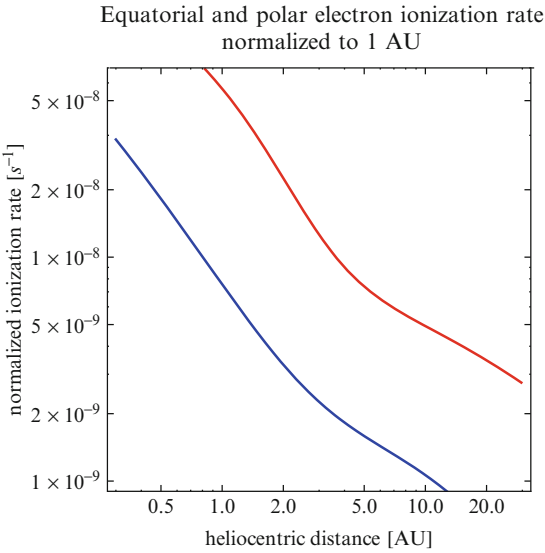

Figure 3.13: Normalized radial profiles $r^2\,\beta_{\rm el}\,(r)$ of the equatorial (*red*) and polar (*blue*) rates of electron-impact ionization of neutral interstellar H atoms in the supersonic solar wind, defined by Eqs. 3.35 and 3.36, respectively (adapted from Bzowski 2008). Since those rates are calculated based on measurements performed between 0.3 and 5.5 AU from the Sun, their validity is limited to this distance range

where $\Gamma(a, z)$ is the incomplete gamma function and for hydrogen $i = 1$, $q_i = 1$, $P_i = E_{\rm ion} = 13.6\,{\rm eV}$, $a_i = 4.0 \times 10^{-14}$, $b_i = 0.60$, $c_i = 0.56$.

Using these relations, Bzowski (2008) employed the approach proposed by Ruciński and Fahr (1989), assuming that the core and halo temperatures are isotropic, which is not exactly the case, as shown by Štverák et al. (2008), and calculated radial profiles of the electron-impact ionization rates separately for the fast and slow solar wind. Subsequently, they approximated the results by the following phenomenological formulae, which are valid between ~ 0.3 and ~ 5 to 10 AU:

$$\beta_{\rm el,s}\,(r, n_p) \;=\; \frac{n_p}{r^2}\,\exp\left[\frac{\ln r\,(541.69\ln r - 1,061.32) + 1,584.32}{(\ln r - 29.17)\,((\ln r - 2.02)\ln r + 2.91)}\right] \qquad (3.35)$$

$$\beta_{\rm el,f}\,(r, n_p) \;=\; \frac{n_p}{r^2}\,\exp\left[\frac{\ln r\,(348.73\ln r - 917.39) + 2,138.05}{(\ln r - 18.97)\,((\ln r - 2.53)\ln r + 5.74)}\right]. \qquad (3.36)$$

As is evident in these formulae, the electron-impact ionization rates are parametrized by local proton densities n_p normalized to 1 AU and are fixed functions of heliocentric distance, which differ appreciably from the $1/r^2$ profiles that are typical of the solar wind flux and photoionization rate. An illustration of the departure of the electron-impact ionization rate from $1/r^2$ behavior is shown in Fig. 3.13.

The behavior of the electron temperature in the compressed solar wind resulting from stream-stream interactions is not easily modeled and thus the behavior of the

electron ionization rate in this solar wind regime is poorly known. Bzowski (2008) approximated the electron ionization in the solar wind of intermediate velocity as a weighted mean value between the rates specific for the fast and slow wind.

The differences in the electron fluid parameters and their variation with solar distance, as well as the differences between the electron fluids in the fast and slow wind result in a pronounced latitude anisotropy of the electron ionization rate throughout the solar cycle. An exception is a brief interval at solar maximum, when the solar wind becomes almost spherically symmetric.

The significance of the electron impact ionization in the overall balance of the contributing ionization reactions increases towards the Sun. Eventually, the role of electron ionization and its anisotropy is greater in the downwind hemisphere, where neutral interstellar gas has already passed the Sun (i.e., the streamlines of the H gas flow have passed their perihelia).

Because of the fast cooling of the electron fluid with solar distance, electron-impact ionization almost negligibly affects the distribution of neutral interstellar hydrogen in the upwind hemisphere at the distances beyond ~ 2 AU (Tarnopolski and Bzowski 2008b). This distance seems to be close to the distance to the Maximum Emissivity Region of the heliospheric Lyman-α backscatter glow.[8] Hence, the limited validity range of the formulae specified in Eqs. 3.35 and 3.36 seems to not hinder modeling of the effective ionization rate of heliospheric neutral atoms at larger distances from the Sun within the supersonic solar wind.

Summary of the Variations in the In-ecliptic Ionization Rates

A summary of the variations in the in-ecliptic ionization rates of hydrogen, scaled to 1 AU, is presented in Fig. 3.7 for a time interval from 1970 through the end of 2011. Charge exchange with solar wind protons dominates, photoionization is the next largest rate, and electron ionization is the third. The total ionization rate does not seem to be a periodic function with a period close to the solar cycle period, even though one of the components, the photoionization rate, does feature a strong solar cycle periodicity. Rather, a much longer periodicity may be guessed. On the time scale of spaceborne solar EUV measurements, a secular decrease in the total ionization rate by about 30 % between 1980s and 1990s and the present decade is observed.

Evolution of Solar Wind in the Ecliptic Plane

The existence of the solar wind was theoretically predicted by Parker (1958) and experimentally discovered at the very beginning of the space age, when the spacecraft Lunnik II and Mariner 2 had left the magnetosphere (Gringauz et al. 1960; Neugebauer and Snyder 1962). Regular measurements of solar wind parameters started in the beginning of the 1960s and up to now, data from more than

[8]The Maximum Emissivity Region is by definition the region where the maximum of the source function for the Lyman-α backscatter glow is located.

20 spacecraft have been available, obtained using various observations and data processing techniques.

The highly supersonic solar wind in the ecliptic plane consists of a sequence of various interleaved components: a "genuine" slow solar wind, a fast solar wind, solar wind plasma from stream-stream interaction regions, and (intermittently) interplanetary coronal mass ejections (CME). The Mach number of the flow at 1 AU varies from ~ 3 to ~ 10. The balance between the populations varies with solar activity.

Historically, measurements of the solar wind speed obtained from various experiments generally agreed among themselves with an accuracy of $\sim 5\,\%$, but systematic differences between density values from different experiments up to $\sim 30\,\%$ existed (for extensive discussion, see the OMNIWeb documentation at http://omniweb.gsfc.nasa.gov/html/omni2_doc.html). Hence any study of a long-term behavior of the solar wind required intercalibration of the results from different experiments. Such an initiative brought the OMNI data collection [King and Papitashvili available at at http://omniweb.gsfc.nasa.gov/]; see also King and Papitashvili (2005) where historical and present measurements of the solar wind density, velocity, temperature, alpha abundance, and magnetic field vector were brought to a common calibration.

Originally, the OMNI collection was created in the 1970s by the National Space Science Data Center (NSSDC) at the NASA Goddard Space Flight Center. In 2003, a successor database OMNI-2 was made available, which has been maintained until present. The OMNI-2 data collection was the basis for the present study of solar wind parameters in the ecliptic and is used in this chapter to construct the charge exchange ionization rates.

The early period of the OMNI databases (1963–1971) includes data from multiple spacecraft (Bonetti et al. 1969; Neugebauer 1970), the middle-period data are mostly from IMP-8 and span from 1971 to 1994, and the later periods, from 1994 until present, include mostly data from IMP-8, or the WIND Solar Wind Experiment (SWE) (Kasper 2002), and ACE/SWEPAM (McComas et al. 1998a).

Since there was no overlap between the early and middle period, the data from the early period in the OMNI-2 database are adopted unchanged from the original OMNI collection. The data obtained from various spacecraft during the early period were extensively intercalibrated, but no intercalibration with the middle and recent periods was possible. Still, owing to the overlap of the data between the middle and recent periods, it was possible to perform an intercalibration between the data from these two periods.

It is important to mention the significance of the correlation work that the OMNI team performed on the data from the IMP-8 spacecraft and early WIND and ACE measurements. IMP-8 operated for 28 years from 1973 to 2001 and provided a bridge between the early and present observations, enabling the presentation of a more or less homogeneous series of solar wind parameters shown further down in this chapter.

Most of the solar wind plasma data used in the OMNI collection were obtained from the MIT Faraday Cups (Bridge et al. 1965; Lyon et al. 1967, 1968; Lazarus and Paularena 1998) and LANL electrostatic analyzers (Bame et al. 1971, 1978a,b; Hundhausen et al. 1967; Ogilvie et al. 1968; Feldman et al. 1973; Asbridge et al. 1976; McComas et al. 1998a). In the OMNI-2 series, King and Papitashvili

(2005) adopted measurements of solar wind parameters performed by the WIND spacecraft as basis for the common calibration. They followed in this respect an analysis performed by Kasper (2002) and Kasper et al. (2006). The latter paper includes a comprehensive, physics-based analysis of the accuracy of solar wind measurements, especially of the measurements performed using the WIND spacecraft Faraday cups.

The preparation of the data published in the OMNI collection involves removing potential Earth bow shock contamination and incomplete records from the original high-resolution data supplied by the Principal Investigators of the experiments, and subsequently time-shifting the data from the spacecraft location to the Earth.

The primary source of the solar wind data are currently WIND measurements, but they are being superceded by measurements from the Advanced Composition Explorer (ACE). These, unlike the data from WIND, are free from possible bow shock contamination because the ACE spacecraft operates near the Earth at a Lissajous orbit close to the L1 Lagrange point about a million kilometers upstream of the Earth's bow shock.

Because of different time scales of the processing of the data from various spacecraft, typically an interim data product becomes available once the first data are obtained, which is superseded with the final product when all the data needed become available or are declared as unavailable. This results in some updates to the published records over time. Our experience shows, however, that the changes are seldom significant for the Carrington averages.

The data from different experiments are scaled to a common calibration using linear fits based on results of linear regression analysis. The result of the intercalibration process is a time series of hourly-averaged solar wind parameters. Because of the varying quality of individual records, the time coverage of the parameters is not uniform and gaps may exist in some parameters, while correct data for the same time interval may be available for others.

Since the distribution function of solar wind is inhomogeneous and varies rapidly in time, the values of solar wind parameters retrieved from observations depend on the method used to process the data. Typically, the LANL team take moments of the observed distribution function to calculate the density, speed and temperature of the solar wind, while the MIT team fit the measurements to an anisotropic Maxwellian or bi-Maxwellian function using a nonlinear fit method. To assess differences resulting from the two aforementioned approaches, the MIT team calculated the density, speed and temperature from the WIND/SWE distributions using both methods.

King and Papitashvili at http://omniweb.gsfc.nasa.gov/html/omni2_doc.html extensively discuss the differences and correlations between data from various sources. They show that the velocities are very well linearly correlated, with the coefficients of the relation $v_{\mathrm{SWE}} = a + b\, v_{\mathrm{ACE}}$ equal to $a = -2.135 \pm 0.387$ and $b = 1.010 \pm 0.001$.

In the case of densities, it is the logarithms of density which are linearly correlated and the coefficients of the formula $\log n_{\mathrm{SWE}} = a + b \log n_{\mathrm{ACE}}$ slowly vary with speed, a changing from 0.006 for $v < 350\,\mathrm{km\,s^{-1}}$ to 0.091 for $350 < v < 450\,\mathrm{km\,s^{-1}}$ to 0.082 for $v > 450\,\mathrm{km\,s^{-1}}$ and b changing from 1 for $v < 350\,\mathrm{km\,s^{-1}}$ to 1.036 for $350 < v < 450\,\mathrm{km\,s^{-1}}$ to 1 for $v > 450\,\mathrm{km\,s^{-1}}$.

This leads to differences on the order up to 20 % between ACE and WIND, which are comparable to the uncertainty in density coming up from the application of various methods of parameter derivation discussed earlier. In a nutshell, while a very good correlation of speeds is obtained, the correlation between the logarithm of the densities is close to linear, but with a scatter of approximately 30 % around the fit line. This is probably a good measure of the inherent uncertainty of the densities even without taking into account the uncertainties in the absolute calibrations.

Based on the OMNI database, we constructed a time series of Carrington period-averaged parameters of the solar wind normalized to 1 AU, with the grid points set precisely at halves of the Carrington rotation intervals. Small deviations of the times from the halves of the rotation periods were linearly interpolated. Averaging over the Carrington rotation enables the construction of a consistent, axially symmetric model of the ionization rate. The time series of density, velocity, and charge exchange rate in the approximation of neutral H atoms stationary relative to the Sun is presented in Fig. 3.8. The daily averaged values for density and speed of the solar wind for a much shorter time interval is shown in Fig. 3.14.

The time interval shown in Fig. 3.15 starts before the solar activity minimum in 1986 and includes the solar minima of 1995 and 2007, as well as the two recent maxima of 1990 and 2001. One observes a striking difference in the appearance of the solar wind equatorial parameters in comparison with the behavior of solar EUV radiation (compare Fig. 3.8 with Fig. 3.1; see also the behavior of the charge exchange rate contrasted with the photoionization rate in Fig. 3.7). Neither density nor speed seem to be correlated with the level of solar activity. There is no clear minimum–maximum–minimum variation, which is clearly seen in the EUV-related time series. Speed shows multi-timescale variations, but its mean value is basically constant over time.

By contrast, the density features a secular change, which begun just before the last solar maximum and leveled off shortly before the present minimum. The overall drop in the average solar wind density is on the order of 30 % between 1998 and 2005. Thus the solar wind density features a "plateau" until 1998, then a "cliff" and a "foot" starting from 2002. Within the "foot," density fluctuations seem to exist that are anticorrelated with solar wind speed. These can be associated with the persistence of coronal holes at equatorial latitudes, as convincingly illustrated by de Toma (2011).

The present rate of charge exchange (oscillating about $4\,10^{-7}\,\mathrm{s}^{-1}$, cf Fig. 3.15) is at a level similar to the charge exchange rate observed by Ulysses at the poles during its first fast latitude scan (Phillips et al. 1995a; McComas et al. 1999). The reduction relative to the pre-drop values of $\sim 6.5\,10^{-7}\,\mathrm{s}^{-1}$ is by $\sim 40\,\%$.

The overall long-standing drop in the ionization rate must result in an overall enhancement in the neutral interstellar gas density in the inner heliosphere (see, e.g., Bzowski et al. 2009 for the effects of various parameters on the behavior of this quantity). The secular variation of the solar wind, on time scales significantly longer than the solar cycle, suggest that the heliosphere does not evolve strictly periodically and that monitoring of these variations is an essential element of any effort aimed at a quantitative analysis of all kinds of heliospheric observations.

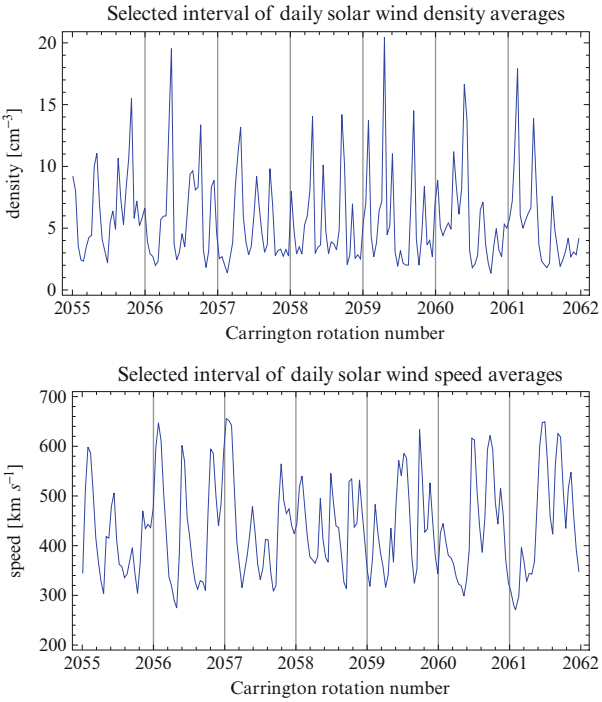

Figure 3.14: Daily averages of solar wind density adjusted to 1 AU (*upper panel*) and speed (*lower panel*) calculated from hourly averages obtained from the OMNI-2 database (King and Papitashvili 2005) for an example time interval covering 7 full Carrington rotation periods, presented to illustrate the complex structure of solar wind parameter evolution at different time scales and the approximate anticorrelation of density and speed. The interval shown covers 7 full Carrington rotations in 2008 and is placed in the context of long-term solar wind evolution shown in Fig. 3.8

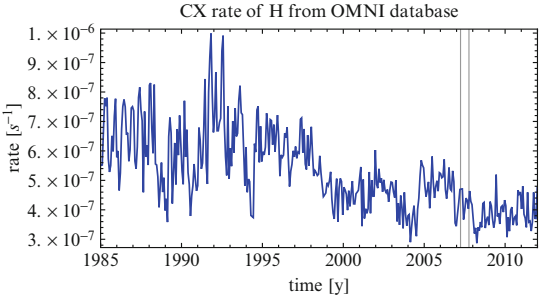

Figure 3.15: Carrington rotation averages of the rate of charge exchange between solar wind protons and neutral interstellar H atoms, calculated from monthly averages of solar wind speed and adjusted density using Eq. 3.19. The *thin vertical lines* mark the time interval expanded to daily time resolution in Fig. 3.14

Latitudinal Structure of the Solar Wind and Its Evolution During the Solar Cycle

Shortly after the discovery of the solar wind, the question of whether or not it is spherically symmetric appeared. The solar wind is currently known to feature a latitudinal structure which varies with the solar activity cycle. While direct observations of the solar wind in the ecliptic plane have been conducted since the early 1960s, information on its latitudinal structure was available only from indirect and mixed observations of the cometary ion tails (Brandt et al. 1972, 1975). The situation changed when radio-astronomy observations of interplanetary scintillation (IPS) and appropriate interpretation of observations of the Lyman-α helioglow became available. Apart from the in situ measurements obtained from Ulysses, these two techniques remain the only source of global, time-resolved information on the solar wind structure.

The launch of the Ulysses spacecraft (Wenzel et al. 1989), the first and up to now the only interplanetary probe to leave the ecliptic plane and sample interplanetary space in the polar regions, improved our understanding of the 3D behavior of the solar wind. Its measurements provided a very high resolution in latitude but a poor resolution in time. The same latitudes were visited only a few times during the $\sim$ 20-year mission at uneven time intervals. Hence the studies of solar wind parameters as a function of time and heliolatitude are still a work in progress and therefore are discussed in a separate section in this chapter.

Historical Perspective: Insight from Interplanetary Scintillation

Interplanetary scintillation measurements involve radiotelescope observations of remote compact radio sources (like quasars), searching for fluctuations of the signal. The variations are caused by the diffraction of radio waves on electron density fluctuations $\sim$ 200 km in diameter, occurring along the line of sight. Specifically, the observable quantity is called the scintillation index, defined as a quotient of the r.m.s. of the observed intensity fluctuation to the mean intensity of a source (Manoharan 1993).

The scintillation signal is the sum of waves scattered along the line of sight to the observed radio source. Most of the scattering occurs at the closest distances to the Sun along the line of sight because the strength of the electron density fluctuations rapidly decreases with solar distance. If the solar wind were spherically symmetric, it would be possible to define a weighting function and the IPS "midpoint" speed would be the spatial average of the solar wind speed centered at the closest point along the line of sight (Coles and Maagoe 1972). But the solar wind is not spherically symmetric and it features streams, which result in discrepancies of the measured speed from the actual one (Houminer 1971). Owing to a correlation between the fluctuations amplitude and the solar wind speed, it is possible to approximately deduce the solar wind speed from careful analysis of registered diffraction patterns in the observed radio source signal (Hewish et al. 1964).

An improvement in the accuracy of measurements of the solar wind speed was achieved from a better identification of the scintillation patterns along the lines of sight when they are simultaneously observed by multiple stations displaced longitudinally on the Earth surface, and by using the solar wind tomography technique (Jackson et al. 1997, 1998; Kojima et al. 1998; Asai et al. 1998). Despite the high sophistication of the tomography technique, its accuracy inevitably depends on geometrical considerations (the telescopes are located in the northern hemisphere of the Earth, whose orbit is tilted at an angle of 7.25° to the solar equator), on the number of available observations, and on the fidelity of the adopted correlation relationship between the solar wind speed and the density turbulence level.

While inferring the correlation between the solar wind speed and density fluctuations was achieved early on for the equatorial solar wind (Harmon 1975), the out-of-ecliptic IPS measurements could only be calibrated once in situ data from Ulysses became available (Kojima et al. 2001). Ideally, such a calibration should be repeated separately for each solar cycle because, as discussed earlier in this chapter, the solar wind features secular changes.

Early measurements of the solar wind speed using the IPS technique brought mixed conclusions: while Dennison and Hewish (1967) discovered an increase in solar wind speed outside the ecliptic plane, Hewish and Symonds (1969) did not find such an increase. Further observations, however, reported by Coles and Rickett (1976), clearly showed that the solar wind is structured, with a band of slow speed around the solar equator and a much faster wind near the poles.

An extensive program of IPS observations of the solar wind, initiated in the 1980s in the Solar-Terrestrial Environmental Laboratory at Nagoya University, Japan (Kojima and Kakinuma 1990), resulted in a homogeneous dataset that spans almost three solar cycles and enables studies of the evolution of the solar wind speed profile with changes in solar activity (Kojima and Kakinuma 1987). Even before the introduction of the Computer Assisted Tomography technique, they suggested that the solar wind structure varies with solar activity, with the slow wind reaching polar regions when the activity is high.

Supported and interpreted by the tomography technique (Hayashi et al. 2003), IPS observations enable detailed studies of the structure of the solar wind with varying solar activity conditions (Kojima et al. 1999, 2001, 2007; Ohmi et al. 2001, 2003; Fujiki et al. 2003a,b,c; Tokumaru et al. 2009, 2010). The solar wind speed data obtained from these observations are discussed later in this chapter.

Historical Perspective: Insight from Heliospheric Backscatter Glow

Observations of the Lyman-α heliospheric backscatter glow, carried out since the beginning of the 1970s (Bertaux and Blamont 1971) have also been used as a tool to discover the 3D structure of the solar wind and its evolution with the solar cycle. The bi-modal structure of the solar wind, with the slow and dense wind in an equatorial band and a rarefied, fast wind at the polar caps, results in a distinctly structured charge exchange ionization rate.

The direction of inflow of neutral interstellar gas is very close to the solar equator. Thus, the inflowing atoms that approach the Sun close enough to significantly

contribute to the backscattered signal and whose orbits happen to be in a plane close to the solar equator spend their entire travel through the heliosphere in the region of increased probability of ionization. In contrast, those traveling in planes inclined at greater angles to solar equator spend relatively little time in the equatorial band of the increased ionization rate or even do not get close to this region at all. Consequently, more of them are able to survive the travel towards the Sun (see Fig. 1 in Lallement et al. 1985a for an illustrative sketch). As a result, a region of reduced density of neutral interstellar hydrogen gas is created close to the solar equator. At higher heliolatitudes, the density of the gas at similar solar distances is higher than that within the equatorial band.

This gas is illuminated by an approximately spherically symmetric solar Lyman-α radiation, which is backscattered by resonance fluorescence. Since at equatorial latitudes the density of the gas is reduced and the illuminating flux is almost homogeneous in heliolatitude, the intensity of the backscattered radiation is lower at equatorial latitudes than at the polar caps. This equatorial dimming of the helioglow, referred to as the heliospheric groove, was observed in the 1970s and 1980s (Kumar and Broadfoot 1978, 1979; Lallement et al. 1985b, 1986; Lallement and Stewart 1990) and correctly interpreted as due to the enhanced ionization level at equatorial latitudes because of the anisotropy of the solar wind.

It is important to stress, however, that analysis of the heliospheric Lyman-α backscatter glow is only able to yield the latitude structure of the total ionization rate of neutral interstellar hydrogen. From the view point of density structure of neutral interstellar hydrogen near the Sun, the nature of the ionization processes is not important, only the results they produce, i.e. a decrease in the total density in an equatorial latitude band. Hence, no differentiation between the charge exchange, photoionization, and electron-impact ionization can be made based solely on the heliospheric glow analysis.

Since, however, charge exchange is the dominant process and photoionization is only slightly anisotropic in latitude, to first order the latitude variation in the total rate can be regarded as a latitude variation in the charge exchange rate, which is proportional to the latitude variation in the total solar wind flux, modulated by the dependence of the charge exchange rate on solar wind speed (see Eqs. 3.14 and 3.17).

Lallement et al. (1985a) proposed to describe the rate of charge exchange between the solar wind protons and neutral interstellar H atoms as a function of heliolatitude, ϕ, defined by the formula:

$$\beta_{\mathrm{CX}}(\phi) = \beta_0 \left(1 - A \sin^2 \phi\right). \tag{3.37}$$

This is a two-parameter relation, where β_0 corresponds to the rate at the equator and A is a pole-to-equator amplitude, which can be fit from observations of the helioglow. This formula approximately reproduced the limited observations of the groove obtained in the early stages of the research. It is able to reproduce various pole-to-equator contrasts in the ionization rate, as well as the situation when the contrast virtually disappears and the solar wind becomes almost spherically symmetric. However, the profile of the ionization rate obtained from this formula has a full width at half maximum $\sim 45^\circ$ and is perfectly symmetric about the solar equator. Consequently, it is not able to reproduce the north-south asymmetries in

the solar wind and the situations when the range of the slow solar wind significantly differs from $\sim 45°$.

Despite these deficiencies, Eq. 3.37 was successfully used by a number of authors (e.g. Lallement et al. 1985a; Pryor et al. 1998, 2003) to qualitatively infer the solar wind structure. The conclusions were similar to those obtained from the IPS analysis: during solar minimum the solar wind is latitudinally structured, with a band of enhanced flux at the equator and two polar caps of a rarefied and fast wind. During solar maximum the ordered structure changes and the polar caps become almost fully covered with the slow wind.

However, it became clear that the simple model given by Eq. 3.37 is not fully adequate to describe reality and a need for more observations became evident. Bertaux et al. (1995) proposed an experiment to study solar wind anisotropies using the technique of analysis of the heliospheric Lyman-α backscatter glow, which was implemented in the French/Finnish project SWAN[9] onboard the Solar and Heliospheric Observatory mission (SOHO).

Already shortly after the launch of SOHO it became evident that the early conclusions on the evolution of the heliospheric groove, and thus the solar wind, with the solar activity cycle were confirmed (Bertaux et al. 1996, 1997, 1999; Kyrölä et al. 1998), but the formula used to describe the latitude profile of the ionization rate needed modification. Thus in the latter work, Eq. 3.37 was modified to describe separately the northern and southern hemispheres:

$$\beta_{\mathrm{CX}}(\phi) = \beta_0 \left[\Theta(\phi)\left(1 - A_N \sin^2\phi\right) + \Theta(-\phi)\left(1 - A_S \sin^2\phi\right) + B(\phi)\right], \quad (3.38)$$

where Θ is the Heavyside step function, A_N, A_S are the separate anisotropy parameters for the northern and southern hemispheres, and $B(\phi)$ is used to narrow the width of the equatorial band of enhanced solar wind flux. An even more sophisticated approach was proposed by Summanen (1996), who suggested to approximate the equatorial band in the latitudinal profile of the total ionization rate by:

$$\beta_{\mathrm{CX}}(\phi, t) = \beta_0 \left[1 - A(t) \sin^2(c\,\phi)\right] \quad (3.39)$$

for heliolatitudes $-40° \leq \phi \leq 40°$, where $c = 9/4$ limits the equatorial band to $\pm 40°$, and by:

$$\beta_{\mathrm{CX}}(\phi, t) = \beta_0 \exp\left[-\left(\frac{t - P/2}{0.2P}\right)^2\right] \quad (3.40)$$

outside the $\pm 40°$ equatorial band, where P is the solar cycle length and t, time. In this formula, there was no north-south asymmetry allowed, but it was possible to homogeneously reproduce the variations of the anisotropy parameters with the solar activity cycle.

The north-south anisotropies in the ionization rate and their evolution with solar activity were evident on one hand, and on the other hand the first fast latitude scan by Ulysses (Phillips et al. 1995a) suggested that the profile of solar wind parameters can be approximated by an equatorial plateau (with a "rough surface" of the gusty slow wind) standing out from a flat "foot" of the fast polar wind.

[9]For: Solar Wind ANisotropies.

Bzowski (2001a, 2003) and Bzowski et al. (2002) suggested to approximate it by the formula:

$$\begin{aligned}\beta_{\mathrm{CX}}(\phi,t) &= (\beta_{\mathrm{CX,pol}}+\delta_{CX}\,\phi)+(\beta_{\mathrm{CX,eqtr}}(t)-\beta_{\mathrm{CX,pol}}) \\ &\times \exp\left[-\ln 2\left(\frac{2\phi-\phi_N(t)-\phi_S(t)}{\phi_N(t)-\phi_S(t)}\right)^N\right],\end{aligned} \tag{3.41}$$

where ϕ is heliographic latitude and N is a shape factor; $\beta_{\mathrm{CX,pol}}$ is the average ionization rate at the poles and the term $(\beta_{\mathrm{CX,pol}}+\delta_{CX}\,\phi)$ describes the north-south asymmetry of the polar ionization rates. The term $(\beta_{\mathrm{SW,pol}}+\delta_{CX}\,\phi)+(\beta_{\mathrm{SW,eqtr}}(t)-\beta_{\mathrm{CX,pol}})$ for $\phi=0$ corresponds to the charge exchange rate at solar equator; and the term $\exp\left[-\ln 2\left(\frac{2\phi-\phi_N-\phi_S}{\phi_N-\phi_S}\right)^N\right]$ describes the latitudinal dependence of the ionization rate (see also Bzowski 2008). The shape of the central bulge is controlled by the exponent N; for $N=2$ the shape is Gaussian, for $N=8$ it is close to rectangular.

The parameters in the model by Bzowski (2003) are the north and south boundaries of the equatorial slow wind band ϕ_N and ϕ_S, the equator/north pole and equator/south pole ratios of the ionization rate, and the polar north/south asymmetry parameters. Thus, to obtain absolute values of the ionization rate, an independent assessment of the ionization rate at the equator is needed.

Bzowski et al. (2003) used the theory developed by Bzowski (2003) and interpreted a carefully selected subset of SWAN observations. To maintain in the data as much symmetry around the inflow axis as possible and simultaneously include the full span of heliolatitudes, they chose observations taken within a week of the passage of SWAN through the projection of inflow axis in the ecliptic plane, i.e. at the beginning of June and December of each year, and they restricted the field of view to a narrow strip going through the projections on the celestial sphere of the solar equator and poles.

They eliminated the "searchlights" (i.e., reflections on sky of the point-like active regions on the solar disk, traveling across the sky with the angular velocity of the solar rotation) discovered by Bertaux et al. (2000). They also cleaned the data from contamination by extraheliospheric "chaff" (Milky Way, stars etc.). To eliminate possible bias from an imperfect absolute calibration, they normalized the lightcurves to equatorial values of the helioglow intensity instead of attempting to fit the absolute values.

In agreement with other studies, Bzowski et al. (2003) found that the ordered structure of the solar wind, present during the solar minimum phase, disappears with the increasing solar activity. The boundaries between the fast and slow wind regions move polewards and ultimately at solar maximum the slow wind encompasses the entire space. The motion of the fast/slow wind boundaries in the north and south hemispheres were found to be shifted in phase by approximately a year.

Bzowski et al. (2008) discovered that the areas of the polar fast wind regions are linearly correlated with the areas of the polar holes observed by Harvey and Recely (2002), which enabled them to calculate the variation in the boundaries between the fast and slow solar wind ϕ_N, ϕ_S for the time span of the polar coronal holes observations, i.e. from 1990 until 2002. Bzowski et al. (2008) also suggested

that the evolution of ϕ_N, ϕ_S can be approximated by:

$$\phi_{N,S}(t) = \phi_0 + \phi_1 \exp\left[-\cos^3(\omega_\phi t)\right], \tag{3.42}$$

where ω_p was obtained as 2π/main period of the composite Lyman-α flux (cf Fig. 3.1) and the free parameters ϕ_0 and ϕ_1 are fit separately for the northern and southern hemispheres. The validity range of this approximation is limited to the time interval from 1990 to 2002. Based on this model of ionization, it was possible to infer the evolution of solar wind speed and density as a function of time and latitude. This topic is covered later in this chapter.

The model by Bzowski et al. (2003) and Bzowski et al. (2008) was able to more correctly reproduce the latitudinal span of the slow wind region and its evolution with solar activity, but was inadequate to correctly reproduce the boundaries themselves. Observations from SWAN showed that especially during the transition phases of solar activity, the photometric latitudinal profiles of the groove are complex and variable in time.

To address this problem, it turned out to be necessary to use an approach originally proposed by Summanen et al. (1993) and to model the ionization rate as a multi-step function, with different levels in fixed—though arbitrarily selected—latitudinal bands. Such an approach to the modeling of the ionization rate was numerically implemented already by Lallement et al. (1985a), but these authors filled the latitudinal "slots" with values obtained from the analytical models discussed earlier in this chapter.

In the refined approach, presented by Quémerais et al. (2006) and Lallement et al. (2010), the ionization rates in the latitudinal bands are free parameters fit to the maps of heliospheric backscatter glow, without any assumptions on the relations between the neighboring bands. In contrast to the approach exercised by Bzowski et al. (2003), Quémerais et al. (2006) and Lallement et al. (2010) used all the data available, cleaned only by appropriate masking to cut off the known extraheliospheric "chaff".

As a result, a time series of the ionization rate profiles at a resolution of $\sim 10°$ in heliolatitude and $\sim$ 2 days in time was obtained from fitting the model to the filtered full-sky maps and subsequent scaling to the in-ecliptic ionization rates obtained from in situ measurements. An illustration of results of this analysis is shown by Lallement et al. (2010). They support the general picture of the evolution of the solar wind structure with solar activity, but they point out that the width of the equatorial band of enhanced ionization rate was wider during the extended solar minimum in 2005 through 2009 than during the former minimum.

On the other hand, inspection of the heliolatitude vs time map of the ionization rate in Lallement et al. (2010) reveals some morphological features that are not supported by Ulysses or IPS observations. These discrepancies were one of the reasons to take a closer look at the calibration of the heliospheric FUV observations.

Historical Perspective: Ulysses Measurements

Ulysses, launched in October 1990, was the first spacecraft to traverse the polar regions of the heliosphere and provide a unique view of the solar wind (Wenzel et al. 1989; Smith et al. 1991). After a cruise to Jupiter, carried out close to the ecliptic

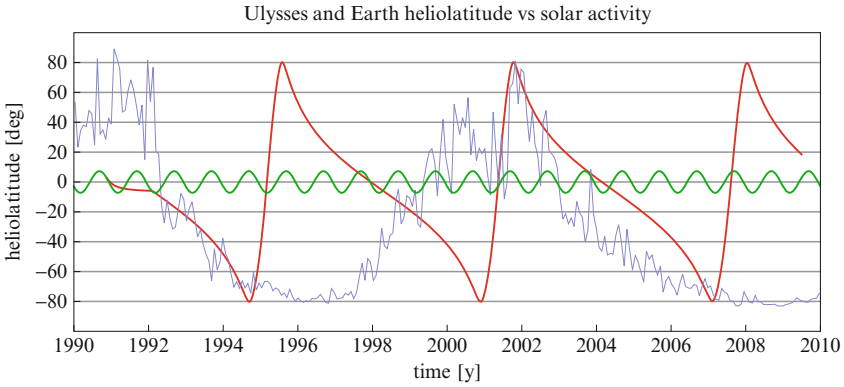

Figure 3.16: Illustration of the heliolatitude track of Ulysses (*red*) and the Earth (*green*) during the time span of Ulysses mission. The *pale blue line* is the $F_{10.7}$ solar radio flux, superimposed to correlate variations in solar activity with Ulysses heliolatitudes during its more than three orbits in a polar plane almost perpendicular to the inflow direction of neutral interstellar gas. Adapted from Sokół et al. (2012)

plane, it performed a Jupiter gravity-assist maneuver that cast it away from the ecliptic plane on an elliptical nearly polar orbit. The orbit has aphelion ~ 5.5 AU and perihelion ~ 1.4 AU and is nearly perpendicular both to the ecliptic plane and solar equator. It is also nearly perpendicular to the inflow direction of interstellar gas. The period of the orbit is about 6 years. The heliolatitude track of Ulysses is shown in Fig. 3.16.

The spacecraft was launched at solar maximum and its radial cruise was completed just when solar activity was beginning to decrease. The first dive towards the south solar pole was carried out during an interval of decreasing solar activity, followed by the first so-called fast latitude scan, when the spacecraft coasted from the south to the north solar pole, almost covering the full span of heliolatitudes during just about a year at solar minimum activity conditions.

This fast latitude scan preceded the first observations of the helioglow by SWAN by about a year. This provided an opportunity to calibrate the model of ionization rates obtained from the analysis of the heliospheric Lyman-α glow. Ulysses continued on its polar orbit, performing its first full slow latitude scan during an interval of increasing solar activity. The second fast latitude scan occurred in a totally different solar cycle phase, namely during solar maximum. This scan also took about a year and was performed during an interval of dynamically variable solar wind structure. In contrast to the first slow scan, the subsequent slow latitude scan occurred during decreasing solar activity. Afterwards, the spacecraft performed its last fast latitude scan, again during minimum solar activity.

The geometry and timing of Ulysses trajectory produced a unique dataset of direct in situ measurements of the solar wind plasma parameters, obtained from SWOOPS (Bame et al. 1992) and SWICS (Gloeckler et al. 1992) experiments. The

discoveries and findings from the plasma measurements were presented in dozens of papers (e.g. Phillips et al. 1995a,b; Marsden and Smith 1997, McComas et al. 1998a, McComas et al. 1999, 2000a,b, 2002a,b, 2003, 2006, 2008). An additional benefit from this unique mission is the use of the Ulysses flight spare plasma instrument with only minor modifications on the ACE mission (McComas et al. 1998a), which facilitates intercalibrating the Ulysses measurements with the OMNI time series.

The Ulysses solar wind dataset is unique and invaluable because it is the first and only direct in situ measurement of the solar wind parameters outside the ecliptic plane. The evolution of solar wind speed, adjusted density, and adjusted flux during the previous and current solar minima and during the previous maximum are compiled in Fig. 3.17, where the parameter values are averaged over 10-degree bins in heliolatitude. "Adjustment" throughout this text means scaling to 1 AU assuming an average dropoff with heliocentric distance as $1/r^2$.

It can be seen that the heliolatitude structure during the two minima is basically similar, featuring an equatorial enhancement in density with the associated reduction in velocity (the slow wind region), and that during solar maximum the slow wind expands to all heliolatitudes (see also Fig. 3.18 and discussion of time scales in the variation of the solar wind structure). However, the region of slow wind seems to reach farther in heliolatitude during the last solar minimum than during the minimum of 1995, which, interestingly, is much less conspicuous in density. Thus the findings from the Ulysses in situ measurements and SWAN remote-sensing observations by Lallement et al. (2010), discussed in the section "Historical Perspective: Insight from Heliospheric Backscatter Glow", qualitatively agree in this respect.

A striking feature seen in Fig. 3.17 is a strong reduction in flux with heliolatitude, reported by McComas et al. (2008) and Ebert et al. (2009). The reduction is visible as a continuous trend from the 1995 minimum through the 2002 maximum until present. Another interesting trend is a variation of $\sim 1\,\mathrm{km\,s^{-1}\,deg^{-1}}$ in the fast polar solar wind, discovered by McComas et al. (2000b) and expanded upon by Ebert et al. (2009).

Retrieval of Solar Wind Evolution: Introduction

In this section, we describe the history of our knowledge of the evolution of the solar wind density and speed during the past solar cycle. Our goal is to provide modelers a tool to develop a model of the neutral interstellar hydrogen distribution (see Izmodenov et al. 2012, this volume) that could be used as background for the inter-calibration of various sets of UV observations. This effort was recently described in a research paper by Sokół et al. (2012).

Sokół et al. (2012) attempted to use all relevant datasets, paying special attention to their absolute calibrations and possible biases. As shown later in this section, this is still a work in progress. Since an essential part of information must be drawn from a careful interpretation of the Lyman-α helioglow observations from SWAN, which are subject to improved absolute calibration, the effort of constructing a homogeneous set of solar wind parameters must be an iterative one.

In the following, we will present a construction of the procedure to retrieve the variability of solar wind speed and density in time and heliographic latitude using the available datasets, developed by Sokół et al. (2012). That construction

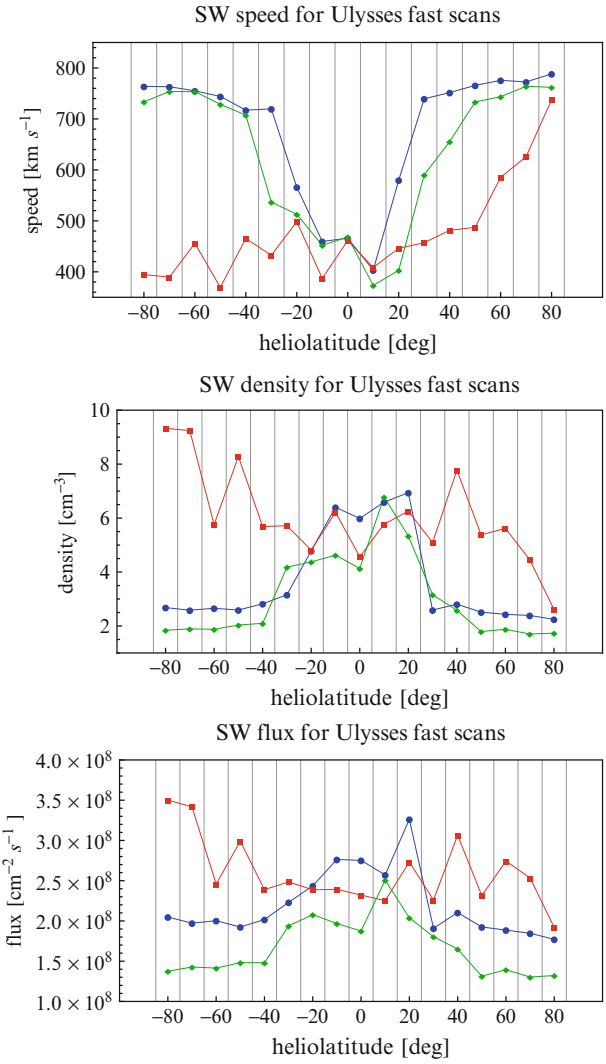

Figure 3.17: Solar wind speed (*upper panel*), adjusted density (*middle panel*), and adjusted flux (*lower panel*) as a function of heliolatitude for the first (*blue*), second (*red*) and third (*green*) Ulysses fast latitude scans, obtained from SWOOPS (Bame et al. 1992). The parameters are averaged over 10-degree heliolatitude bins. Adapted from Sokół et al. (2012)

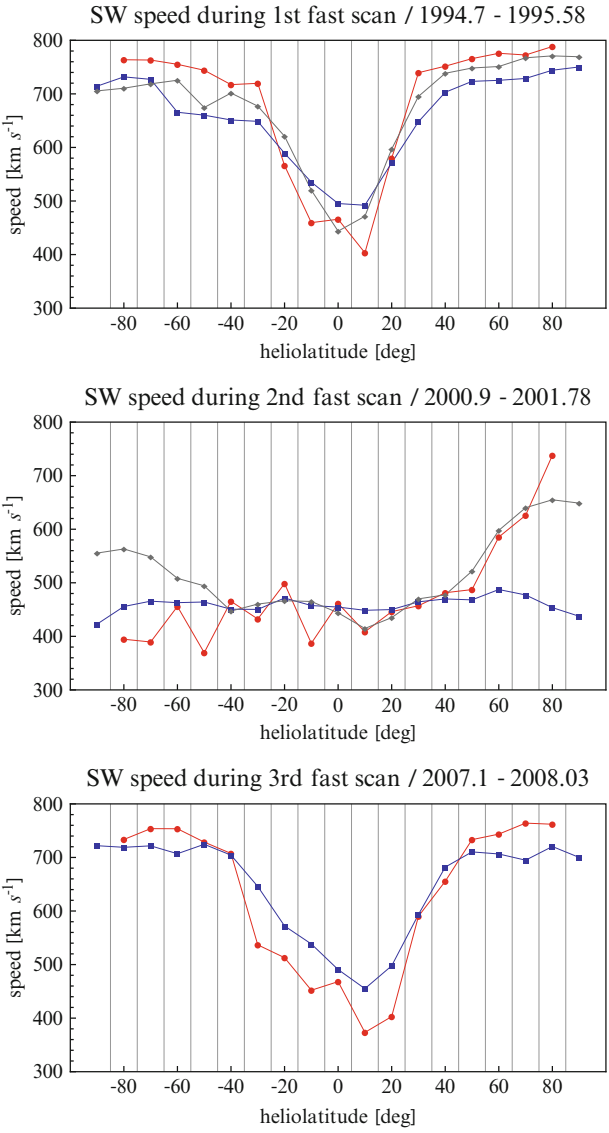

Figure 3.18: Solar wind speed profiles from Ulysses measurements and IPS observations for the three fast Ulysses scans. *Red*: Ulysses, *blue*: IPS during the year of beginning of a Ulysses fast scan, *gray*: IPS during the year of the end of Ulysses fast scan. *Top panel*: the first fast scan during solar minimum, *middle panel*: the second fast scan during solar maximum, *bottom panel*: the third fast scan during minimum. Adapted from Sokół et al. (2012)

relies on the absolute calibration of the OMNI dataset both in speed and density in the ecliptic plane. Out of ecliptic, the baseline is the absolute calibration of Ulysses SWOOPS measurements and IPS. The prime source of information on the heliolatitude structure of the solar wind are IPS observations, interpreted by tomography modeling, that generally agree quite well with the Ulysses SWOOPS in situ measurements out of the ecliptic and with the OMNI measurements in the ecliptic. Up to now, no continuous measurements of solar wind density as a function of ecliptic latitude have been available.

Tests revealed that an appropriate balance between the latitudinal resolution of the coverage and the fidelity of the results is obtained at a subdivision of the heliolatitudes' range into 10-degree bins. Concerning the time resolution, the most welcome would be Carrington rotation averages, identical with the resolution of the photoionization rate and Lyman-α flux. Regrettably, such a high resolution seems to be hard to achieve because (1) the time coverage in the data from IPS has gaps that typically occur during ~ 4 months at the beginning of each year, which would induce an artificial 1-year periodicity in the data, and (2) the fast latitude scans by Ulysses were about 12 months long, hence differentiating between time and latitude effects in its measurements is challenging. Thus a reliable latitude structure of the solar wind can only be obtained on a time scale of 1 year and this is the time resolution of the model that Sokół et al. (2012) developed.

Concerning the global mapping of solar wind parameters from the ecliptic, it has to be pointed out that the accuracy of measurements of solar wind parameters decreases with latitude because of geometry. The polar values are the most uncertain (and possibly biased) because the signal in the polar lines of sight is only partly formed in the polar region of space, which is illustrated in Fig. 3.19.

In the following section, we will present a procedure to retrieve the solar wind speed evolution in time and heliolatitude, plus two procedures for retrieval of solar wind density. One, by Sokół et al. (2012), is based on a correlation between the solar wind speed and density that was established from the three Ulysses fast latitude scans and must be regarded as an interim solution, to be used until the other one, based on the SWAN Lyman-α helioglow observations, will be available.

Latitude Profiles of Solar Wind Velocity from Interplanetary Scintillation Observations

IPS observations carried out by the Solar-Terrestrial Environment Laboratory (STEL) of Nagoya University (Japan) enable Sokół et al. (2012) to derive the latitude structure of solar wind speed and its variations in time. They used data from 1990 to 2011—with a one year gap in 2010—obtained from 3 antennas (Toyokawa, Fuji and Sugadaira) and from another antenna (Kiso) since 1994. The 4-antenna system was operated until 2005, when the Toyokawa antenna was closed (Tokumaru et al. 2010). Since then, the system has operated in a 3-antenna setup.

The IPS data from STEL are typically collected on a daily basis during 11 Carrington rotations per year: there is a break in winter because the antennas get covered with snow. The IPS observations are line of sight integration of the solar wind speed weighted by density turbulence and a Fresnel filter. Each day, 30–40 lines of sight for selected scintillating radio sources are observed.

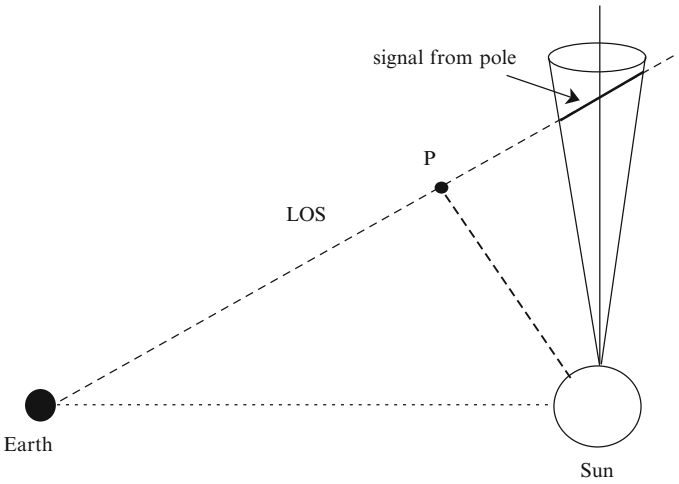

Figure 3.19: Illustration of the geometry of line of sight (LOS) in a remote sensing observation of the solar polar region. The observer is close to the Earth in the ecliptic plane and aims its instrument (e.g., a radio telescope antenna or a Lyman-α photometer) at a target so that the line of sight crosses a cone with a small opening angle centered at the pole. The signal is collected from the full length of the line of sight, but the contributions from various parts are different and depend on the observations technique. In the case of IPS observations, the strongest contribution to the signal is from the point nearest to the Sun along the line of sight, marked with P, because the source function of the scintillation signal decreases with the square of solar distance. In the case of helioglow observations, the maximum of the signal comes from the so-called Maximum Emissivity Region, which is located within 1.5–5 AU from the Sun, so it is important to carefully select the solar elongation of the line of sight. Note that the angular area of the polar region is quite small, so with an observations program that maps the entire sky only a small region in the maps indeed includes the signal from polar regions. Adapted from Sokół et al. (2012)

The line of sight integration effect is deconvolved using the Computer Assisted Tomography (CAT) method developed by the STEL group (Kojima et al. 1998, 2007). The LOS's are projected on the source surface at 2.5 solar radii ($R_\odot$), which is used as a reference surface in time sequence tomography.

The heliolatitude coverage by IPS observations is not uniform and is strongly correlated with the Sun's position in the sky, which changes during the year. The coverage is also constrained by the target distribution in the sky, with relatively few of them near the solar poles. Additionally, the observations of the south pole are of lower quality than those of the north pole because of the low elevation of the Sun during winter in Japan. The original latitude coverage was improved by adding the new antenna in 1994 and by optimization of the choice of the targets.

In the following, we briefly present the approach and results from Sokół et al. (2012). For the analysis, they took the solar wind speed from 1990 to 2011, without

year 2010, when the number of observations was not sufficient to retrieve reliable solar wind speeds. The solar wind speed observations were mapped at the source surface on a grid of $11 \times 360 \times 180$ records per year, which corresponds to a series of Carrington rotations. The data were organized in heliolatitude from 89.5° North to 89.5° South.

A comparison of the tomography-derived solar wind speed with the in situ measurements by Ulysses performed by Sokół et al. (2012) showed that the accuracy of the tomographic results depends on the number of IPS observations available for a given rotation. The intervals with a small number of data points clearly tend to underestimate the speed. Consequently, the Carrington rotations with the total number of points less than 30 000 were removed from the data. Small numbers of available observations typically happen at the beginning and at the end of the year and at the edges of data gaps. The selection of data by the total number of points per rotation constrained the coverage mainly to the summer and autumn months, when all latitudes are well sampled.

The selected subset of data was split into years, and within each yearly subset into 19 heliolatitude bins, equally spaced from $-90°$ to $90°$. The speeds averaged over bins and over year for the latitudinal bins yield the yearly latitudinal profiles of solar wind speed, shown in Figs. 3.20 and 3.21. They cover half of solar cycle 22 and the full solar cycle 23. In the analysis a two-step calculation was used.

First, Carrington rotation averaged values per bin were computed. Next, the yearly averages were calculated from the monthly ones. It is worth noting that the solar wind speed profiles for individual Carrington rotations during a given year typically have very similar shapes to the related yearly profile, which suggests that the latitude structure is stable during a year and changes only on a time scale comparable with solar activity variations.

The results confirm that the solar wind speed is bimodal during solar minimum, slow at latitudes close to the solar equator (and thus the ecliptic plane) and fast at the poles. The latitude structure evolves with the solar activity cycle and becomes flatter when the activity is increasing. The structure is approximately homogeneous in latitude only during a short time interval during the peak of solar maximum, when the solar wind is slow at all latitudes (see the panel for 2000 in Fig. 3.20). Shortly after the activity maximum, the bimodal structure reappears and the fast wind at the poles is observed again, but switchovers from the slow to fast wind at the poles may still occur during the high activity period, as shown in the panels for 2001 and 2003 in Figs. 3.20 and 3.21.

During the descending and ascending phases of solar activity there is a wide band of slow solar wind that straddles the equator and extends to midlatitudes; the fast wind is restricted to the polar caps and upper midlatitudes. At solar minimum, the structure is sharp and stable during a few years straddling the turn of solar cycles, with high speed at the poles and at midlatitudes and a rapid decrease at the equator.

Thus, apart from short time intervals at solar maximum, the solar wind structure close the poles is almost flat, with a steady fast speed value typical of wide polar coronal holes, in perfect agreement with the measurements from Ulysses (Phillips et al. 1995b; McComas et al. 2000b, 2006).

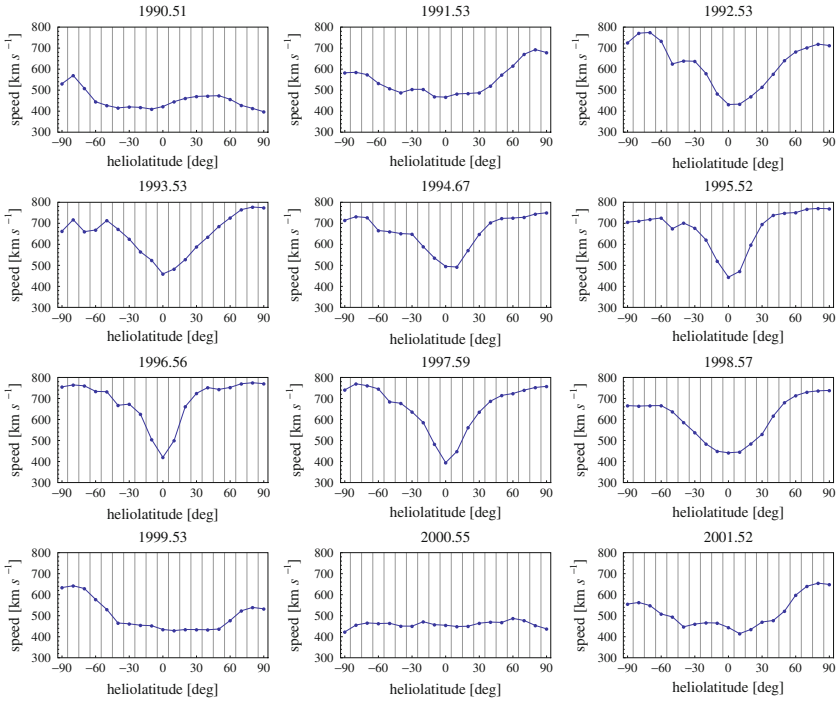

Figure 3.20: Heliolatitude profiles of yearly averaged solar wind speed for 1990–2001 obtained by Sokół et al. (2012) from the Computer Assisted Tomography analysis of interplanetary scintillation observations (Tokumaru et al. 2010). Adapted from Sokół et al. (2012)

To further verify the results obtained from the IPS analysis, we compared them with the data from the three Ulysses fast latitude scans and the OMNI measurements in the ecliptic plane. The Ulysses velocity profiles used for this comparison were constructed from subsets of hourly averages available from the NSSDC, split into identical heliolatitude bins as those used for the IPS data analysis and averaged. They are shown in Fig. 3.18 as red lines. Since the acquisition of the Ulysses profiles took one year each and the fast scans straddle the turn of the years, we show the IPS results for the years straddling the fast latitude scans. They are presented in blue and gray in Fig. 3.18.

The fast scans were performed at the perihelion half of the Ulysses elliptical orbit, with the perihelion close to the solar equator plane. Hence, the angular speed of its motion was highest close to the equator and traversing the 10-degree bin took it less than one solar rotation period. The apparent bin-to-bin fluctuation is an effect of incomplete Carrington longitude coverage of the bimodal solar wind, with slow wind interleaved with fast wind streams.

Near the poles, the angular speed was slower and it took more than 1 Carrington rotation to scan the 10-degree bin. Still, the longitudinal coverage was uneven.

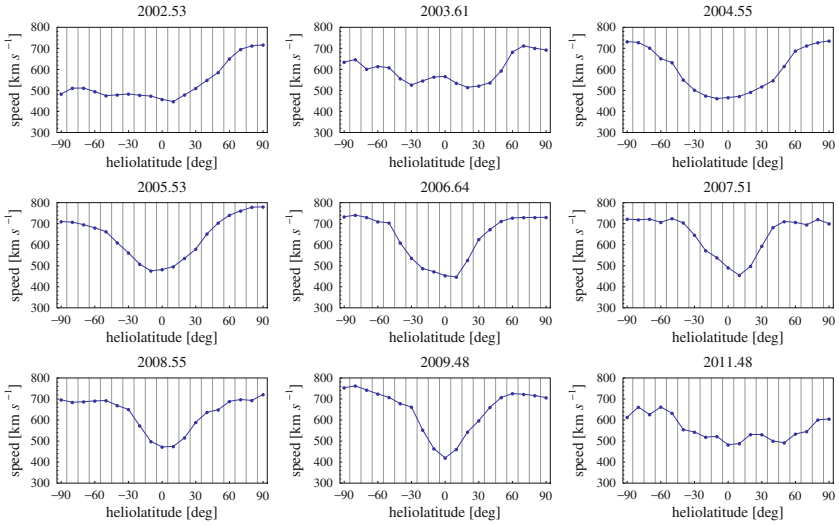

Figure 3.21: Heliolatitude profiles of yearly averaged solar wind speed for 2002–2011 obtained by Sokół et al. (2012) from the Computer Assisted Tomography analysis of interplanetary scintillation observations (Tokumaru et al. 2010). Note that data for 2010 are missing because of a non-sufficient number of observations available. Adapted from Sokół et al. (2012)

Thus, during solar maximum, when the gusty slow wind engulfed the whole space, the "sawtooth effect" expanded into the full latitude span. By contrast, during the low-activity scans the solar wind speed at high latitude was stable, which resulted in the lack of the small-scale latitude variations in the Carrington rotation averages at high latitudes, even though the issue of uneven longitudinal coverage persisted.

The solar wind speed profiles obtained from IPS and Ulysses observations are very similar, but some systematic differences do exist. On one hand, it seems that $\sim 50\,\mathrm{km\,s^{-1}}$ is a typical difference between Ulysses and IPS values in the polar regions, with the northern region usually in better agreement than the southern. On the other hand, sometimes the agreement is almost perfect.

The difference between the blue and gray lines in the top and middle panels of Fig. 3.18 is a measure of true variation of the latitudinal profile of solar wind speed during one year. Ulysses was moving from south to north during the fast latitude scans, so the south limb of the profile from Ulysses ought to be closer to the south limb of the blue profile obtained from the IPS analysis, while the north limb of the Ulysses profile should agree better with the north limb of the gray IPS profile.

Such behavior is observed in the second panel of Fig. 3.18, which corresponds to the solar maximum in 2001. In our opinion, it is a very interesting observation because (1) it shows how rapidly the latitude structure of the solar wind varies during solar maximum, and (2) it confirms both Ulysses and IPS results regarding solar wind structure.

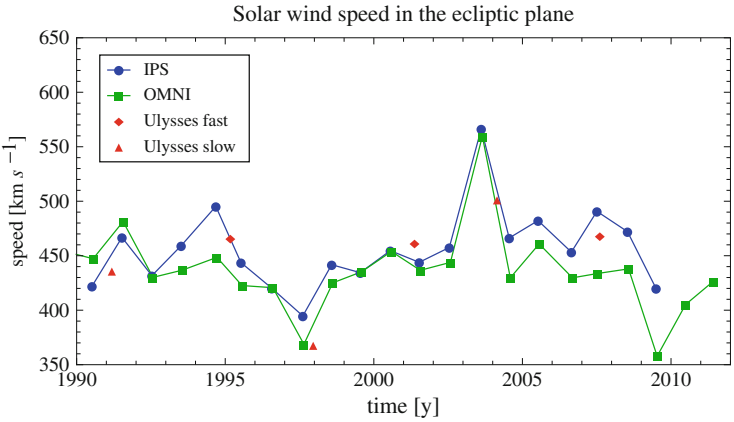

Figure 3.22: Yearly averages of solar wind speed from the IPS analysis (*blue*) and in-situ measurements collected in the OMNI-2 database (*green*), compared with the average solar wind speed measured by Ulysses during its passage within 5° from the solar equator plane during the three fast latitude scans (*red diamonds*) and three slow scans (*red triangles*). Adapted from Sokół et al. (2012)

Originally, the interpretation of the speed profiles obtained from Ulysses was not clear. It was pondered whether the north-hemisphere increase in the solar wind speed was a long-standing feature of the solar wind or was just due to a time-variability of the wind at the north pole. Similarly, it was pondered whether the IPS analysis is able to reliably reproduce the solar wind profiles given the fact that some of the profiles obtained approximately at the time of the fast scan seemed to disagree with the in situ data.

The analysis by Sokół et al. (2012) suggests that the yearly-averaged velocity profiles obtained from the tomography analysis of IPS observations agree with the in-situ observations from Ulysses even at times when the solar wind is restructuring rapidly at the peak of solar activity. The IPS data are in a very good agreement with the OMNI data collected in the ecliptic plane (see Fig. 3.22). Up to 2004, the agreement is almost perfect, afterwards small differences appear. The agreement is better than with the in-ecliptic Ulysses measurements from the fast latitude scans. This, in our opinion, is because the measurements of solar wind parameters in the ecliptic plane obtained during the fast latitude scans from Ulysses are challenging to directly compare with the OMNI and IPS measurements. The reason is that Ulysses was passing through the ecliptic 10-degree latitude bin in a time equal to about half of a Carrington rotation and thus a reliable longitude averaging of the solar wind parameters could not be obtained. A detailed discussion of the non-trivial issue of comparing the OMNI, Ulysses, and IPS solar wind speed close to the ecliptic plane is provided by Sokół et al. (2012).

The IPS solar wind speed profiles provide a solar wind latitude structure that can be adopted as an interim solution. They agree well both with the OMNI time series in the ecliptic and with the Ulysses measurements out of the ecliptic for the time intervals when they can be directly compared.

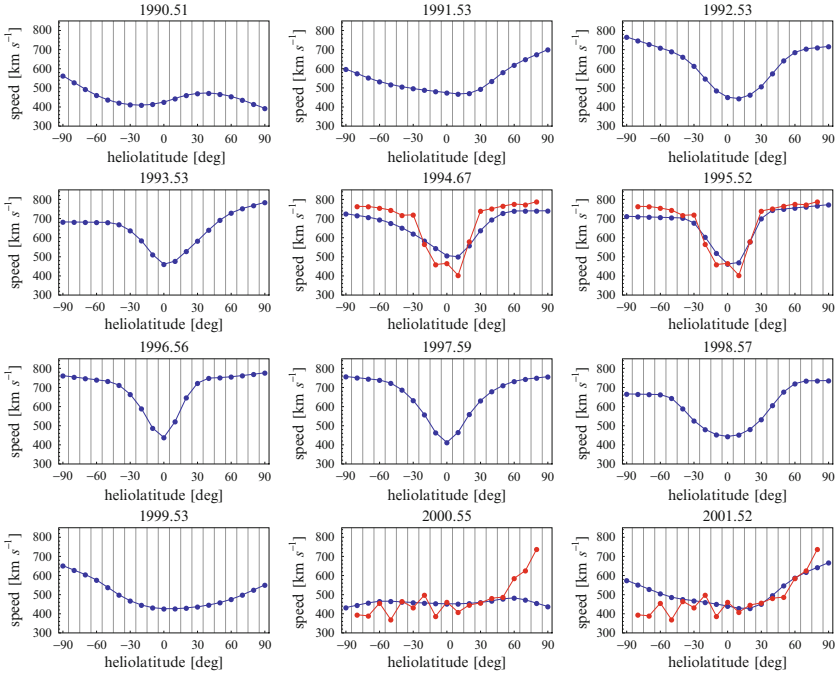

Figure 3.23: Latitude profiles of yearly-averaged solar wind speed for 1990–2001 obtained from the interim procedure described in the text. The *red lines* show the speed profiles obtained from the Ulysses fast scans. The profile for 2010 is a linear interpolation between the profiles for 2009 and 2011 (Sokół et al. 2012)

For further analysis, Sokół et al. (2012) smoothed the yearly speed profiles assuming that the variation of the solar wind speed at high latitude close to the poles is linear and the variation outside the polar caps can be approximated by a series of smoothly-transitioning parabolae. The resulting smoothed yearly heliolatitude profiles of solar wind speeds are shown in Figs. 3.23 and 3.24. The gap in the observations in 2010 was filled by linear interpolation between the profiles from 2009 and 2011. The formula used to smooth the profiles along with the numerical values of their parameters are listed in Sokół et al. (2012). These smoothed profiles will be used in the remainder of this paper to obtain the solar wind density and flux profiles.

Latitude Structure of Solar Wind Density and Flux

The time- and latitude-dependence of the solar wind flux and density can be obtained using two different methods. The first one (Sokół et al. 2012), which we regard as an interim solution, relies on an approximate correlation between the solar wind speed and density inferred from from fast latitude scan data taken by Ulysses. The other, expected to be the ultimate one, will be based on future analysis of the SWAN Lyman-α helioglow measurements, once completed. Here we will only introduce the first method.

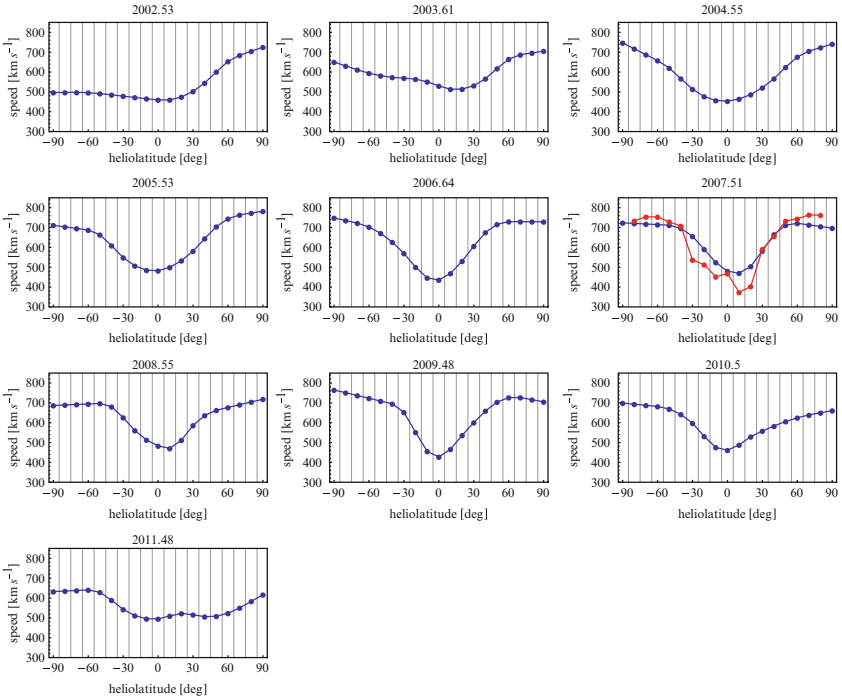

Figure 3.24: Latitude profiles of yearly-averaged solar wind speed for 2002–2011 obtained from the interim procedure described in the text. The *red lines* show the speed profiles obtained from the Ulysses fast scans. The profile for 2010 is a linear interpolation between the profiles for 2009 and 2011 (Sokół et al. 2012)

Solar Wind Density and Flux from Density-Speed Correlation

As discussed by Sokół et al. (2012), the solar wind speed and density seem to be related to heliolatitude and thus correlated with each other, at least during the solar minimum conditions and for the observations collected during the fast latitude scans. The correlations seem to be slightly different between the first and third latitude scans, as illustrated in Fig. 3.25:

$$n_{\mathrm{Ulysses}}\,(v) = a_{\mathrm{scan}} + b_{\mathrm{scan}}\,v, \tag{3.43}$$

where a_{scan} and b_{scan} are fit separately for the speed and density values averaged over 10-degree bins using the ordinary least squares bisector method (Isobe et al. 1990) which allows for uncertainty in both ordinate and abscissa. The fitting is done separately for the first and third latitude scans. For the first scan (blue line and points in Fig. 3.25) we obtain $a_{\mathrm{first}} = 12.69$ and $b_{\mathrm{first}} = -0.01332$. For the third scan (green line and dots in Fig. 3.25), the correlation formula parameters are $a_{\mathrm{third}} = 10.01$ and $b_{\mathrm{third}} = -0.01107$. Thus, the slopes are almost identical and the main difference between the two relations is in the y-intercept, which reflects the overall secular decrease in solar wind density.

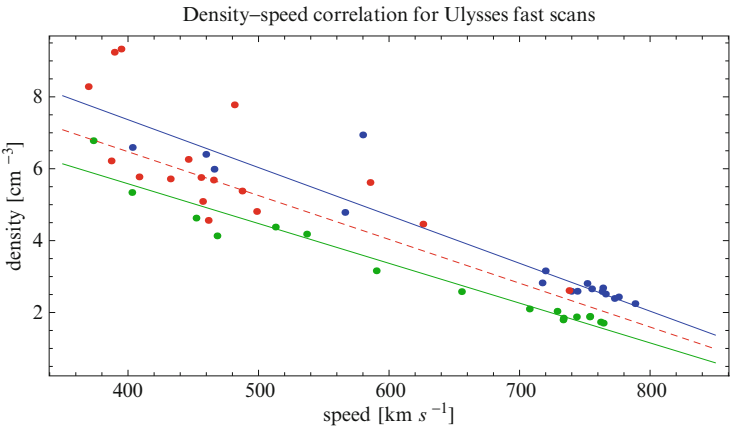

Figure 3.25: Anticorrelation between the solar wind density and speed obtained from Ulysses fast latitude scans. *Blue* corresponds to the first scan at solar minimum (see Fig. 3.16), *red* to the second scan (performed during solar maximum conditions), and *green* to the third scan excecuted during solar minimum. The *dots* represent speeds and densities averaged over the 10-degree heliolatitude bins, the *blue* and *green* lines are the linear correlations specified in Eq. 3.43. The *dotted red line* is the density—speed relation proposed for the transition interval close to the solar maximum of 2002, calculated as the mean of the correlation relations obtained from the first and third latitude scans. Adapted from Sokół et al. (2012)

The relation between density and speed for the second scan, which occurred during solar maximum, does not seem to be linear, but in this case the spatial and temporal effects seem to be convolved (as discussed earlier in this section). Therefore, Sokół et al. (2012) proposed to use an arithmetic mean of the relations for the first and third scans: $a_{\mathrm{second}} = (a_{\mathrm{first}} + a_{\mathrm{third}})/2$ and $b_{\mathrm{second}} = (b_{\mathrm{first}} + b_{\mathrm{third}})/2$. This relation is shown in Fig. 3.25 as the red broken line. A comparison of the density values actually measured during the second latitude scan and calculated from the correlation formula is shown in Fig. 3.26.

The interval of applicability of the latter formula is from ∼1998 until 2002. The formula from the first scan is applicable to the interval before 1998 and the formula from the third scan for the interval after 2002.

Sokół et al. (2012) calculated the interim yearly profiles of solar wind density as a function of heliolatitude by applying Eq. 3.43 to the speed profiles presented in the preceding subsection. Since this is an interim and very approximate solution, which by its nature is not very accurate, the authors did not attempt to further adjust it at the equator to the corresponding OMNI densities. The results are shown in Figs. 3.27 and 3.28. The accuracy of the results in the polar regions is in the range of 20–40 %.

With the density and speed profiles on hand, one can easily calculate the flux:

$$F(\phi_j, t_i) = v(\phi_j, t_i)\, n(\phi_j, t_i)\,, \tag{3.44}$$

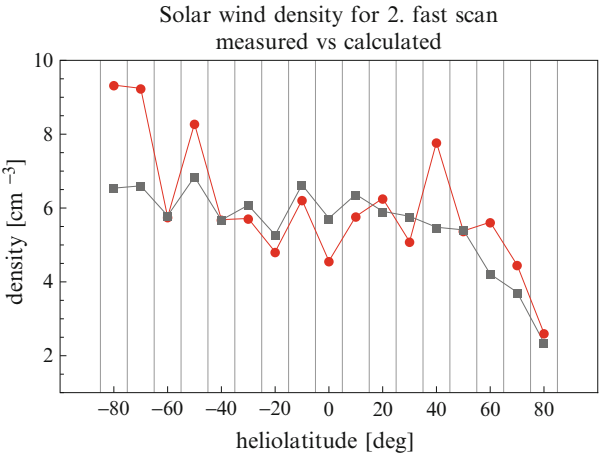

Figure 3.26: Comparison of solar wind density averaged over 10-degree heliolatitude bins actually measured by Ulysses (*red*) and calculated from the correlation formula in Eq. 3.43 (*blue*) (Sokol et al., Solar Physics, 2012)

dynamic pressure:

$$p_{dyn}\left(\phi_j, t_i\right) = \frac{1}{2} m_p n\left(\phi_j, t_i\right)\left(v\left(\phi_j, t_i\right)\right)^2, \tag{3.45}$$

and charge exchange rate (in the stationary H atom approximation; Eq. 3.14). They are collectively shown in Fig. 3.29.

To obtain the solar wind parameters (speed, density, flux, dynamic pressure, charge exchange rate and total ionization rate) at monthly resolution, Sokół et al. (2012) replaced the equatorial bin directly with the Carrington rotation averaged series from OMNI, linearly interpolated to halves of Carrington rotations. The $\pm 10^\circ$ bins were replaced with values linearly interpolated between the ± 20 deg bins and the equatorial bin.

The pole values were calculated from the the parabolic interpolation between the ± 70 and $\pm 80^\circ$ bins, because due to the problems discussed earlier in this chapter direct measurements over the poles are not available. The remaining latitudinal bins were linearly interpolated in time between the yearly profiles. As a result of such a treatment, all available information on the equatorial bin of the solar wind was utilized. Away from the equatorial bin, where such an information is not available, there is a smooth transition into the latitude region where the low time-resolution model is used.

Figure 3.29 shows contour maps of solar wind flux (upper), charge exchange rate (middle), and dynamic pressure (lower) as a function of time (horizontal axis) and heliolatitude (vertical axis). The magnitude of the quantity being shown is indicated by color code and isocontours.

The latitudinal profile of a given quantity at a desired moment in time can be retrieved by taking a vertical strip of the map from a location corresponding to the

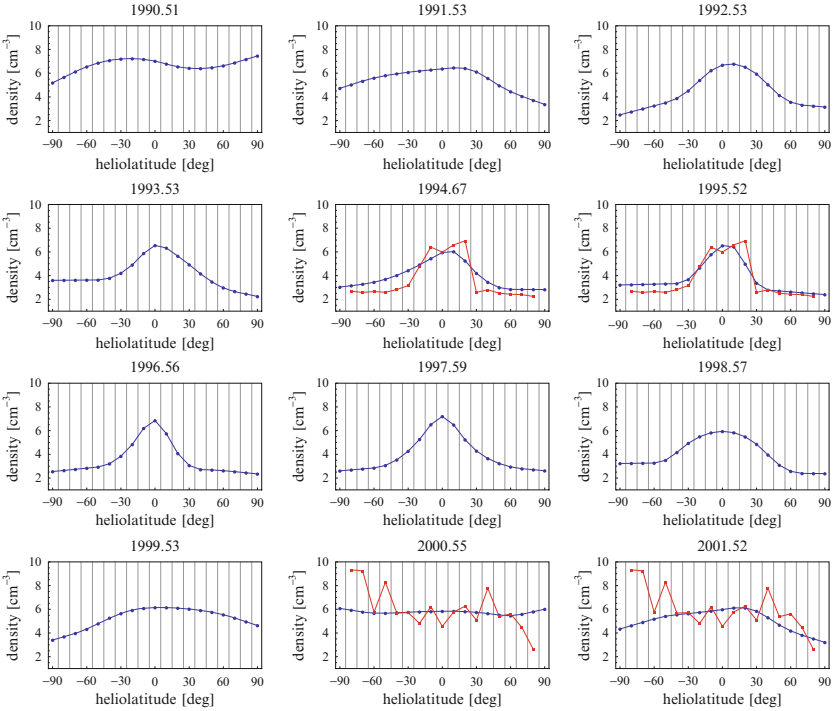

Figure 3.27: Latitude profiles of yearly averaged solar wind density for 1990–2001 obtained from the interim procedure. The *red lines* show the Ulysses fast scan profiles (Sokół et al. 2012)

desired time on the horizontal axis. The evolution of a given quantity in time at a selected heliolatitude can be retrieved taking a horizontal strip for the latitude indicated at the vertical axis. The magnitude of this quantity is color-coded and the color code is given in the color bar next to the panels. The isocontours indicate regions in (time vs heliolatitude) space where the quantity has a specific value.

As discussed by Sokół et al. (2012), the structure of solar wind flux and charge exchange painted in Fig. 3.29 shows a clear variation with solar activity level. During the epochs of two solar minima presented in the figure, the flux and charge exchange rate were almost spherically symmetric, as indicated by the light bands spanning the whole latitude range in 1991 and in 2001.

By contrast, the flux and charge exchange structure during prolonged intervals of lower activity is quite different. The flux and charge exchange rate feature clear maxima at the equatorial latitude. One can observe some north-south asymmetry in the latitudinal range of this equatorial enhancement, as well as a small (< 1 year) shift in phase between the northern and southern hemispheres.

The absolute magnitude of the flux and charge exchange rate dropped after the solar maximum of activity in 2001, which can be seen as a general dimming of the maps in their right-hand halves. This weakening exists at all heliolatitudes.

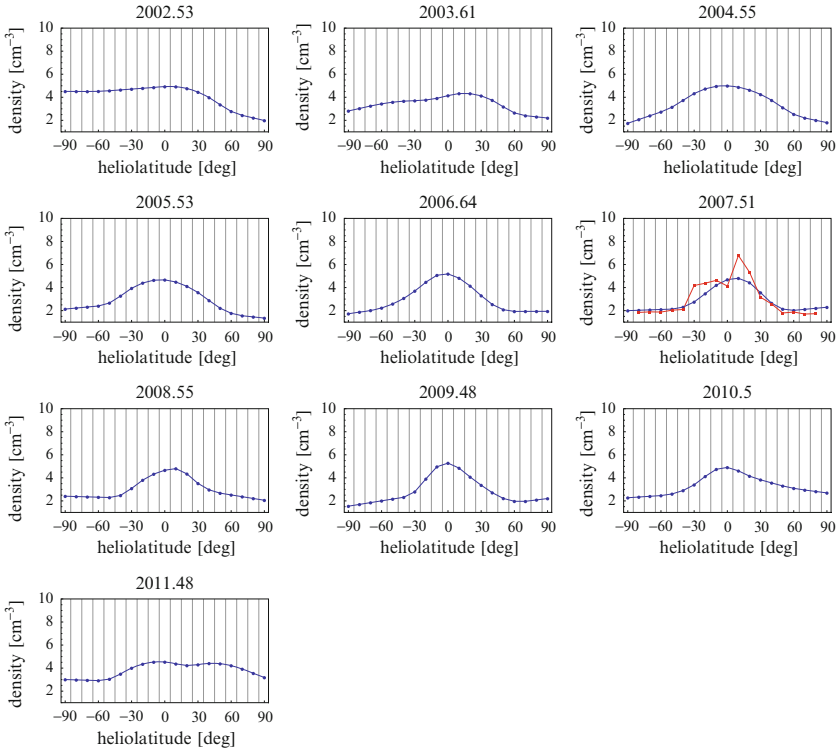

Figure 3.28: Latitude profiles of yearly averaged solar wind density for 2002–2011 obtained from the interim procedure. The *red lines* show the Ulysses fast scan profiles (Sokół et al. 2012)

Interestingly, the behavior of the solar wind ram pressure is different. This quantity is much less structured in heliolatitude than radiation pressure and charge exchange are. This is true at all times, practically regardless of the solar activity level. The solar wind ram pressure also weakened, similarl to the flux and charge exchange rate. However, the drop in pressure began earlier than the drop in the other quantities, namely just before the last solar maximum, i.e., about 1998.

Summing up this section, we have the structure of the solar wind speed from the smoothed IPS profiles (Figs. 3.23 and 3.24). The density structure is obtained (Figs. 3.27 and 3.28) from the density-speed correlation from Ulysses (Eq. 3.43, Fig. 3.25). From these, one calculates the solar wind flux, dynamic pressure, and—from Eq. 3.19—charge exchange rate between solar wind protons and neutral H atoms (Fig. 3.29).

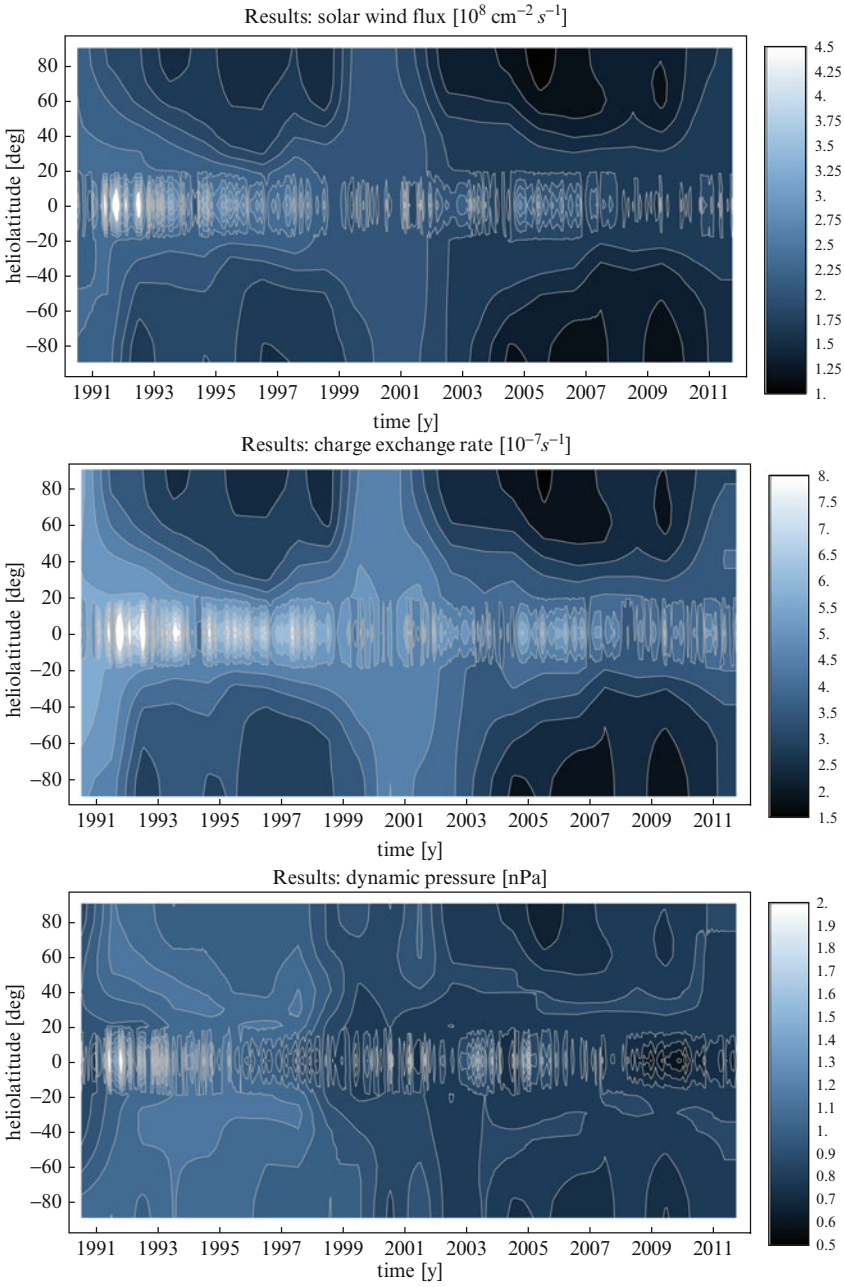

Figure 3.29: Contour maps of solar wind flux (in $10^8\,\mathrm{cm}^{-2}\,s^{-1}$), charge exchange (in $10^{-7}\,\mathrm{s}^{-1}$) and dynamic pressure (in nPa) shown as a function of time (*horizontal axis*) and heliolatitude (*vertical axis*). The magnitudes are color-coded, with the color code shown in the color bars accompanying the panels (Sokół et al. 2012)

Outlook: Latitudinal Structure of Solar Wind Flux and Density from IPS and Lyman-α Helioglow Observations *(A Sketch of the Method)*

In this section we propose a method to obtain the solar wind density as a function of heliolatitude by combining information from IPS measurements and from analysis of photometric observations of the Lyman-α backscatter glow from SWAN. We assume that the total ionization rate from SWAN is the sum of the charge exchange and photoionization rates of H, with electron impact ionization neglected (because $\beta_{\mathrm{el}} \ll \beta_{\mathrm{CX}}$ for the maximum emissivity region (MER) distance and beyond). Thus the heliolatitude- and time-dependent charge exchange rate can be calculated as

$$\beta_{\mathrm{CX}}\left(\phi_j, t_i\right) = \beta_{\mathrm{tot}}\left(\phi_j, t_i\right) - \beta_{\mathrm{Hph}}\left(0, t_i\right), \tag{3.46}$$

where $\beta_{\mathrm{tot}}\left(\phi_j, t_i\right)$ is obtained from the inversion of a SWAN map and the photoionization rate $\beta_{\mathrm{Hph}}\left(0, t_i\right)$, here assumed to be spherically symmetric, is from one of the formulae specified in Eqs. 3.23, 3.24, or 3.25.

Since the total ionization rate data from SWAN for the equator does not always agree with the rate derived from direct in situ measurements, we calculate the contrasts $\kappa_{\beta,\mathrm{SWAN}}\left(\phi_j, t_i\right)$ of the SWAN-derived ionization rates as a function of heliolatitude using:

$$\kappa_{\beta,\mathrm{SWAN}}\left(\phi_j, t_i\right) = \frac{\beta_{\mathrm{SWAN}}\left(\phi_j, t_i\right)}{\beta_{\mathrm{SWAN}}\left(0, t_i\right)}, \tag{3.47}$$

where $\beta_{\mathrm{SWAN}}\left(\phi_j, t_i\right)$ is an ionization rate at ϕ_jth heliolatitude and $\beta_{\mathrm{SWAN}}\left(0, t_i\right)$ is an ionization rate at the equator. In this way we can build yearly contrasts for the 19 heliolatitude bins and for the years since 1996. Multiplying the contrasts $\kappa_{\beta,\mathrm{SWAN}}\left(\phi_j, t_i\right)$ with the monthly averages of the total equatorial ionization rates (see Fig. 3.7), we obtain latitudinal profiles of the total ionization rate that agree with the baseline values for the equator.

We can calculate the absolute charge exchange ionization rate for all heliolatitudes by subtracting the photoionization rate from the total rate from Eq. 3.46. Considering the formula for charge exchange rate given in Eq. 3.14, with the solar wind velocity profile obtained from IPS observations $v\left(\phi_j, t_i\right)$ we can now calculate the total solar wind flux as a function of heliolatitude in the following way:

$$F\left(\phi_j, t_i\right) = \beta_{\mathrm{CX}}\left(\phi_j, t_i\right) / \sigma_{\mathrm{CX}}\left(v\left(\phi_j, t_i\right)\right). \tag{3.48}$$

With the flux and solar wind speed profile on hand, it is straightforward to calculate the profile of density:

$$n\left(\phi_j, t_i\right) = F\left(\phi_j, t_i\right) / v\left(\phi_j, t_i\right). \tag{3.49}$$

In that way we can obtain a model of the evolution of the solar wind speed and density as a function of time and heliolatitude. This model can be used to calculate the evolution of the ionization rate for H atoms traveling at arbitrary speeds and can be used as an input to global models of the heliosphere to calculate the flux and dynamic pressure of the solar wind. This calculation will be performed once

the intercalibration of the heliospheric EUV measurements has been completed and the final inversion of the SWAN photometric observations for the ionization rate profiles is performed.

It is worthwhile to mention here that the proposed method involves a time-latency because the inflowing hydrogen gas needs some time to adapt its density distribution to the changing ionization rate and radiation pressure. This effect was discussed by Bzowski et al. (2002), who showed that the latency is a function of the offset angle of the line of sight from the upwind direction. Its magnitude depends on the velocity and temperature of the gas, but it is almost constant on a level between 0.5 and 1.1 years for the offset angles between 0° and 90°. For higher offset angles, between 90° and 140°, it increases by a factor of 1.5–2. This suggests that a time dependent model of the distribution of neutral interstellar hydrogen in the inner heliosphere should be used for modeling.

Summary

Intercalibration of heliospheric UV and EUV measurements requires a common basis of heliospheric ionization processes. The ionization processes affect the distribution of neutral interstellar gas in the heliosphere and thus influence both the spectrum and intensity distribution of the heliospheric backscatter glow.

In this chapter we presented a review of the solar factors affecting the distribution of neutral interstellar gas in the heliosphere. We discussed the radiation pressure, solar EUV ionizing radiation, and the solar wind parameters. We reviewed the history of measurements of these factors and developed a model of time and heliolatitude evolution of solar wind speed and density based on data available from in situ measurements of the solar wind parameters, from remote sensing interplanetary scintillation observations of the solar wind speed structure, and from correlation between the solar wind density and speed, inferred from in situ measurements.

The results of this model are used as input in the global heliospheric models, discussed by Izmodenov et al. (2012, this volume). The results of the global heliospheric modeling can in turn be used to fine tune the absolute calibration of heliospheric EUV measurements and, in a new iteration, to further refine the solar wind evolution model.

The refined model will cover at least the two recent solar cycles and will thus provide a common homogeneous basis for interpretation of the present and past heliospheric experiments. It will also be used to interpret the observations of Energetic Neutral Atoms by the Interstellar Boundary Explorer (IBEX) (McComas et al. 2009a,b) and hopefully other past and future heliospheric measurements.

Acknowledgements

M.B. and J.S. are obliged to Marty Snow for sharing his insight into the realm of EUV measurements. The authors acknowledge the use of NASA/GSFC's Space Physics Data Facility's ftp service for Ulysses/SWOOPS and TIMED/SEE data, SOHO/CELIAS/SEM (http://www.usc.edu/dept/space_science/semdatafolder/long/daily_avg/), and OMNI2 data collection (ftp://nssdcftp.gsfc.nasa.gov/spacecraft_data/omni/). The $F_{10.7}$ solar radio flux

was provided by the NOAA and Pentincton Solar Radio Monitoring Programme operated jointly by the National Research Council and the Canadian Space Agency (ftp://ftp.ngdc.noaa.gov/STP/SOLAR_DATA/SOLAR_RADIO/FLUX/Penticton_Adjusted/ and ftp://ftp.geolab.nrcan.gc.ca/data/solar_flux/daily_flux_values/). The composite Lyman-α flux and $\mathrm{MgII_{c/w}}$ were obtained from LASP, accessed through the LISIRD Web page at (http://lasp.colorado.edu/lisird/lya/). The SOLAR2000 Research Grade historical irradiances are provided courtesy of W. Kent Tobiska and SpaceWx.com. These historical irradiances have been developed with funding from the NASA UARS, TIMED, and SOHO missions.

M.B. and J.S. were supported by the Polish Ministry for Science and Higher Education grants NS-1260-11-09 and N-N203-513-038. P.B. acknowledges support from NASA SR&T Grant NX09AW32G. Contributions from D.M. were supported by NASA's IBEX Explorer mission. Support from the International Space Science Institute in Bern, Switzerland, is gratefully acknowledged.

Bibliography

P.O. Amblard, S. Moussaoui, T. Dudok de Wit, J. Aboudarham, M. Kretzschmar, J. Lilensten, F. Auchère, The euv sun as the superposition of elementary suns. Astron. Astrophys. **487**, L13–L16 (2008). doi:10.1051/0004-6361:200809588

G. Artzner, J.C. Vial, P. Lemaire, P. Gouttebroze, J. Leibacher, Simultaneous time-resolved observations of the H L-alpha Mg K 2795 A, and Ca K solar lines. Astrophys. J. Lett. **224**, L83–L85 (1978). doi:10.1086/182765

K. Asai, M. Kojima, M. Tokumaru, A. Yokobe, B.V. Jackson, P.L. Hick, P.K. Manoharan, Heliospheric tomography using interplanetary scintillation observations. iii - correlation between speed and electron density fluctuations in the solar wind. J. Geophys. Res. **103**, 1991–2001 (1998). doi:10.1029/97JA02750

J.R. Asbridge, S.J. Bame, W.C. Feldman, M.D. Montgomery, Helium and hydrogen velocity differences in the solar wind. J. Geophys. Res. **81**, 2719–2727 (1976). doi:10.1029/JA08li016p02719

F. Auchère, Effect of the H I Ly α chromospheric flux anisotropy on the total intensity of the resonantly scattered coronal radiation. Astrophys. J. **622**, 737–743 (2005). doi:10.1086/427903

F. Auchère, J.W. Cook, J.S. Newmark, D.R. McMullin, R. von Steiger, M. Witte, Model of the all-sky He II 30.4 nm solar flux. Adv. Space Res. **35**, 388–392 (2005a). doi:10.1016/j.asr.2005.02.036

F. Auchère, D.R. McMullin, J.W. Cook et al., A model for solar euv flux helium photoionization throughout the 3-dimensional heliosphere, in *Proceedings of the Solar Wind 11 / SOHO 16 "Connecting the Sun and Heliosphere" Conference*, Whistler, Canada, June 2005. S.P. ESA-592, ed. by B. Fleck, T.H. Zurbuchen, H. Lacoste (2005b), pp. 327–329

S.J. Bame, E.W. Hones Jr., S.-L. Akasofu, M.D. Montgomery, J.R. Asbridge, Geomagnetic storm particles in the high-latitude magnetotail. J. Geophys. Res. **76**, 7566–7583 (1971). doi: 10.1029/JA076i031p07566

S.J. Bame, J.R. Asbridge, H.E. Felthauser, J.P. Glore, H.L. Hawk, J. Chavez, ISEE-C solar wind plasma experiment. IEEE Trans. Geosci. Electron. **16**, 160–162 (1978a)

S.J. Bame, J.R. Asbridge, H.E. Felthauser, J.P. Glore, G. Paschmann, P. Hemmerich, K. Lehmann, H. Rosenbauer, ISEE-1 and ISEE-2 fast plasma experiment and the ISEE-1 solar wind experiment. IEEE Trans. Geosci. Electron. **16**, 216–220 (1978b)

S.J. Bame, D.J. McComas, B.L. Barraclough, J.L. Phillips, K.J. Sofaly, J.C. Chavez, B.E. Goldstein, R.K. Sakurai, The Ulysses solar wind plasma experiment. Astron. Astrophys. Supp. **92**, 237–265 (1992)

V.B. Baranov, Kinetic and hydrodynamic approaches in space plasma, in *The Physics of the Heliospheric Boundaries*, ed. by V.V. Ismodenov, R. Kallenbach, Vol. SR-005 of ISSI Science Report, pp. 1–26, ESA Publications Division, EXTEC ISBN 1608-280X (2006a)

V.B. Baranov, Early concepts of the heliospheric interface: plasma, in *The Physics of the Heliospheric Boundaries*, ed. by V.V. Ismodenov, R. Kallenbach, vol. SR-005 of ISSI Science Report, pp. 27–44 (2006b)

V.B. Baranov, Y.G. Malama, Model of the solar wind interaction with the local interstellar medium—numerical solution of self-consistent problem. J. Geophys. Res. **98**, 15157–15163 (1993). doi:10.1029/93JA01171

V.B. Baranov, M.G. Lebedev, Y.G. Malama, The influence of the interface between the heliosphere and local interstellar medium on the penetration of H atoms to the solar system. Astrophys. J. **375**, 347–351 (1991). doi:10.1086/170194

C.F. Barnett, H.T. Hunter, M.I. Kirkpatrick, I. Alvarez, C. Cisneros, R.A. Phaneuf, Atomic data for fusion, in *Volume 1: Collisions of H, H_2, He, and Li Atoms and Ions with Atoms and Moleucles*. vol. ORNL-6086/V1 (Oak Ridge National Laboratories, Oak Ridge, Tennessee, 1990)

J.-L. Bertaux, J.E. Blamont, Evidence for a source of an extraterrestrial hydrogen Lyman alpha emission. Astron. Astrophys. **11**, 200–217 (1971)

J.-L. Bertaux, E. Kyrölä, E. Quémerais, R. Pellinen, R. Lallement, W. Schmidt, M. Berthé, E. Dimarellis, J.P. Goutail, C. Taulemasse, C. Bernard, G. Leppelmeier, T. Summanen, H. Hannula, H. Huomo, V. Kehlä, S. Korpela, K. Leppälä, E. Strömmer, J. Torsti, K. Viherkanto, J.-F. Hochedez, G. Chretiennot, R. Peyroux, T. Holzer, SWAN: a study of solar wind anisotropies on SOHO with Lyman alpha sky mapping. Sol. Phys. **162**, 403–439 (1995). doi:10.1007/BF00733435

J.-L. Bertaux, E. Quémerais, R. Lallement, Observations of a sky Lyman α groove related to enhanced solar wind mass flux in the neutral sheet. Geophys. Res. Lett. **23**, 3675–3678 (1996). doi:10.1029/96GL03475

J.-L. Bertaux, E. Quémerais, R. Lallement, E. Kyrölä, W. Schmidt, T. Summanen, T. Mäkinen, The first 1.5 years of observation from SWAN Lyman-alpha solar wind mapper on SOHO, in *Fifth SOHO Workshop: The Corona and Solar Wind near Minimum Activity*, Oslo, Norway, June 1997, ed. by A. Wilson. S.P. ESA-404, p. 29 (1997)

J.-L. Bertaux, E. Kyrölä, E. Quémerais, R. Lallement, W. Schmidt, J. Costa, T. Mäkinen, SWAN observations of the solar wind latitude distribution and its evolution since launch. Space Sci. Rev. **87**, 129–132 (1999). doi:10.1023/A:1005178402842

J.-L. Bertaux, E. Quémerais, R. Lallement, E. Lamassoure, W. Schmidt, E. Kyrölä, Monitoring solar activity on the far side of the sun from sky reflected Lyman α radiation. Geophys. Res. Lett. **27**, 1331–1334 (2000). doi:10.1029/1999GL003722

S. Błeszyński, S. Grzędzielski, D. Ruciński, J. Jakimiec, Expected fluxes of about 1 keV neutral H atoms in interplanetary space—comparison with the uv background and possibility of detection. Planet. Space Sci. **40**, 1525–1533 (1992). doi:10.1016/0032-0633(92)90049-T

P. Bochsler, M. Bzowski, L. Didkovsky, H. Kucharek, J.M. Sokół, T.N. Woods, Ionization rates (preliminary), (2012) in preparation

A. Bonetti, G. Moreno, S. Cantarano, A. Egidi, R. Marconero, F. Palutan, G. Pizella, Solar wind observations with satellite ESRO HEOS-1 in December 1969. Nuovo Cimento B Series **46**, 307–323 (1969). doi:10.1007/BF02711013

R.M. Bonnet, P. Lemaire, J.C. Vial, G. Artzner, P. Gouttebroze, A. Jouchoux, A. Vidal-Madjar, J.W. Leibacher, A. Skumanich, The LPSP instrument on OSO 8. ii—in-flight performance and preliminary results. Astrophys. J. **221**, 1032–1053 (1978). doi:10.1086/156109

J.C. Brandt, R.G. Roosen, R.S. Harrington, Interplanetary gas. xvii. an astrometric determination of solar wind velocities from orientations of ionic comet tails. Astrophys. J. **177**, 277–284 (1972). doi:10.1086/151706

J.C. Brandt, R.S. Harrington, R.G. Roosen, Interplanetary gas. xx. does the radial solar wind speed increase with latitude. Astrophys. J. **196**, 877–878 (1975). doi:10.1086/153478

M. Brasken, E. Kyrölä, Resonance scattering of Lyman alpha from interstellar hydrogen. Astron. Astrophys. **332**, 732–738 (1998)

J.S. Bridge, A. Egidi, A.J. Lazarus, E. Lyon, L. Jacobson, Preliminary results of plasma measurements on IMP-A, in *Space Research. V:969–978*, ed. by D.G. King-Hele, P. Muller, G. Righini (North Holland, Amsterdam, 1965)

M. Bzowksi, Time dependent radiation pressure and time dependent 2d ionisation rate for heliospheric modelling, in *The Outer Heliosphere: The Next Frontiers, Cospar Colloquia Series, vol. 11*, ed. by K. Scherer, H. Fichtner, H.-J. Fahr, E. Marsch (Pergamon Press, Amsterdam, 2001a), pp. 69–72

M. Bzowski, A model of charge exchange of interstellar hydrogen on a time-dependent, 2d solar wind. Space Sci. Rev. **97**, 379–383 (2001b). doi:10.1023/A:1011814125384

M. Bzowski, Response of the groove in heliospheric Lyman-α glow to latitude-dependent ionization rate. Astron. Astrophys. **408**, 1155–1164 (2003). doi:10.1051/0004-6361:20031023

M. Bzowski, Survival probability and energy modification of hydrogen energetic neutral atoms on their way from the termination shock to earth orbit. Astron. Astrophys. **488**, 1057–1068 (2008). doi:10.1051/0004-6361:200809393

M. Bzowski, D. Ruciński, Solar cycle modulation of the interstellar hydrogen density distribution in the heliosphere. Space Sci. Rev. **72**, 467–470 (1995a). doi:10.1007/BF00768821

M. Bzowski, D. Ruciński, Variability of the neutral hydrogen density distribution due to solar cycle related effects. Adv. Space Res. **16**, 131–134 (1995b). doi:10.1016/0273-1177(95)00325-9

M. Bzowski, D. Ruciński, Neutral solar wind evolution during solar cycle, in *Solar Wind Eight*, ed. by D. Winterhalter, J.T. Gosling, S.R. Habbal, W.S. Kurth, M. Neugebauer. AIP Conference Proceedings, vol. 382 (American Institute of Physics, Woodbury, New York, 1996), pp. 650–654. doi:10.1063/1.51452

M. Bzowski, S. Tarnopolski, Neutral atom transport from the termination shock to 1 au, in *Physics of the Inner Heliosheath*, ed. by J. Heerikhuisen, V. Florinski, G.P. Zank, N.V. Pogorelov. AIP Conference Series, vol. 858, pp. 251–256 (2006). doi:10.1063/1.2359335

M. Bzowski, H.-J. Fahr, D. Ruciński, H. Scherer, Variation of bulk velocity and temperature anisotropy of neutral heliospheric hydrogen during the solar cycle. Astron. Astrophys. **326**, 396–411 (1997)

M. Bzwoski, T. Summanen, D. Ruciński, E. Kyrölä, Response of interplanetary glow to global variations of hydrogen ionization rate and solar Lyman-α flux. J. Geophys. Res. **107**, ssh2-1 (2002). doi:10.1029/2001JA000141

M. Bzowski, T. Mäkinen, E. Kyrölä, T. Summanen, E. Quémerais, Latitudinal structure and north-south asymmetry of the solar wind from Lyman-α remote sensing by SWAN. Astron. Astrophys. **408**, 1165–1177 (2003). doi:10.1051/0004-6361:20031022

M. Bzowski, E. Möbius, S. Tarnopolski, V. Izmodenov, G. Gloeckler, Density of neutral interstellar hydrogen at the termination shock from Ulysses pickup ion observations. Astron. Astrophys. **491**, 7–19 (2008). doi:10.1051/0004-6361:20078810

M. Bzowski, E. Möbius, S. Tarnopolski, V. Izomdenov, G. Gloeckler, Neutral H density at the termination shock: a consolidation of recent results. Space Sci. Rev. **143**, 177–190 (2009)

S. Chabrillat, G. Kockarts, Simple parameterization of the absorption of the solar Lyman-alpha line. Geophys. Res. Lett. **24**, 2659–2662 (1997)

W.A. Coles, S. Maagoe, Solar-wind velocity from IPS observations. J. Geophys. Res. **77**, 5622–5624 (1972). doi: 10.1029/JA077i028p05622

W.A. Coles, B.J. Rickett, IPS observations of the solar wind speed out of the ecliptic. J. Geophys. Res. **81**, 4797–4799 (1976)

J.W. Cook, G.E. Brueckner, M.E. van Hoosier, Variability of the solar flux in the far ultraviolet 1175–2100 Å. J. Geophys. Res. **85**, 2257–2268 (1980)

J.W. Cook, R.R. Meier, G.E. Brueckner, M.E. van Hoosier, Latitudinal anisotropy of the solar far ultraviolet flux—effect on the Lyman alpha sky background. Astron. Astrophys. **97**, 394–397 (1981)

A.E. Covington, Micro-wave solar noise observations during the partial eclipse of November 23, 1946. Nature **159**, 405–406 (1947). doi:10.1038/159405a0

J.M.A. Danby, J.L. Camm, Statistical dynamics and accretion. Monthly Not. Royal Astron. Soc. **117**, 150 (1957)

G. de Toma, Evolution of coronal holes and implications for high-speed solar wind during the minimum between cycles 23 and 24. Solar Phys. **274**, 195–217 (2011). doi:10.1007/s11207-010-9677-2

P.A. Dennison, A. Hewish, The solar wind outside the plane of the ecliptic. Nature **213**, 343–346 (1967). doi:10.1038/213343a0

T. Dudok de Wit, J. Lilensten, J. Aboudarham, P.-O. Amblard, M. Kretzschmar, Retrieving the solar euv spectrum from a reduced set of spectral lines. Ann. Geophys. **23**, 3055 (2005)

T. Dudok de Wit, M. Kretzschmar, J. Aboudarham, P.-O. Amblard, F. Auchère, J. Lilensten, Which solar euv indices are best for reconstructing the solar euv irradiance? Adv. Space Res. **42**, 903–911 (2008). doi:10.1016/j.asr.2007.04.019

T. Dudok de Wit, M. Kretzschmar, J. Lilensten, T. Woods, Finding the best proxies for the solar uv irradiance. Geophys. Res. Lett. **36**, L10 (2009). doi:10.1029/2009/GL037825

R.W. Ebert, D.J. McComas, H.A. Elliott, R.J. Forsyth, J.T. Gosling, Bulk properites of the slow and fast solar wind and interplanetary coronal mass ejections measured by Ulysses: three polar orbits of observations. J. Geophys. Res. **114**, A1109 (2009). doi:10.1029/2008JA013631

C. Emerich, P. Lemaire, J.-C. Vial, W. Curdt, U. Schüle, K. Wilhelm, A new relation between the central spectral solar H I Lyman α irradiance and the line irradiance measured by sumer/SOHO during cycle 23. Icarus **178**, 429–433 (2005)

H.-J. Fahr, Non-thermal solar wind heating by supra-thermal ions. Solar Phys. **30**, 193–206 (1973)

H.-J. Fahr, Change of interstellar gas parameters in stellar wind dominated atmospheres: solar case. Astron. Astrophys. **66**, 103–117 (1978)

H.-J. Fahr, Interstellar hydrogen subject to a net repulsive solar force field. Astron. Astrophys. **77**, 101–109 (1979)

H.-J. Fahr, The 3d heliosphere: three decades of growing knowledge. Adv. Space Res. **32**, 3–13 (2004)

H.-J. Fahr, D. Ruciński, Neutral interestellar gas atoms reducing the solar wind number and fractionally neutralizing the solar wind. Astron. Astrophys. **350**, 1071–1078 (1999)

H.-J. Fahr, D. Ruciński, Modification of properties and dynamics of distant solar wind due to its interaction with neutral interstellar gas. Space Sci. Rev. **97**, 407–412 (2001). doi:10.1023/A:1011874311272

H.-J. Fahr, D. Ruciński, Heliospheric pick-up ions influencing thermodynamics and dynamics of the distant solar wind. Nonlinear Proc. Geophys. **9**, 377–386 (2002)

H.-J. Fahr, K. Scherer Perturbations of the solar wind flow by radial and latitudinal pick-up ion pressure gradients. Ann. Geophys. **22**, 2229–2238 (2004)

H.-J. Fahr, H. Fichtner, K. Scherer, Theoretical aspects of energetic neutral atoms as messengers from distant plasma sites with emphasis on the heliosphere. Rev. Geophys. **45**, RG4003 (2007). doi:10.1029/2006RG000214

W.C. Feldman, J.R. Asbridge, S.J. Bame, M.D. Montgomery, Double ion streams in the solar wind. J. Geophys. Res. **78**, 2017–2027 (1973). doi:10.1029/JA078i013p02017

W.L. Fite, A.C.S. Smith, R.F. Stebbins, Charge transfer in collisions involving symmetric and asymmetric resonance. Proc. R. Soc. London Ser. A **268**, 527 (1962)

L. Floyd, D.K. Prinz, P.C. Crane, L.C. Herring, Solar uv irradiance variation during cycles 22 and 23. Adv. Space Res. **29**, 1957–1962 (2002)

L. Floyd, G. Rottman, M. Deland, J. Pap, 11 years of solar uv irradiance measurements from UARS, in *Solar Variability as an Input to the Earth's Environment*, ed. by A. Wilson. ESA SP-535, pp. 195–203 (2003)

L. Floyd, J. Newmark, J. Cook, L. Herring, D. McMullin, Solar euv and uv spectral irradiances and solar indices. J. Atmos. Sol. Terr. Phys. **67**, 3–15 (2005). doi:10.1016/j.jastp.2004.07.013

P.C. Frisch, M. Bzowski, E. Grün, V. Izmodenov, H. Krüger, J.L. Linsky, D.J. McComas, E. Möbius, S. Redfield, N. Schwadron, R. Shelton, J.D. Slavin, B.E. Wood, The galactic environment of the sun: interstellar material inside and outside of the heliosphere. Space Sci. Rev. **146**, 235–273 (2009). doi:10.1007/s11214-009-9502-0

P.C. Frisch, S. Redfield, J.D. Slavin, The interstellar medium surrounding the sun. Ann. Rev. Astron. Astrophys. **49**, 237–279 (2011). doi:10.1146/annurev-astro-081710-102613

K. Fujiki, M. Kojima, M. Tokumaru, T. Ohmi, A. Yokobe, K. Hayashi, Solar cycle dependence of high-latitude solar wind, in *Solar Wind Ten*, ed. by M. Velli, R. Bruno, F. Malara, B. Bucci. American Institute of Physics Conference Series, vol. 679 (American Institute of Physics, Woodbury, New York, 2003a), pp. 141–143. doi:10.1063/1.1618561

K. Fujiki, M. Kojima, M. Tokumaru, T. Ohmi, A. Yokobe, K. Hayashi, D.J. McComas, H.A. Elliott, Solar wind velocity structure around the solar maximum observed by interplanetary scintillation, in *Solar Wind Ten*, ed. by M. Velli, R. Bruno, F. Malara, B. Bucci. American Institute of Physics Conference Series, vol 679 (American Institute of Physics, Woodbury, New York, 2003b) pp. 226–229. doi:10.1063/1.1618583

K. Fujiki, M. Kojima, M. Tokumaru, T. Ohmi, A. Yokobe, K. Hayashi, D.J. McComas, H.A. Elliott, How did the solar wind structure change around the solar maximum? from interplanetary scintillation observation. Ann. Geophys. **21**, 1257–1261 (2003c). doi:10.5194/angeo-21-1257-2003

G. Gloeckler, J. Geiss, Heliospheric and interstellar phenomena deduced from pickup ion observations. Space Sci. Rev. **97**, 169–181 (2001)

G. Gloeckler, J. Geiss, H. Balsiger, P. Bedini, J.C. Cain, J. Fisher, L.A. Fisk, A.B. Galvin, F. Gliem, D.C. Hamilton, The solar wind ion composition spectrometer. Astron. Astrophys. Supp. **92**, 267–289 (1992)

G. Gloeckler, J. Geiss, H. Balsinger, L.A. Fisk, A.B. Galvin, F.M. Ipavich, K.W. Ogilvie, R. von Steiger, B. Wilken, Detection of interstellar pickup hydrogen in the solar system. Science **261**, 70–73 (1993)

G. Gloeckler, E. Möbius, J. Geiss, M. Bzowksi, S. Chalov, H.-J. Fahr, D.R. McMullin, H. Noda, M. Oka, D. Ruciński, R. Skoug, T. Terasawa, R. von Steiger, A. Yamazaki, T. Zurbuchen, Observations of the helium focusing cone with pickup ions. Astron. Astrophys. **426**, 845–854 (2004)

K. Gringauz, V. Bezrukih, V. Ozerov, R. Ribchinsky, A study of the interplanetary ionized gas, high-energy electrons and corpuscular radiation from the sun by means of hte three electrode trap for charged particles on the second soviet cosmic rocket. Sov. Phys. Doklady **5**, 361 (1960)

M.A. Gruntman, Neutral solar wind properties: advance warning of major geomagnetic storms. J. Geophys. Res. **99**, 19213–19227 (1994)

J.K. Harmon, Scintillation studies of density microstructure in the solar wind plasma. Dissertation, University of California, San Diego, 1975

K.L. Harvey, F. Recely, Polar coronal holes during cycles 22 and 23. Solar Phys. **211**, 31–52 (2002)

K. Hayashi, M. Kojima, M. Tokumaru, K. Fujiki, MHD tomography using interplanetary scintillation measurement. J. Geophys. Res. **108**, 1102 (2003). doi:10.1029/2002JA009567

D.F. Heath, B.M. Schlesinger, The Mg 280-nm doublet as a monitor of changes in solar ultraviolet irradiance. J. Geophys. Res. **91**, 8672–8682 (1986). doi:10.1029/JD091iD08p08672

A. Hewish, M.D. Symonds, Radio investigation of the solar plasma. Planet. Space Sci. **17**, 313 (1969). doi:10.1016/0032-0633(69)90064-6

A. Hewish, P.F. Scott, D. Wills, Interplanetary scintillation of small diameter radio sources. Nature **203**, 1214–1217 (1964). doi:10.1038/2031214a0

H.E. Hinteregger, K. Fukui, B.R. Gilson, Observational, reference and model data on solar euv, from measurements on AE-E. Geophys. Res. Lett. **8**, 1147–1150 (1981). doi:10.1029/GL008i011p01147

Z. Houminer, Radio source scintillation—evidence of plasma streams corotating about the sun. Nature **231**, 165 (1971)

D. Hovestadt, M. Hilchenbach, A. Bürgi, B. Klecker, P. Laeverenz, M. Scholer, H. Grünwaldt, W.I. Axford, S. Livi, E. Marsch, B. Wilken, H.P. Winterhoff, F.M. Ipavich, P. Bedini, M.A. Coplan, A.B. Galvin, G. Gloeckler, P. Bochsler, H. Balsiger, J. Fischer, J. Geiss, R. Kallenbach, P. Wurz, K.-U. Reiche, F. Gliem, D.L. Judge, H.S. Ogawa, K.C. Hsieh, E. Möbius, M.A. Lee, G.G. Managadze, M.I. Verigin, M. Neugebauer, CELIAS—

charge, element and isotope analysis system for SOHO. Solar Phys. **162**, 441–481 (1995). doi:10.1007/BF00733436

A.J. Hundhausen, J.R. Asbridge, S.J.B.H.E. Gilbert, I.B. Strong, Vela 3 satellite observations of solar wind ions. J. Geophys. Res. **72**, 1979 (1967). doi:10.1029/JZ072i007p01979

T. Isobe, E.D. Feigelson, M.G. Akritas, G.J. Babu, Linear regression in astronomy. Astrophys. J. **364**, 104–113 (1990). doi:10.1086/169390

K. Issautier, Diagnostics of the solar wind plasma, in *Turbulence in Space Plasmas*, ed. by P. Cargill, L. Vlahos. Lecture Notes in Physics, vol. 778 (Springer, Berlin, 2009), pp. 223–246

K. Issautier, N. Meyer-Vernet, M. Moncuquet, S. Hoang, Solar wind radial and latitudinal structure—electron density and core temperature from Ulysses thermal noise spectroscopy. J. Geophys. Res. **103**, 1969–1979 (1998)

K. Issautier, R.M. Skoug, J.T. Gosling, S.P. Gary, D.J. McComas, Solar wind plasma parameters on Ulysses: detailed comparison between the urap and swoops experiments. J. Geophys. Res. **106**, 15665–15676 (2001). doi:10.1029/2000JA000412

V.V. Izmodenov, V.B. Baranov, Modern multi-component models of the heliospheric interface, in *The Physics of the Heliospheric Boundaries*, ed. by V.V. Izmodenov, R. Kallenbach. ISSI Scientific Report Series, SR-005, pp. 67–136 (2006)

V.V. Izmodenov, Y.G. Malama, A.P. Kalinin, M. Gruntman, R. Lallement, I.P. Rodionova, Hot neutral H in the heliosphere: elastic H-H, H-p collisions. Astrophys. Space Sci. **274**, 71–76 (2000). doi:10.1023/A:1026531519864

V.V. Izmodenov, D.B. Alexashov, S.V. Chalov, O.A. Katushkina, Y.G. Malama, E.A. Provornikova, Kinetic-gasdynamic modeling of the heliospheric interface: global structure, interstellar atoms and heliospheric enas. Space Sci. Rev. **146**, 329–351 (2009). doi:10.1007/s11214-009-9528-3

V.V. Izmodenov, O.A. Katushkina, E. Quémerais, M. Bzowski, Distribution of interstellar H atoms in the heliosphere and backscattered solar Lyman-α, in *Cross-Calibration of Far uv Spectra of Solar System Objects and the Heliosphere*, ed. by E. Quémerais, M. Snow, R.M. Bonnet. ISSI Scientific Report Series, SR-013 (2013) (this volume)

B.V. Jackson, P.L. Hick, M. Kojima, A. Yokobe, Heliospheric tomography using interplanetary scintillation observations. Adv. Space Res. **20**, 23–26 (1997). doi:10.1016/S0273-1177(97)00474-2

B.V. Jackson, P.L. Hick, M. Kojima, A. Yokobe, Heliospheric tomography using interplanetary scintillation observations. i. combined nagoya and cambridge data. J. Geophys. Res. **103**, 12049–12067 (1998)

D.L. Judge, D.R. McMullin, H.S. Ogawa, D. Hovestadt, B. Klecker, M. Hilchenbach, E. Möbius, L.R. Canfield, R.E. Vest, R. Watts, C. Tarrio, M. Kuehne, P. Wurz, First solar euv irradiances obtained from SOHO by the CELIAS/SEM. Solar Phys. **177**, 161–173 (1998)

J.C. Kasper, Solar wind plasma: kinetic properties and micro-instabilities. Dissertation, Massachusetts Institute of Technology, Cambridge, 2002

J.C. Kasper, A.J. Lazarus, J.T. Steinberg, K.W. Ogilvie, A. Szabo, Physics-based tests to identify the accuracy of solar wind ion measurements: a case study with the wind faraday cups. J. Geophys. Res. **111**, A03105 (2006). doi:10.1029/2005JA011442

J.C. Kasper, M.L. Stevens, K.E. Korreck, B.A. Maruca, K.K. Kiefer, N.A. Schwadron, S.T. Lepri, Evolution of the relationships between helium abundance, minor ion charge state, and solar wind speed over the solar cycle. Astrophys. J. **745**, 162 (2012). doi:10.1088/0004-637X/745/2/162

O.A. Katushkina, V.V. Izmodenov, Effect of the heliospheric interface on the distribution of interstellar hydrogen atom inside the heliosphere. Astron. Lett. **36**, 297–306 (2010). doi:10.1134/S1063773710040080

J.H. King, N.E. Papitashvili, Solar wind spatial scales in and comparisons of hourly wind and acd plasma and magnetic field data. J. Geophys. Res. **110**, 2104–2111 (2005). doi:10.1029/2004JA010649

D. Kiselman, T. Pereira, B. Gustafsson, M. Asplund, J. Meléndez, K. Langhans, Is the solar spectrum latitude dependent? an investigation with SST/TRIPPEL. Astron. Astrophys. **535**, A18 (2011)

M. Kojima, T. Kakinuma, Solar cycle evolution of solar wind speed structure between 1973 and 1985 observed with the interplanetary scintillation method. J. Geophys. Res. **92**, 7269–7279 (1987). doi:10.1029/JA092iA07p07269

M. Kojima, T. Kakinuma, Solar cycle dependence of global distribution of solar wind speed. Space Sci. Rev. **53**, 173–222 (1990). doi:10.1007/BF00212754

M. Kojima, M. Tokumaru, H. Watanabe, A. Yokobe, K. Asai, B.V. Jackson, P.L. Hick, Heliospheric tomography using interplanetary scintillation observations. 2. latitude and heliocentric distance dependence of solar wind structure at 0.1-1 au. J. Geophys. Res. **103**, 1981–1989 (1998)

M. Kojima, K. Fujiki, T. Ohmi, M. Tokumaru, A. Yokobe, K. Hakamada, The highest solar wind velocity in a polar region estimated from IPS tomography analysis. Space Sci. Rev. **87**, 237–239 (1999). doi:10.1023/A:1005108820106

M. Kojima, K. Fujiki, T. Ohmi, M. Tokumaru, A. Yokobe, K. Hakamada, Latitudinal velocity structures up to the solar poles estimated from interplanetary scintillation tomography analysis. J. Geophys. Res. **106**, 15677–15686 (2001)

M. Kojima, M. Tokumaru, K. Fujiki, K. Hayashi, B.V. Jackson, IPS tomographic observations of 3d solar wind structure. Astron. Astrophys. Trans. **26**, 467–476 (2007)

M. Kretzschmar, J. Lilensten, J. Aboudarham, Retrieving the solar euv spectral irradiance from the observation of 6 lines. Adv. Space Res. **37**, 341–346 (2006). doi:10.1016/j.asr.2005.02.029

S. Kumar, A.L. Broadfoot, Evidence from mariner 10 of solar wind flux depletion at high ecliptic latitudes. Astron. Astrophys. **69**, L5-L8 (1978).

S. Kumar, A.L. Broadfoot, Signatures of solar wind latitudinal structure in interplanetary Lyman-α emissions: mariner 10 observations. Astrophys. J. **228**, 302–311 (1979)

E. Kyrölä, T. Summanen, P. Råback, Solar cycle and interplanetary hydrogen. Astron. Astrophys. **288**, 299–314 (1994)

E. Kyrölä, T. Summanen, T. Mäkinen, E. Quémerais, J.-L. Bertaux, R. Lallement, J. Costa, Preliminary retrieval of solar wind anisotropies / SOHO observations. J. Geophys. Res. **103**, 14523–14538 (1998)

R. Lallement, A.I. Stewart, Out-of-ecliptic lyman-alpha observations with Pioneer-Venus: solar wind anisotropy degree in 1986. Astron. Astrophys. **227**, 600–608 (1990)

R. Lallement, J.-L. Bertaux, F. Dalaudier, Interplanetary lyman α spectral profiles and intensities for both repulsive and attractive solar force fields: predicted absorption pattern by a hydrogen cell. Astron. Astrophys. **150**, 21–32 (1985a)

R. Lallement, J.-L. Bertaux, V.G. Kurt, Solar wind decrease at high heliographic latitudes detected from prognoz interplanetary lyman alpha mapping. J. Geophys. Res. **90**, 1413–1420 (1985b)

R. Lallement, T.E. Holzer, R.H. Munro, Solar wind expansion in a polar coronal hole: inferences from coronal white light and interplanetary lyman alpha observations. J. Geophys. Res. **91**, 6751–6759 (1986)

R. Lallement, E. Quémerais, P. Lamy, J.L. Bertaux, S. Ferron, W. Schmidt, The solar wind as seen by SOHO/SWAN since 1996: comparison with SOHO/LASCO C2 coronal densities. In *Proceedings of SOHO 23 Workshop*, ed. by S. Cranmer, T. Hoeksma, J. Kohl. ASP Conference Series, vol. 428 (2010), pp. 253–258

A.J. Lazarus, K. Paularena, A comparison of solar wind parameters from experiments on the IMP 8 and Wind spacecraft. In *Measurement Techniques in Space Plasmas*, ed. by E. Borovsky, F. Pfaff, T. Young. AGU Geophysical Monograph Series, vol. 102 (1998), pp. 85–90

G. Le Chat, K. Issautier, N. Meyer-Vernet, I. Zouganelis, M. Moncuquet, S. Hoang, Quasi-thermal noise spectroscopy: preliminary comparison between kappa and sum of two Maxwellian distributions, in *Twelfth International Solar Wind Conference*, vol. 1216, pp. 316–319 (2010). doi:10.1063/1.3395864

G. Le Chat, K. Issautier, N. Meyer-Vernet, S. Hoang, Large-scale variation of solar wind electron properties from quasi-thermal noise spectroscopy: Ulysses measurements. Solar Phys. **271**, 141–148 (2011). doi:10.1007/s11207-011-9797-3

J.L. Lean, H.P. Warren, J.T. Mariska, J. Bishop, A new model of solar euv irradiance variability 2. comparisons with empirical models and observations and implications for space weather. J. Geophys. Res. **108**, 1059 (2003). doi:10.1029/2001JA009238

J.L. Lean, T.N. Woods, F.G. Eparvier, R.R. Meier, D.J. Strickland, J.T. Correira, J.S. Evans, Solar extreme ultraviolet irradiance: present, past, and future. J. Geophys. Res. **116**, A01102 (2011). doi:10.1029/2010JA015901

M.A. Lee, H.J. Fahr, H. Kucharek, E. Möbius, C. Prested, N.A. Schwadron, P. Wu, Physical processes in the outer heliosphere. Space Sci. Rev. **146**, 275–294 (2009). doi:10.1007/s11214-009-9522-9

P. Lemaire, J. Charra, A. Jouchoux, A. Vidal-Madjar, G.E. Artzner, J.C. Vial, R.M. Bonnet, A. Skumanich, Calibrated full disk solar H I Lyman-alpha and Lyman-beta profiles. Astrophys. J. Lett. **223**, L55–L58 (1978). doi:10.1086/182727

P. Lemaire, C. Emerich, W. Curdt, U. Schühle, K. Wilhelm, Solar HI Lyman α full disk profile obtained with the SUMER/SOHO spectrometer. Astron. Astrophys. **334**, 1095–1098 (1998)

P.L. Lemaire, C. Emerich, J.-C. Vial, W. Curdt, U. Schühle, K. Wilhelm, Variation of the full sun hydrogen lyman α and β profiles with the activity cycle, in ESSP A-508: From solar min to max: half a solar cycle with SOHO, 2002, pp. 219–222

P. Lemaire, C. Emerich, J.-C. Vial, W. Curdt, U. Schühle, K. Wilhelm, Variation of the full sun hydrogen Lyman profiles through solar cycle 23. Adv. Space Res. **35**, 384–387 (2005)

P.C. Liewer, B.E. Goldstein, N. Omidi, Hybrid simulations of the effects of interstellar pickup hydrogen on the solar wind termination shock. J. Geophys. Res. **981**, 15211–15220 (1993). doi:10.1029/93JA01172

B.G. Lindsay, R.F. Stebbings, Charge transfer cross sections for energetic neutral atom data analysis. J. Geophys. Res. **110**, A12213 (2005). doi:10.1029/2005JA011298

W. Lotz, An empirical formula for the electron-impact ionization cross-section. Zeitschrift f. Phys. **206**, 205–211 (1967a)

W. Lotz, Electron-impact ionization cross-sections and ionization rate coefficients for atoms and ions. Ap. J. Suppl. **14**, 207–238 (1967b)

E.F. Lyon, H.S. Bridge, J.H. Binsack, Explorer 35 plasma measurements in the vicinity of the moon. J. Geophys. Res. **72**, 6113–6117 (1967). doi:10.1029/JZ072i023p06113

E.F. Lyon, A. Egidi, G. Pizella, H.S. Bridge, J.S. Binsack, R. Baker, R. Butler, Plasma measurements on Explorer 33 (I) interplanetary region. Space Research, **VIII**, 99 (1968)

L.J. Maher, B.A. Tinsley, Atomic hydrogen escape rate due to charge exchange with hot plasmaspheric ions. J. Geophys. Res. **82**, 689–695 (1977)

M. Maksimovic, V. Pierrard, P. Riley, Ulysses distributions fitted with Kappa functions. Geophys. Res. Lett. **24**, 1151–1154 (1997). doi:10.1029/97GL00992

M. Maksimovic, S.P. Gary, R.M. Skoug, Solar wind electron suprathermal strength and temperature gradients: Ulysses observations. J. Geophys. Res. **105**, 18337–18350 (2000)

M. Maksimovic, I. Zouganelis, J.-Y. Chaufray, K. Issautier, E.E. Scime, J.E. Littleton, E. Marsch, D.J. McComas, C. Salem, R.P. Lin, H. Elliott, Radial evolution of the electron distribution functions in the fast solar wind between 0.3 and 1.5 AU. J. Geophys. Res. **110**, A9104 (2005). doi:10.1029/2005JA011119

Y. Malama, V.V. Izmodenov, S.V. Chalov, Modeling of the heliospheric interface: multi-component nature of the heliospheric plasma. Astron. Astrophys. **445**, 693–701 (2006)

P.K. Manoharan, Three-dimensional structure of the solar wind: Variation of density with the solar cycle. Sol. Phys. **148**, 153–167 (1993). doi:10.1007/BF00675541

R.G. Marsden, E.J. Smith, Ulysses: a summary of the first high-latitude survey. Adv. Space Res. **19**, (6)825–(6)834 (1997)

D.J. McComas, S. J. Bame, P. Barker, W. C. Feldman, J. L. Phillips, P. Riley, J.W. Griffee, Solar wind electron proton alpha monitor (SWEPAM) for the Advanced Composition Explorer. Space Sci. Rev. **86**, 563–612 (1998a)

D.J. McComas, S.J. Bame, B.L. Barraclough, W.C. Feldman, W.C. Funsten, J.T. Gosling, P. Riley, R. Skoug, Ulysses' return to the slow solar wind. Geophys. Res. Lett. 25(1), 1-4 (1998)

D.J. McComas, H.O. Funsten, J.T. Gosling, W.R. Pryor, Ulysses measurements of variations in the solar wind – interstellar hydrogen charge exchange rate. Geophys. Res. Lett. **26**, 2701–2704 (1999)

D.J. McComas, B.L. Barraclough, H.O. Funsten, J.T. Gosling, E. Santiago-Muñoz, B.E. Goldstein, M. Neugebauer, P. Riley, A. Balogh, Solar wind observations over Ulysses first full polar orbit. J. Geophys. Res. **105**, 10419–10433 (2000a)

D.J. McComas, J.T. Gosling, R.M. Skoug, Ulysses observations of the irregularly structured mid-latitude solar wind during the approach to solar maximum. Geophys. Res. Lett. **27**, 2437–2440 (2000b)

D.J. McComas, H.A. Elliot, R. von Steiger, Solar wind from high-latitude coronal holes at solar maximum. Geophys. Res. Lett. **29**, 1314 (2002a). doi:10.1029/2001GL013940

D.J. McComas, H.A. Elliott, J.T. Gosling, D.B. Reisenfeld, R.M. Skoug, B.E. Goldstein, M. Neugebauer, A. Balogh, Ulysses second fast-latitude scan: Complexity near solar maximum and the reformation of polar coronal holes. Geophys. Res. Lett. **29**, 1290 (2002b). doi:10.1029/2001GL014164

D.J. McComas, H.A. Elliot, N.A. Schwadron, J.T. Gosling, R.M. Skoug, B.E. Goldstein, The three-dimensional solar wind around solar maximum, Geophys. Res. Lett. **30**, 24–1, (2003). doi:10.1029/2003GL017136

D.J. McComas, F. Allegrini, L. Bartolone, P. Bochsler, M. Bzowski, M. Collier, H. Fahr, H. Fichtner, P. Frisch, H. Funsten, S. Fuselier, G. Gloeckler, M. Gruntman, V. Izmodenov, P. Knappenberger, M. Lee, S. Livi, D. Mitchell, E. Möbius, T. Moore, S. Pope, D. Reisenfeld, E. Roelof, H. Runge, J. Scherrer, N. Schwadron, R. Tyler, M. Wieser, M. Witte, P. Wurz, G. Zank, The Interstellar Boundary Explorer (IBEX): Update at the end of phase B, in *Physics of the Inner Heliosheath*, ed. by J. Heerikhuisen, V. Florinski, G.P. Zank, N.V. Pogorelov. American Institute of Physics Conference Series, vol. 858 (American Institute of Physics, Woodbury, New York, 2006), pp. 241–250

D.J. McComas, R.W. Ebert, H.A. Elliot, B.E. Goldstein, J.T. Gosling, N.A. Schwadron, R.M. Skoug, Weaker solar wind from the polar coronal holes and the whole sun, Geophys. Res. Lett. **35**, L18103 (2008). doi:10.1029/2008GL034896

D.J. McComas, F. Allegrini, P. Bochsler, M. Bzowski, E.R. Christian, G.B. Crew, R. DeMajistre, H. Fahr, H. Fichtner, P.C. Frisch, H.O. Funsten, S.A. Fuselier, G. Gloeckler, M. Gruntman, J. Heerikhuisen, V. Izmodenov, P. Janzen, P. Knappenberger, S. Krimigis, H. Kucharek, M. Lee, G. Livadiotis, S. Livi, R.J. MacDowall, D. Mitchell, E. Möbius, T. Moore, N.V. Pogorelov, D. Reisenfeld, E. Roelof, L. Saul, N.A. Schwadron, P.W. Valek, R. Vanderspek, P. Wurz, G.P. Zank, Global observations of the interstellar interaction from the Interstellar Boundary Explorer (IBEX). Science **326**, 959–962 (2009a). doi:10.1126/science.1180906

D.J. McComas, F. Allegrini, P. Bochsler, M. Bzowski, M. Collier, H. Fahr, H. Fichtner, P. Frisch, H.O. Funsten, S.A. Fuselier, G. Gloeckler, M. Gruntman, V. Izmodenov, P. Knappenberger, M. Lee, S. Livi, D. Mitchell, E. Möbius, T. Moore, S. Pope, D. Reisenfeld, E. Roelof, J. Scherrer, N. Schwadron, R. Tyler, M. Wieser, M. Witte, P. Wurz, G. Zank, IBEX - Interstellar Boundary Explorer, Space Sci. Rev. **146**, 11–33 (2009b). doi:10.1007/s11214-009-9499-4

E. Möbius, D. Hovestadt, B. Klecker, M. Scholer, G. Gloeckler, Direct observation of He+ pick-up ions of interstellar origin in the solar wind. Nature **318**, 426–429 (1985)

E. Möbius, B. Klecker, D. Hovestadt, M. Scholer, Interaction of interstellar pick-up ions with the solar wind. Astrophys. Space Sci. **144**, 487–505 (1988)

M. Neugebauer, Initial deceleration of solar wind positive ions in the earth's bow shock. J. Geophys. Res. **75**, 717–733 (1970)

M. Neugebauer, C.W. Snyder, Solar plasma experiment. Science **138**, 1095–1097 (1962). doi:10.1029/JA075i004p00717

H.S. Ogawa, C.Y.R. Wu, P. Gangopadhyay, D.L. Judge, Solar photoionization as a loss mechanism of neutral interstellar hydrogen in interplanetary space. J. Geophys. Res. **100**, 3455–3462 (1995)

K.W. Ogilvie, L.F. Burlaga, T.D. Wilkerson, Plasma observations on Explorer 34. J. Geophys. Res. **73**, 6809–6824 (1968). doi:10.1029/JA073i021p06809

T. Ohmi, M. Kojima, A. Yokobe, M. Tokumaru, K. Fujiki, K. Hakamada, Polar low-speed solar wind at the solar activity maximum. J. Geophys. Res. **106**, 24923–24936 (2001). doi:10.1029/2001JA900094

T. Ohmi, M. Kojima, K. Fujiki, M. Tokumaru, K. Hayashi, K. Hakamada, Polar low-speed solar wind reappeared at the solar activity maximum of cycle 23. Geophys. Res. Lett. **30**, 1409 (2003). doi:10.1029/2002GL016347

R. Osterbart, H.-J. Fahr, A Boltzmann-kinetic approach to describe entrance of neutral interstellar hydrogen into the heliosphere. Astron. Astrophys. **264**, 260–269 (1992)

S.P. Owocki, T.E. Holzer, A.J. Hundhausen, The solar wind ionization state as a coronal temperature diagnostic. Astrophys. J. **275**, 354–366 (1983)

E.N. Parker, Dynamics of the interplanetary gas and magnetic fields. Astrophys. J. **128**, 664–676 (1958)

J.L. Phillips, S.J. Bame, A. Barnes, B.L. Barrcalough, W.C. Feldman, B.E. Goldstein, J.T. Gosling, G.W. Hoogveen, D.J. McComas, M. Neugebauer, S.T. Suess, Ulysses solar wind plasma observations from pole to pole. Geophys. Res. Lett. **22**, 3301–3304 (1995a)

J.L. Phillips, S.J. Bame, W.C. Feldman, J.T. Gosling, C.M. Hammond, D.J. McComas, B.E. Goldstein, M. Neugebauer, Ulysses solar wind plasma observations during the declining phase of solar cycle 22. Adv. Space Res. **16**, (9)85–(9)94 (1995b)

W.G. Pilipp, K.-H. Muehlhaeuser, H. Miggenrieder, M.D. Montgomery, H. Rosenbauer, Unusual electron distribution functions in the solar wind derived from the HELIOS plasma experiment—double-strahl distributions and distributions with an extremely anisotropic core. J. Geophys. Res. **92**, 1093–1101 (1987a)

W.G. Pilipp, K.-H. Muehlhaeuser, H. Miggenrieder, M.D. Montgomery, H. Rosenbauer, Characteristics of electron velocity distribution functions in the solar wind derived from the HELIOS plasma experiment. J. Geophys. Res. **92**, 1075–1092 (1987b)

W.R. Pryor, J.M. Ajello, C.A. Barth, C.W. Hord, A.I.F. Stewart, K.E. Simmons, W.E. McClintock, B.R. Sandel, D.E. Shemansky, The Galileo and Pioneer Venus ultraviolet spectrometer experiments: solar Lyman-α latitude variation at solar maximum from interplanetary Lyman-α observations. Astrophys. J. **394**, 363–377 (1992)

W.R. Pryor, M. Witte, J.M. Ajello, Interplanetary Lyman α remote sensing with the Ulysses interstellar neutral gas experiment. J. Geophys. Res. **103**, 26813–26831 (1998)

W.R. Pryor, J.M. Ajello, D.J. McComas, M. Witte, W.K. Tobiska, Hydrogen atom lifetimes in the three-dimensional heliosphere over the solar cycle. J. Geophys. Res. **108**, 8034 (2003). doi:10.1029/2003JA009878

E. Quémerais, The interplanetary Lyman-α background, in *The Physics of the Heliospheric Boundaries*, ed. by V.V. Izmodenov, R. Kallenbach, ISSI Scientific Report Series, SR-005, pp. 283–310 (2006)

E. Quémerais, R. Lallement, S. Ferron, D. Koutroumpa, J.-L. Bertaux, E. Kyrölä, W. Schmidt, Interplanetary hydrogen absolute ionization rates: retrieving the solar wind mass flux latitude and cycle dependence with SWAN/SOHO maps. J. Geophys. Res. **111**, 9114–9131 (2006). doi:10.1029/2006JA011711

P.G. Richards, J.A. Fennelly, D.G. Torr, EUVAC: a solar euv flux model for aeronomic calculations. J. Geophys. Res. **99**, 8981–8992 (1994). doi:10.1029/94JA00518

J.D. Richardson, K.I. Paularena, A.J. Lazarus, J.W. Belcher, Radial evolution of the solar wind from IMP-8 to Voyager 2. Geophys. Res. Lett. **22**, 325–328 (1995)

J.D. Richardson, J.C. Kasper, C. Wang, J.W. Belcher, A.J. Lazarus, Cool heliosheath plasma and deceleration of the upstream solar wind at the termination shock. Nature **454**, 63–66 (2008a). doi:10.1038/nature07024

J.D. Richardson, Y. Liu, C. Wang, D.J. McComas, Determining the LIC H density from the solar wind slow down. Astron. Astrophys. **491**, 1–5 (2008b). doi:10.1051/0004-6361:20078565

D. Ruciński, M. Bzowski, Solar cycle dependence of the production of H+ pick-up ions in the inner heliosphere. Adv. Space Res. **16**, 121–124 (1995)

D. Ruciński, H.-J. Fahr, The influence of electron impact ionization on the distribution of interstellar helium in the inner heliosphere: possible consequences for determination of interstellar helium parameters. Astron. Astrophys. **224**, 290–298 (1989)

D. Ruciński, H.-J. Fahr, Nonthermal ions of interstellar origin at different solar wind conditions. Ann. Geophys. **9**, 102–110 (1991)

D. Ruciński, M. Bzowski, H.-J. Fahr, Minor helium components co-moving with the solar wind. Astron. Astrophys. **334**, 337–354 (1998)

C. Salem, J.-M. Bosqued, D.E. Larson, A. Mangeney, M. Maksimovic, C. Perche, R.P. Lin, J.-L. Bougeret, Determination of accurate solar wind electron parameters using particle detectors and radio wave receivers. J. Geophys. Res. **106**, 21701–21717 (2001). doi:10.1029/2001JA900031

C. Salem, S. Hoang, K. Issautier, M. Maksimovic, C. Perche, WIND-Ulysses in-situ thermal noise measurements of solar wind electron density and core temperature at solar maximum and minimum. Adv. Space Res. **32**, 491–496 (2003). doi:10.1016/S0273-1177(03)00354-5

H. Scherer, M. Bzowski, H.-J. Fahr, D. Ruciński, Improved analysis of interplanetary HST-$H_{Ly\alpha}$ spectra using time-dependent modelings. Astron. Astrophys. **342**, 601–609 (1999)

H. Scherer, H.-J. Fahr, M. Bzowski, D. Ruciński, The influence of fluctuations of the solar emission line profile on the Doppler shift of interplanetary H Lyα lines observed by the Hubble-Space-Telescope. Astrophys. Space Sci. **274**, 133–141 (2000)

E.E. Scime, S.J. Bame, W.C. Feldman, S.P. Gary, J.L. Phillips, Regulation of the solar wind electron heat flux from 1 to 5 au JGR **99**, 23401–23410 (1994)

G.J. Smith, L.K. Johnson, R.S. Gao, K.A. Smith, R.F. Stebbings, Absolute differential cross sections for electron capture and loss by kilo-electron-volt hydrogen atoms. Phys. Rev. A **44**, 5647–5652 (1991)

J.M. Sokół, M. Bzowski, M. Tokumaru, K. Fujiki, D.J. McComas, Heliolatitude and time variations of solar wind structure from in-situ measurements and interplanetary scintillation observations. Solar Phys. (2012). doi: 10.1007/s11207-012-9993-9.

Š. Štverák, P.M. Trávníček, M. Maksimovic, E. Marsch, A.N. Fazakerley, E.E. Scime, Electron temperature anisotropy constraints in the solar wind. J. Geophys. Res. **113**, A03103 (2008). doi:10.1029/2007JA012733

Š. Štveràk, M. Maksimovic, P.M. Trávníček, E. Marsch, A.N. Fazakerley, E.E. Scime, Radial evolution of nonthermal electron populations in the low-latitude solar wind: Helios, Cluster, and Ulysses observations. J. Geophys. Res. **114**, A05104 (2009). doi:10.1029/2008JA013883

T. Summanen, The effect of the time and latitude-dependent solar ionisation rate on the measured Lyman-α-intensity. Astron. Astrophys. **314**, 663–671 (1996)

T. Summanen, R. Lallement, J.-L. Bertaux, E. Kyrölä, Latitudinal distribution of solar wind as deduced from Lyman alpha measurements: an improved method. J. Geophys. Res. **98**, 13215–13224 (1993)

K.F. Tapping, Recent solar radio astronomy at centimeter wavelengths - the temporal variability of the 10.7-cm flux. J. Geophys. Res. **92**, 829–838 (1987). doi:10.1029/JD092iD01p00829

S.T. Tarnopolski, Expected distribution of interstellar deuterium in the heliosphere. Dissertation. Space Research Centre PAS, 2007

S. Tarnopolski, M. Bzowski, Detectability of neutral interstellar deuterium by a forthcoming SMEX mission IBEX. Astron. Astrophys. **483**, L35-L38 (2008a). doi:10.1051/0004-6361:200809593

S. Tarnopolski, M. Bzowski, Neutral interstellar hydrogen in the inner heliosphere under the influence of wavelength-dependent solar radiation pressure. Astron. Astrophys. **493**, 207–216 (2008b). doi:10.1051/0004-6361:20077058

G.E. Thomas, The interstellar wind and its influence on the interplanetary environment. Ann. Rev. Earth Planet. Sci. **6**, 173–204 (1978)

H. Tian, W. Curdt, E. Marsch, U. Schühle, Hydrogen Lyman-α and Lyman-β spectral radiance profiles in the quiet sun. Astron. Astrophys. **504**, 239–248 (2009a). doi:10.1051/0004-6361/200811445

H. Tian, W. Curdt, L. Teriaca, E. Landi, E. Marsch, Solar transition region above sunspots. Astron. Astrophys. **505**, 307–318 (2009b). doi:10.1051/0004-6361/200912114

H. Tian, L. Teriaca, W. Curdt, J.-C. Vial, Hydrogen Ly α and Ly β radiances and profiles in polar coronal holes. Astrophys. J. Lett. **703**, L152–L156 (2009c). doi:10.1088/0004-637X/703/2/L152

W.K. Tobiska, T. Woods, F. Eparvier, R. Viereck, L.E. Floyd, D. Bouwer, G. Rottman, O.R. White, The SOLAR2000 empirical solar irradiance model and forecast tool. J. Atmos. Sol. Terr. Phys. **62**, 1233–1250 (2000)

M. Tokumaru, M. Kojima, K. Fujiki, K. Hayashi, Non-dipolar solar wind structure observed in the cycle 23/24 minimum. Geophys. Res. Lett. **360**, L09101 (2009). doi:10.1029/2009GL037461

M. Tokumaru, M. Kojima, K. Fujiki, Solar cycle evolution of the solar wind speed distribution from 1985 to 2008. J. Geophys. Res. **115**, A04102 (2010). doi:10.1029/2009JA014628

A.V. Usmanov, W.H. Matthaeus, B.A. Breech, M.L. Goldstein, Solar wind modeling with turbulence transport and heating. Astrophys. J. **727**, 84 (2011). doi:10.1088/0004-637X/727/2/84

V. Vasyliunas, G. Siscoe, On the flux and the energy spectrum of interstellar ions in the solar wind. J. Geophys. Res. **81**, 1247–1252 (1976)

D.A. Verner, G.J. Ferland, T.K. Korista, D.G. Yakovlev, Atomic data for astrophysics. ii. new fits for photoionization cross-sections of atoms and ions. Astrophys. J. **465**, 487–498 (1996)

I.S. Veselovsky, A.V. Dmitriev, A.V. Suvorova, Algebra and statistics of the solar wind. Cosmic Res. **48**, 113–128 (2010). doi:10.1134/S0010952510020012

A. Vidal-Madjar, Evolution of the solar Lyman alpha flux during four consecutive years. Solar Phys. **40**, 69–86 (1975)

A. Vidal-Madjar, B. Phissamay, The solar L α flux near solar minimum. Solar Phys. **66**, 259–271 (1980)

R.A. Viereck, L.C. Puga, The NOAA Mg II core-to-wing solar index: construction of a 20-year time series of chromospheric variability from multiple satellites. J. Geophys. Res. **104**, 9995–10006 (1999). doi:10.1029/1998JA900163

M.E. Wachowicz, Global model of distribution of ionization states of heavy ions from solar plasma in the heliosphere (in Polish). Dissertation, Space Research Centre PAS, 2006

H.P. Warren, NRLEUV **2**, A new model of solar euv irradiance variability. Adv. Space Res. **37**, 359–365 (2006). doi:10.1016/j.asr.2005.10.028

H.P. Warren, J.T. Mariska, J.L. Lean, A new reference spectrum for the euv irradiance of the quiet sun 1. emission measure formulation. J. Geophys. Res. **103**, 12077–12090 (1998a). doi:10.1029/98JA00810

H.P. Warren, J.T. Mariska, J.L. Lean, A new reference spectrum for the euv irradiance of the quiet sun 2. comparisons with observations and previous models. J. Geophys. Res. **103**, 12091–12102 (1998b). doi:10.1029/98JA00811

H.P. Warren, J.T. Mariska, K. Wilhelm, High-resolution observations of the solar hydrogen Lyman lines in the quiet sun with the SUMER instrument on SOHO. Astrophys. J. Suppl **119**, 105–120 (1998c). doi:10.1086/313151

K.-P. Wenzel, R.G. Marsden, D.E. Page, E.J. Smith, Ulysses: the first high-latitude heliospheric mission. Adv. Space Res. **9**, 25–29 (1989). doi:10.1016/0273-1177(89) 90089-6

T.N. Woods, G.J. Rottman, O.R. White, J. Fontenla, E.H. Avrett, The solar Ly-alpha line profile. Astrophys. J. **442**, 898–906 (1995). doi:10.1086/175492

T.N. Woods, D.K. Prinz, G.J. Rottman, J. London, P.C. Crane, R.P. Cebula, E. Hilsenrath, G.E. Brueckner, M.D. Andrews, O.R. White, M.E. VanHoosier, L.E. Floyd, L.C. Herring, B.G. Knapp, C.K. Pankratz, P.A. Reiser, Validation of the UARS solar ultraviolet irradiances: comparison with the ATLAS 1 and 2 measurements. J. Geophys. Res. **101**, 9541–9570 (1996). doi:10.1029/96JD00225

T.N. Woods, W.K. Tobiska, G.J. Rottman, J.R. Worden, Improved solar Lyman irradiance modeling from 1979 through 1999 based on UARS observations. J. Geophys. Res. **105**, 27195–27215 (2000)

T.N. Woods, F.G. Eparvier, S.M. Bailey, P.C. Chamberlin, J. Lean, G.J. Rottman, S.C. Solomon, W.K. Tobiska, D.L. Woodraska, Solar euv experiment (SEE): mission overview and first results. J. Geophys. Res. **110**, A01312 (2005). doi:10.1029/2004JA010765

F.M. Wu, D.L. Judge, Temperature and velocity of the interplanetary gases along solar radii. Astrophys. J. **231**, 594–605 (1979)